Influence of collective effects on seeded FEL and mitigation strategies at FLASH

Dissertation
zur Erlangung des Doktorgrades
an der Fakultät für Mathematik, Informatik und Naturwissenschaften
Fachbereich Physik
der Universität Hamburg

vorgelegt
von
Dmitrii Samoilenko
aus
Samara, Russland

Hamburg
2024

Gutachter der Dissertation:	Prof. Dr. Wolfgang Hillert Dr. Lucas Schaper
Zusammensetzung der Prüfungskommission:	Prof. Dr. Wolfgang Hillert Dr. Lucas Schaper Prof. Dr. Michael Potthoff Dr. Pardis Niknejadi Prof. Dr. Gudrid Moortgat-Pick
Vorsitzende/r der Prüfungskommission:	Prof. Dr. Michael Potthoff
Datum der Disputation:	14.10.2024
Vorsitzender Fach-Promotionsausschusses PHYSIK:	Prof. Dr. Markus Drescher
Leiter des Fachbereichs PHYSIK:	Prof. Dr. Wolfgang J. Parak
Dekan der Fakultät MIN:	Prof. Dr.-Ing. Norbert Ritter

Declaration on oath

I hereby declare and affirm that this doctoral dissertation is my own work and that I have not used any aids and sources other than those indicated.

If electronic resources based on generative artificial intelligence (gAI) were used in the course of writing this dissertation, I confirm that my own work was the main and value-adding contribution and that complete documentation of all resources used is available in accordance with good scientific practice. I am responsible for any erroneous or distorted content, incorrect references, violations of data protection and copyright law or plagiarism that may have been generated by the gAI.

Hamburg, den 23.07.2024

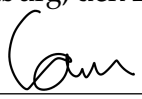

Unterschrift

Contents

Abstract

The Free Electron Laser (FEL) user facility FLASH at DESY is currently being upgraded within the framework of the FLASH2020+ project with the goal of converting one of the beamlines into an externally seeded beamline. In particular, the Echo-Enabled Harmonic Generation (EEHG) method will be used to generate fully coherent FEL pulses in XUV and soft X-ray wavelength regions down to 4 nm. As one of the most challenging of the planned operation modes, 4 nm EEHG can be especially sensitive to the parasitic beam dynamics, known as collective effects. In this work, we employ analytical models to investigate the influence of Incoherent Synchrotron Radiation and Intra-Beam Scattering on the efficiency of the EEHG set-up. We perform numerical simulations to study the effect of Coherent Synchrotron Radiation (CSR) in the seeding section of the beamline on the spectral properties of EEHG bunching. We compare different models of CSR and highlight the importance of such aspects of the models as chamber shielding and transient effects in the parameter space of 4 nm EEHG set-up at FLASH. Furthermore, for CSR, which poses noticeable challenges, we explore a mitigation strategy using short seed laser pulses to optimize the spectral bandwidth. Finally, we demonstrate a promising solution to the Micro-Bunching Instability (MBI) using the recently installed Laser Heater. This thesis is a self-contained detailed investigation of the electron beam dynamics of EEHG in the seeding section in the presence of collective effects and an integral part of ongoing start-to-end simulation efforts for realistic characterization of the performance of the future seeded FEL beamline at FLASH2020+.

Zusammenfassung

Der für den Nutzerbetrieb verwendete Freie-Elektronen-Laser (FEL) FLASH am DESY wird aktuell im Rahmen des Projekts FLASH2020+ erneuert, um in einer der beiden Strahlführungen externes Seeding zu realisieren. Insbesondere wird das Prinzip Echo-Enabled Harmonic Generation (EEHG) verwendet werden, um vollständig kohärente FEL-Pulse mit Wellenlängen im XUV- und weichen Röntgenbereich hinunter bis zu 4 nm zu erzeugen. Als einer der anspruchsvollsten geplanten Betriebsmodi kann EEHG bei einer Wellenlänge von 4 nm besonders empfindlich auf parasitäre Strahldynamik, bekannt als kollektive Effekte, reagieren. In dieser Arbeit verwenden wir analytische Modelle, um den Einfluss von Inkohärenter Synchrotronstrahlung (ISR) und Intra-Beam-Streuung (IBS) auf die Effizienz des EEHG-Prozesses zu untersuchen. Wir führen numerische Simulationen durch, um den Effekt von Kohärenter Synchrotronstrahlung (CSR) in der Seeding-Sektion der Strahlführung auf die spektralen Eigenschaften des EEHG-Bunchings zu untersuchen. Wir vergleichen verschiedene CSR-Modelle und heben die Bedeutung von Aspekten wie Strahlrohrabschirmung und transiente Effekte im Parameterraum des EEHG-Betriebs bei 4 nm am FLASH hervor. Darüber hinaus untersuchen wir für CSR, das bemerkenswerte Herausforderungen darstellt, eine Minderungsstrategie unter Verwendung kurzer Seed-Laserpulse zur Optimierung der spektralen Bandbreite. Schließlich demonstrieren wir eine vielversprechende Lösung für die Mikro-Bunching-Instabilität (MBI) mit dem kürzlich installierten Laser Heater. Diese Arbeit ist eine in sich geschlossene detaillierte Untersuchung der Elektronenstrahldynamik von EEHG in der Seeding-Sektion unter Berücksichtigung kollektiver Effekte. Weiterhin ist diese Arbeit ein integraler Bestandteil der laufenden Anstrengungen zur Realisierung von Simulationen des vollständigen Strahlverlaufs zur realistischen Charakterisierung der Leistungsfähigkeit des Seeding-Betriebs in der zukünftigen Strahlführung bei FLASH2020+.

Dedicated to Mila

Chapter 1

Introduction

1.1 Why EEHG FEL?

Accelerator-based light sources have been an invaluable investigation tool for many research fields, such as atomic and molecular physics, chemistry and biology. The basic principle of their operation is to accelerate a group of charged particles and to manipulate them to make them lose the energy in the form of light. One of the most basic ways to make use of this principle is to bend the trajectory of the accelerated electrons by a magnetic field. This type of radiation was first observed in a synchrotron [1] and is therefore called *synchrotron radiation*. At the time, this radiation was considered as undesired energy losses. Later, when its true potential was understood, synchrotrons developed into dedicated light sources equipped with insertion devices to improve the quality of the emitted radiation. The quality of the radiation can be characterized in many different ways. One of the most comprehensive quantities to characterize a light source is spectral brightness

$$\mathcal{B} = \frac{N_{\mathrm{ph}}}{dt}\frac{1}{d\omega/\omega}\frac{1}{4\pi^2\Sigma_x\Sigma_{x'}\Sigma_y\Sigma_{y'}}, \tag{1.1}$$

where N_{ph} is the number of photons and $d\omega/\omega$ is the relative bandwidth. The last term characterizes the transverse size and divergence of the electron bunch (superscript "e") and the radiation pulse (superscript "ph") with

$$\Sigma_{x,y} = \sqrt{\left(\sigma^{\mathrm{ph}}_{x,y}\right)^2 + \left(\sigma^{\mathrm{e}}_{x,y}\right)^2} \tag{1.2}$$

and

$$\Sigma_{x',y'} = \sqrt{\left(\sigma^{\mathrm{ph}}_{x',y'}\right)^2 + \left(\sigma^{\mathrm{e}}_{x',y'}\right)^2}. \tag{1.3}$$

Therefore, spectral brightness simultaneously quantifies the number of photons produced per second, as well as their spectral purity and how well the radiation pulse can be focused on a sample. A substantial improvement in spectral brightness of accelerator-based light sources was made possible with the development of *free electron lasers* (FELs). The idea was suggested in [2] and the first implementation was reported in [3, 4]. The operational principle is based on an optical cavity, where the light produced by the free electrons in a wiggler is trapped, and the amplification of the emitted radiation is achieved in multiple passes.

Another possible approach would be to use single-pass FEL as an amplifier for radiation from an external source, like a conventional laser. In this case, achieving substantial gain in power in a single pass, known as the high-gain regime, requires using high charge density electron bunches and long undulators. However,

this approach has a limitation in available high-output light sources in XUV wavelength range and below. This limitation was solved by the invention of so-called Self Amplified Spontaneous Emission or SASE [5] FEL. The name can be understood in the following way. The "spontaneous" undulator radiation from the first sections of a long undulator works as the seed for "stimulated" emission in the later sections, which eliminates the necessity of both the initial radiation source and the FEL cavity. A number of user facilities around the world operate SASE FEL [6, 7, 8, 9, 10]. The pulses are typically characterized by high transverse coherence, high peak power and (ultra-) short pulse duration.

However, SASE FELs have their own limitations. The start-up of SASE FEL relies on electron density modulations at the target wavelength at the entrance of the undulator, which are present (although small) in the naturally noisy density distribution, also called shot-noise [5]. Using shot-noise as the source of initial density modulations is advantageous, as it naturally accompanies any practical electron distribution. The consequences of relying on stochastic shot-noise are low longitudinal coherence and poor shot-to-shot stability. In terms of the spectrum of the FEL radiation these consequences show as multiple spikes of varying amplitude, which on average form a relatively broad and poorly reproducible spectrum.

One way to overcome these limitations while still operating at short wavelengths is to create the initial density modulations using a highly coherent external light source at high harmonics of the source. This is the idea behind *external seeding* techniques, specifically the *pre-bunching* approach within these techniques. The two most well-established pre-bunching techniques are High-Gain Harmonic Generation (HGHG) [11] and *Echo-Enabled Harmonic Generation* (EEHG) [12]. The underlying principle behind both of them is to use highly coherent laser radiation to induce an energy modulation in the electron bunch and then to convert it into electron density modulation by carefully-chosen longitudinal dispersion before the bunch enters the undulator. In this case, the electron density modulations are inherently coherent along the electron bunch (or its lasing part). While operating at higher harmonics is increasingly difficult, with the EEHG seeding scheme it is in principle possible to have harmonics up to ≈ 100 [13]. This allows to make use of readily available laser systems operating in UV (wavelength $\sim$ 300 nm) to generate fully coherent short FEL pulses with narrow bandwidth in soft X-ray range (wavelength $\sim$ 1 nm). This combination of light properties is highly desired, e.g. for probing of core electron transitions. Apart from high conversion efficiency at high harmonics, the EEHG scheme is also known to be more persistent with respect to non-ideal electron beam properties at the entrance of the seeding (or pre-bunching) section of the beamline [13].

1.2 Challenges of EEHG

The fact that EEHG is more resistant to the electron beam quality does not mean that it is completely insensitive to the beam parameters and can provide stable output regardless. First, it is still sensitive to fluctuations in the electron beam parameters, in particular current and energy spread. Such fluctuations can take place due to *microbunching instability* or MBI [14], mainly driven by an effect called Longitudinal Space Charge (LSC) [15]. MBI can significantly spoil the stability of EEHG signal, as well as its spectral properties due to the frequency mixing [16]. Second, EEHG is very sensitive to deviations from optimal (for the chosen working point) beam parameters, in particular the energy profile, making any dynamic changes within the

seeding section highly undesirable. This includes both uncorrelated energy spread, which can be induced by effects such as *Incoherent Synchrotron Radiation* (ISR) [17] or *Intra-Beam Scattering* (IBS) [18], as well as correlated energy modulations [19], which can be induced by *Coherent Synchrotron Radiation* (CSR) [20]. Such parasitic energy kicks reduce the efficiency of harmonic conversion and the spectral purity of the signal [21, 19]. The effects mentioned above are referred to as *collective effects*. Additionally, the energy profile of the electron beam at the entrance of the seeding section, in particular the *energy chirp*, can affect the beam dynamics in the seeding section and effectively enhance the influence of the collective effects on EEHG performance.

Managing the complexities of an EEHG FEL, particularly reaching low pulse-to-pulse variation in the high repetition rate case of FLASH, presents an ongoing and challenging development. This study focuses on the crucial aspect of electron beam dynamics within the seeding section of the EEHG FEL beamline, aiming to advance the research on the overall system.

1.3 Literature review on the collective effects

The detrimental effect of the MBI can be mitigated by a device called laser heater (LH) [22]. LH systems were successfully commissioned and a positive effect on FEL output was reported at LCLS [23], FERMI [24], PAL-XFEL [25, 26] and European XFEL [27, 28]. Recently, a LH system has also been installed at FLASH [29].

The theory of ISR and IBS is well-established in the literature. Practical expressions for the ISR-induced energy spread in dipoles can be found in [30, 21, 31] and for IBS in [32, 33, 31]. The effect of smearing of EEHG-bunching due to ISR and IBS is well-understood. It has been estimated for machine parameters of LCLS-II [34], SXFEL [35], SwissFEL [36], as well as of more complex cascaded set-ups (e.g. [37, 38]). The conclusions from these studies are fairly consistent: the bunching degradation due to ISR and IBS is tolerable if the machine is optimized correctly. In this work, we will refer to these studies where appropriate and apply their theories to the FLASH parameters.

The effect of CSR on EEHG spectral properties has been considered in a number of publications, e.g. [19, 39, 40, 41, 42, 43]. A number of mitigation strategies, such as short seed duration and seed laser chirp, have been suggested in [40, 43]. However, these works use simplified CSR models, which lack consideration of potentially important aspects in calculation of CSR. In particular, the importance of transient effects [20, 44], shielding by chamber walls [45, 46] and inter-dipole CSR interaction [47] has been indicated in the literature. Preliminary studies show that the shielding by chicane chamber has a substantial effect of EEHG performance in presence of CSR for FLASH parameters [48]. Currently, no analytical model is available to investigate these effects simultaneously. However, the numerical code introduced in [49] is capable of tracking CSR along an arbitrary trajectory (including multiple bends) in a rectangular chamber [50]. This code can be used for detailed investigation of CSR in the strong first EEHG chicane and its effect of EEHG bunching properties. Such precise calculation of CSR is required for proper compensation of the effect by any of the mitigation techniques mentioned above.

1.4 Scope of this work

This work is structured as follows. Chapter 2 covers the necessary theoretical background. The fundamentals of particle motion in electro-magnetic fields are given in

Sec. 2.1. Basic mathematical constructs and concepts used in accelerator physics are explained in Sec. 2.2. The most common beamline elements and their implementation are listed in Sec. 2.3. A basic explanation of FEL principle and a detailed explanation of the EEHG external seeding technique are given in Sec. 2.4. The physics behind the collective effects and the methods of their estimation are provided in Sec. 2.5. The chapter concludes with an introduction of *laser heater* (LH). Next, Chapter 3 covers analytical, numerical, and experimental results obtained in this work. Performance of an idealized 4 nm EEHG set up at FLASH is summarized in Sec. 3.1 and serves as a reference for the rest of the work. The effects of ISR and IBS on EEHG performance are studied in Sec. 3.2. The detailed simulations of the effect of CSR in the first chicane of 4 nm EEHG set-up are given in Sec. 3.3. The implementation of common mitigation strategies for the effects of CSR and MBI at FLASH is discussed in Sec. 3.4. Chapter 4 reflects on the most important conclusions drawn from Chapter 3 and provides an overview on possible extensions of this work. Finally, Chapter 5 summarizes all the covered material and presents the key findings.

Chapter 2

Theoretical background

2.1 Particles in Electromagnetic Fields

The purpose of this section is to summarize the most essential and general physical laws, required to enter the domain of accelerator physics.

First, we need to introduce a coordinate system. For this we use the concept of the reference particle. This particle has the nominal momentum p_0 and follows the fixed design trajectory. It is convenient then to measure the longitudinal coordinate s along the trajectory of the reference particle. The transverse coordinates x, y are measured from the reference particle and oriented so that $x - y - s$ is a right-handed coordinate system, as shown in Fig. 2.1. The reference trajectory is not necessarily

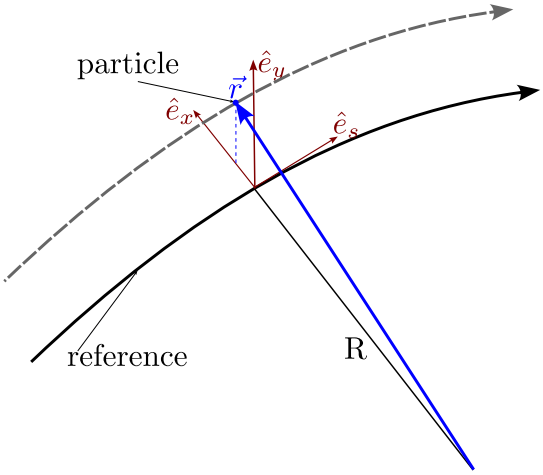

FIGURE 2.1: The coordinate system used throughout the chapter. $\hat{e}_s$ is aligned with the trajectory of the reference particle.

a straight line. In Fig. 2.1 the local shape of the reference trajectory is given by the radius of curvature R. The curvature of the trajectory of an individual particle can be different from R. When the trajectory is curved, the unit vectors change their orientation. If we assume a horizontal layout of the machine, however, the orientation of the unit vector $\hat{e}_y$ remains constant.

2.1.1 Lorentz force

The force acting on a charged particle in EM field - Lorentz force - is given by

$$\vec{F} = q\left(\vec{E} + \vec{v} \times \vec{B}\right), \tag{2.1}$$

where q is the particle charge, $\vec{v}$ is its velocity, $\vec{E}$ and $\vec{B}$ are the electric and the magnetic components of the field, respectively. This formula alone allows for a number of practical considerations for particle accelerator physics. First of all, one can not efficiently accelerate particles by magnetic fields, since the corresponding component of Lorentz force is orthogonal to the direction of motion. Hence, the acceleration is done by longitudinal electric fields. Second, for relativistic particles the second term of Eq. 2.1 is effectively multiplied by the factor $|\vec{v}| \approx c$, where c is the speed of light in vacuum. This means that the same amplitude of, say, F_x component of Lorentz force can be achieved by certain B_y or a much larger E_x, where x, y indicate projections of the field components on corresponding axes. With increasing energy of the particles the use of electric fields for transverse deflection turns from impractical to impossible. Hence, transverse steering of the particles is done by transverse magnetic fields.

Equation 2.1 is naturally essential for beam dynamics in accelerators. In the later sections we will see how certain types of $\vec{E}$ and $\vec{B}$ are typically used in particle accelerators and FELs in particular.

2.1.2 Multipole expansion of magnetic field

In principle, Eq. 2.1 allows to estimate the effect of arbitrary-shaped $\vec{B} = \vec{B}(x, y, s)$. However, design and operation of a machine is much easier if we stick to simple shapes. For this reason, we would like to decompose an arbitrary magnetic field into components of easily understandable practical applications. If the transverse beam size remains small with respect to the radius of curvature of the reference trajectory R, we can perform explicit expansion of the magnetic field with respect to x and y. While such explicit treatment provides insights into magnet design (see, e.g., [51]), we will focus on commonly used practical results. For the horizontal layout of the machine, the magnetic field can be represented as

$$\vec{B}(x, y, s) = \frac{p}{q}\left[\kappa\hat{e}_y - k(y\hat{e}_x + x\hat{e}_y) + l\left(xy\hat{e}_x + \frac{x^2 - y^2}{2}\hat{e}_y\right) + ...\right], \tag{2.2}$$

where p is the momentum of the particle and κ, k, l are multipole strengths of 1st, 2nd and 3rd order terms. Let's quickly discuss the first three terms of Eq. 2.2.

1st order: Dipole field

The first component is a homogeneous field along y-axis. Such a field is created by a dipole magnet and used to deflect particles in the horizontal plane. A more common quantity for characterization of the dipole field is the radius of curvature R:

$$\frac{1}{R} = \kappa\,. \tag{2.3}$$

In practice it is also useful to define bending angle $\vartheta = R/l_b$, where l_b is the effective length of the dipole magnet. R can be also related to the energy of the particle from the centripetal force. Assuming orthogonal $\vec{v}$ and $\vec{B}$,

$$qvB = \frac{m_0 v^2}{R}\,, \tag{2.4}$$

where m_0 is the mass of the particle, $v = |\vec{v}|$ and $B = \left|\vec{B}\right|$. An important conclusion from Eq. 2.4 is that particles with larger momentum are deflected less ($R \sim m_0 v$) by the same magnetic field.

2nd order: Quadrupole field

The second component is the field, which is linear with particle's transverse displacements x and y with respect to the reference trajectory. Such fields are created by quadrupole magnets and are used to focus (defocus) the beam in one (the other) transverse plane. By plugging quadrupole field in Eq. 2.1 we get the restoring force:

$$\vec{F} = qv\left(\frac{p}{q}k\right)(x\hat{e}_x - y\hat{e}_y)\,. \tag{2.5}$$

By choosing the sign of k we can make the quadrupole focus the beam by negative restoring force in x or y, but never both at the same time. In practice it is also useful to draw a parallel between quadrupole magnets and optical lenses. If the length of the quadrupole L_Q is much shorter than its focal length $f^Q_{x,y}$ we can apply thin lens approximation and write

$$\frac{1}{f^Q_{x,y}} = \mp kL_Q\,. \tag{2.6}$$

3rd order: Sextupole field

The third component is non-linear in x and y and also couples the movements in both planes. Such fields are produced by sextupole magnets and can be used to correct for chromaticity. The problem of chromaticity is evident from Eq. 2.5, where the quadrupole focusing depends not only on x and y, but also on the momentum of the particle. Although sextupole magnets exist in the actual setup discussed below, their effect is not considered in this work.

2.1.3 Maxwell equations

Charged particles are not only subjects to EM fields, but can also produce them. To facilitate the discussion of radiation produced by the particles, we introduce Maxwell equations. In differential form they are given by

$$\begin{aligned}
\vec{\nabla}\cdot\vec{B} &= 0\,,\\
\vec{\nabla}\cdot\vec{E} &= \frac{1}{\epsilon_0}\rho\,,\\
\vec{\nabla}\times\vec{B} &= \mu_0\vec{j} + \frac{1}{c^2}\frac{\partial}{\partial t}\vec{E}\,,\\
\vec{\nabla}\times\vec{E} &= -\frac{\partial}{\partial t}\vec{B}\,,
\end{aligned} \tag{2.7}$$

where $\vec{\nabla}$ is the gradient operator, ϵ_0 is vacuum permittivity, ρ is the charge density, μ_0 is vacuum permeability, $\vec{j}$ is the current density and $1/\partial t$ indicates partial derivative with respect to time. Eqs. 2.7 are usually accompanied by the equation of continuity

$$\vec{\nabla}\cdot\vec{j} = -\frac{\partial}{\partial t}\rho\,. \tag{2.8}$$

We can introduce somewhat arbitrary (at first) potentials, which satisfy

$$\begin{aligned}\vec{B} &= \vec{\nabla} \times \vec{A}\,,\\ \vec{E} &= -\frac{\partial \vec{A}}{\partial t} - \vec{\nabla}\Phi\,,\end{aligned} \tag{2.9}$$

where $\vec{A}$ is magnetic vector potential and Φ is electric scalar potential. As long as Eq. 2.7 are satisfied, we can introduce additional conditions on $\vec{A}$ and Φ. A popular choice is the so-called Lorentz gauge:

$$\vec{\nabla} \cdot \vec{A} = -\frac{1}{c^2}\frac{\partial \Phi}{\partial t},. \tag{2.10}$$

This allows to derive inhomogeneous wave equations for the potentials:

$$\begin{aligned}\nabla^2 \vec{A} - \frac{1}{c^2}\frac{\partial^2 \vec{A}}{\partial t^2} &= -\mu_0 \vec{j},\\ \nabla^2 \Phi - \frac{1}{c^2}\frac{\partial^2 \Phi}{\partial t^2} &= -\frac{\rho}{\epsilon_0}\,.\end{aligned} \tag{2.11}$$

2.1.4 Lienard-Wiechert potential

If we consider a point charge e moving with velocity $\vec{v}$, Eq. 2.11 can be solved:

$$\vec{A}(\vec{r},t) = \frac{\mu_0}{4\pi}\left[\frac{e\vec{v}}{\left|\vec{r}-\vec{r'}\right|\left(1-\vec{n}\cdot\vec{\beta}_\gamma\right)}\right]\Bigg|_{t'=t-\frac{\left|\vec{r}(t)-\vec{r'}(t')\right|}{c}}, \tag{2.12}$$

$$\Phi(\vec{r},t) = \frac{1}{4\pi\epsilon_0}\left[\frac{e}{\left|\vec{r}-\vec{r'}\right|\left(1-\vec{n}\cdot\vec{\beta}_\gamma\right)}\right]\Bigg|_{t'=t-\frac{\left|\vec{r}(t)-\vec{r'}(t')\right|}{c}}. \tag{2.13}$$

In the above equations $\vec{\beta}_\gamma = \vec{v}/c$, $\vec{n} = \left(\vec{r}-\vec{r'}\right)/\left|\vec{r}-\vec{r'}\right|$. The equations describe the potential felt by a test particle at the point of space $\vec{r}$ at the moment of time t and produced by the point charge at $\vec{r'}$ at the moment of time t'. t' is referred to as retarded time and illustrates that electro-magnetic fields created by the particles travel with finite speed c. Plugging the resulting potentials into Eqs. 2.9 we obtain the field components

$$\vec{E} = \frac{e}{4\pi\epsilon_0}\left\{\frac{\vec{n}-\vec{\beta_\gamma}}{\gamma^2\left(1-\vec{n}\cdot\vec{\beta}_\gamma\right)^3\left|\vec{r}-\vec{r'}\right|^2} + \frac{\vec{n}\times\left[\left(\vec{n}-\vec{\beta_\gamma}\right)\times\dot{\vec{\beta}_\gamma}\right]}{c\left(1-\vec{n}\cdot\vec{\beta}_\gamma\right)^3\left|\vec{r}-\vec{r'}\right|}\right\}\Bigg|_{t'=t-\frac{\left|\vec{r}(t)-\vec{r'}(t')\right|}{c}}, \tag{2.14}$$

$$\vec{B} = -\frac{\mu_0 e}{4\pi}\left\{\frac{\vec{n}\times\vec{\beta}_\gamma c}{\gamma^2(1-\vec{n}\cdot\vec{\beta}_\gamma)^3\left|\vec{r}-\vec{r'}\right|^2} + \frac{\vec{n}\times\left[\dot{\vec{\beta}}_\gamma + \vec{n}\times\left(\vec{\beta}_\gamma\times\dot{\vec{\beta}}_\gamma\right)\right]}{\left(1-\vec{n}\cdot\vec{\beta}_\gamma\right)^3\left|\vec{r}-\vec{r'}\right|]}\right\}\Bigg|_{t'=t-\frac{\left|\vec{r}(t)-\vec{r'}(t')\right|}{c}}, \tag{2.15}$$

where $\gamma = 1/\sqrt{1-\beta_\gamma^2}$ is the Lorentz factor, $\beta_\gamma = \left|\vec{\beta}_\gamma\right|$ and the dot operator $\dot{} = \partial/\partial t$. The first term of Eq. 2.14 represents the Coulomb field and is commonly referred to as velocity field. The second term represents the radiation field, which exists only if

the acceleration of the charged particle is non-zero. To estimate the radiated power, we calculate the Poynting vector:

$$\vec{S}(t) = \frac{1}{\mu_0}\vec{E}\times\vec{B} = \frac{1}{\mu_0 c}\left[\left(1-\vec{n}\cdot\vec{\beta_\gamma}\right)\left|\vec{E}\right|^2\vec{n}\right]\Big|_{t'=t-\frac{\left|\vec{r}(t)-\vec{r'}(t')\right|}{c}}, \tag{2.16}$$

where the Coulomb part of $\vec{E}$ can be neglected. The power radiated per unit angle is then

$$\frac{dP(t')}{d\Omega} = \left[\left|\vec{r}-\vec{r'}\right|^2\left(\vec{S}\cdot\vec{n}\right)\right]\Big|_{t'=t-\frac{\left|\vec{r}(t)-\vec{r'}(t')\right|}{c}}. \tag{2.17}$$

Evaluating the above expression in polar coordinates results in

$$\frac{dP(t')}{d\Omega} = P_0\,\frac{1}{(1-\beta_\gamma\cos\theta)^3}\left[1-\frac{\sin^2\theta\cos^2\phi}{\gamma^2(1-\beta_\gamma\cos\theta)^2}\right]\Big|_{t'=t-\frac{\left|\vec{r}(t)-\vec{r'}(t')\right|}{c}}, \tag{2.18}$$

where $P_0 = e^2\dot{\vec{\beta}}_\gamma^2/(16\pi^2\epsilon_0 c)$. From Eq. 2.18 we can see that the radiation is mainly emitted in the direction of propagation $\theta = 0$. The width of the radiation cone is roughly given by $\Delta\theta = 2/\gamma$.

2.2 Overview of Beam Dynamics in the Accelerator

The purpose of this section is to introduce quantities and mathematical constructs commonly used to describe beam dynamics in an accelerator.

2.2.1 Beam transport matrix

To describe the beam dynamics through the machine we need to track the coordinates x, y, z and the corresponding momenta p_x, p_y, p of the particles. They can be written as a 6-vector

$$\vec{X} = \begin{pmatrix} x \\ p_x \\ y \\ p_y \\ z \\ p \end{pmatrix}.$$

When a particle described by $\vec{X}_i$ traverses a section of the beamline, its new coordinates become

$$\vec{X}_f = \mathbb{M}\cdot\vec{X}_i\,, \tag{2.19}$$

where $\mathbb{M}$ describes the effect of the beamline section in an arbitrary complex way. Once again, for practical purposes we would like to decompose something complex into simpler and comprehensible components. To justify it, we need to assume that the change in coordinates remains relatively small. Usually $p_x, p_y \ll p$ holds quite well in an accelerator. The magnitudes of x, y should be compared to the "good-field" regions of the magnets, where the field felt by the particles is well-described by the expressions in Subsec. 2.1.2. With those approximations we can rewrite Eq. 2.19 as

$$X_i = \sum_j R_{ij}X_j + \sum_j\sum_k T_{ijk}X_jX_k + \ldots\,, \tag{2.20}$$

where R_{ij} are the elements of a 6×6 matrix $\mathbb{R}$ and T_{ijk} describe higher order correlations between the coordinates. Truncating the above expression after $\mathbb{R}$ we reduce the problem of beam dynamics to linear optics. Transporting the beam through N subsequent sections of the beamline is then done by

$$\vec{X}_f = \mathbb{R}_N \mathbb{R}_{N-1} \cdots \mathbb{R}_1 \cdot \vec{X}_i \,. \tag{2.21}$$

$\mathbb{R}$ is commonly referred to as transport matrix and can be derived for the most basic beamline elements, such as drifts, dipoles and quadrupoles. For these elements the transverse components x and y are usually decoupled from one another, which makes $R_{13} = R_{14} = R_{23} = R_{24} = R_{31} = R_{41} = R_{32} = R_{42} = 0$, and from the longitudinal coordinate, which makes $R_{15} = R_{25} = R_{35} = R_{45} = 0$. The assumption of horizontal layout of the machine, which we made in Subsec. 2.1.2, also makes $R_{53} = R_{54} = 0$ and eventually $R_{36} = R_{46} = 0$. We are left with

$$\mathbb{R} = \begin{pmatrix} R_{11} & R_{12} & 0 & 0 & 0 & R_{16} \\ R_{21} & R_{22} & 0 & 0 & 0 & R_{26} \\ 0 & 0 & R_{33} & R_{34} & 0 & 0 \\ 0 & 0 & R_{43} & R_{44} & 0 & 0 \\ R_{51} & R_{52} & 0 & 0 & 0 & R_{56} \\ 0 & 0 & 0 & 0 & 0 & 1 \end{pmatrix} . \tag{2.22}$$

The longitudinal dispersion component R_{56} is of particular importance for the discussion of seeded FELs and bunch compression, as will be shown in later sections. The components related to $x - p_x$ and $y - p_y$ planes are important for transverse beam dynamics.

2.2.2 Transverse beam dynamics

For the discussion of transverse beam dynamics we reduce $\vec{X}$ to the first 4 coordinates

$$\begin{pmatrix} x \\ x' \\ y \\ y' \end{pmatrix} ,$$

where x' and y' are the angular displacements in the corresponding planes, defined as $p_x = \beta_\gamma \gamma m_0 c x'$ and $p_y = \beta_\gamma \gamma m_0 c y'$, where m_0 is the rest mass of the particle. The transport matrix is reduced to 4x4 matrices

$$\mathbb{M} = \begin{pmatrix} M_{11} & M_{12} & 0 & 0 \\ M_{21} & M_{22} & 0 & 0 \\ 0 & 0 & M_{33} & M_{34} \\ 0 & 0 & M_{43} & M_{44} \end{pmatrix} = \begin{pmatrix} \mathbb{M}_x & \begin{pmatrix} 0 & 0 \\ 0 & 0 \end{pmatrix} \\ \begin{pmatrix} 0 & 0 \\ 0 & 0 \end{pmatrix} & \mathbb{M}_y \end{pmatrix} . \tag{2.23}$$

To derive the elements of $\mathbb{M}$ we need to formulate and solve the equations of motion.

Equations of motion

First, we introduce a transverse coordinate vector

$$\vec{r}(s) = r_x \cdot \hat{e}_x + y \cdot \hat{e}_y = (R + x) \cdot \hat{e}_x + y \cdot \hat{e}_y \,, \tag{2.24}$$

as illustrated in Fig. 2.1. Conceptually, the equations of motion are supposed to give $x(t)$ and $y(t)$. However, since we introduced the coordinate system x, y, s, we will rather look for $x(s)$ and $y(s)$. To relate the coordinates to the Lorentz force acting on the particles, we need to deal with the time derivatives, so we need to find the relation between $\frac{d}{dt}$ and $\frac{d}{ds}$. For the reference particle we obviously have $\frac{d}{dt} = v\frac{d}{ds}$. For an individual particle, whose trajectory is displaced with respect to the reference particle, we rather have

$$\frac{d}{dt} = v\left(\frac{R}{r_x}\right)\frac{d}{ds} \tag{2.25}$$

from geometrical considerations. As was mentioned in the beginning of this chapter, the unit vectors $\hat{e}_x$ and $\hat{e}_s$ change their orientation along s, meaning that we need to find their derivatives with respect to s. From Fig. 2.1, a step ds in the direction of $\hat{e}_s$ rotates $\hat{e}_x$ by ds/R in the direction of propagation. The same step rotates the unit vector $\hat{e}_s$ by the same angle in the direction opposite to $\hat{e}_x$. This gives

$$\begin{aligned} \frac{d}{ds}\hat{e}_x &= \frac{1}{R}\hat{e}_s\,, \\ \frac{d}{ds}\hat{e}_s &= -\frac{1}{R}\hat{e}_x\,. \end{aligned} \tag{2.26}$$

The momentum of the individual particles p can also be slightly different from the nominal p_0, which gives

$$\begin{aligned} \Delta p &= p - p_0\,, \\ \frac{1}{p} &\approx \frac{1}{p_0}\left(1 - \frac{\Delta p}{p_0}\right)\,, \end{aligned} \tag{2.27}$$

where the bottom equation is the Taylor expansion truncated after the 1st-order term. Finally, Newton's second law gives

$$\gamma m_0 \frac{d^2\vec{r}}{dt^2} = q\left(\vec{v}\times\vec{B}\right)\,. \tag{2.28}$$

Combining Eqs. 2.25 - 2.28 and the first two terms of Eq. 2.2 we finally get

$$\begin{aligned} &\frac{d^2}{ds^2}x(s) + \left[\frac{1}{R^2(s)} - k(s)\right]x(s) = \frac{1}{R}\frac{\Delta p}{p_0}\,, \\ &\frac{d^2}{ds^2}y(s) + k(s)y(s) = 0\,. \end{aligned} \tag{2.29}$$

Examples

The above equations can be solved with respect to the initial values $\vec{X}_i$ for drift, dipole and quadrupole sections of the beamline. As an illustration, we show explicit solutions for a monochromatic beam $\Delta p = 0$. For a drift of length L we obtain

$$\mathbb{M}_{\text{drift}} = \begin{pmatrix} 1 & L & 0 & 0 \\ 0 & 1 & 0 & 0 \\ 0 & 0 & 1 & L \\ 0 & 0 & 0 & 0 \end{pmatrix}\,. \tag{2.30}$$

For a rectangular dipole, characterized by the radius of curvature R and the bending angle $\vartheta << 1$ we get

$$\mathbb{M}_{\text{dipole}} = \begin{pmatrix} 1 & R\vartheta & 0 & 0 \\ 0 & 1 & 0 & 0 \\ 0 & 0 & \cos\vartheta & R\vartheta \\ 0 & 0 & -\dfrac{\sin^2\vartheta}{R\vartheta} & \cos\vartheta \end{pmatrix} \tag{2.31}$$

For a quadrupole of length L depending of the sign of k we get

$$\mathbb{M}_{k>0} = \begin{pmatrix} \cos(\sqrt{|k|}L) & \dfrac{1}{\sqrt{|k|}}\sin(\sqrt{|k|}L) & 0 & 0 \\ -\sqrt{|k|}\sin(\sqrt{|k|}L) & \cos(\sqrt{|k|}L) & 0 & 0 \\ 0 & 0 & \cosh(\sqrt{|k|}L) & \dfrac{1}{\sqrt{|k|}}\sinh(\sqrt{|k|}L) \\ 0 & 0 & \sqrt{|k|}\sinh(\sqrt{|k|}L) & \cosh(\sqrt{|k|}L) \end{pmatrix} \tag{2.32}$$

or

$$\mathbb{M}_{k<0} = \begin{pmatrix} \cosh(\sqrt{|k|}L) & \dfrac{1}{\sqrt{|k|}}\sinh(\sqrt{|k|}L) & 0 & 0 \\ \sqrt{|k|}\sinh(\sqrt{|k|}L) & \cosh(\sqrt{|k|}L) & 0 & 0 \\ 0 & 0 & \cos(\sqrt{|k|}L) & \dfrac{1}{\sqrt{|k|}}\sin(\sqrt{|k|}L) \\ 0 & 0 & -\sqrt{|k|}\sin(\sqrt{|k|}L) & \cos(\sqrt{|k|}L) \end{pmatrix} \tag{2.33}$$

An important property of transfer matrices in each plane is

$$\det \mathbb{M}_{x,y} = 1\,. \tag{2.34}$$

2.2.3 Beam emittance

Using Eq. 2.29 we can track particles, which have different initial coordinates and different energies. At any point of the beamline s we can take a snapshot of the phase space in one of the transverse planes, e.g., $x - p_x$. We can apply the Liouville theorem and conclude that the phase space area occupied by the particles remains constant along s. Since x' is essentially scaled p_x, the same statement also applies to $x - x'$ plane. The trace space is schematically depicted in Fig. 2.2. Assuming the x and x' distributions of the particles are centered around the reference particle, their mean values are $\langle x \rangle = \langle x' \rangle = 0$. The "widths" of the distributions are given by the variances

$$\sigma_x = \frac{1}{N}\sum_i x_i^2 \qquad\qquad \sigma_{x'} = \frac{1}{N}\sum_i x_i'^2\,, \tag{2.35}$$

where N is the number of particles. Distributions in x and x' are usually correlated. We can introduce two different axes, along which the distributions are not correlated, as shown in Fig. 2.2. The area of the trace space covered by the particles is better characterized by variances along these two axes. Skipping the derivation, the area is given in the original coordinates by

$$\pi\epsilon_x = \sqrt{\langle x^2\rangle\langle x'^2\rangle - \langle xx'\rangle^2}\,, \tag{2.36}$$

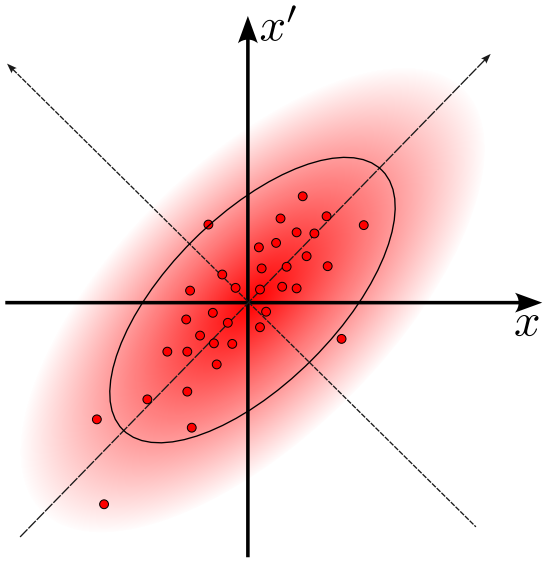

FIGURE 2.2: Schematic illustration of trace space.

where ϵ_x is the beam emittance in $x - x'$ plane. The emittance is an important characteristic of the beam quality. Parametrization of the rotated ellipse in the original coordinates gives

$$\epsilon_x^2 = x^2\sigma_{x'}^2 - 2xx'\langle xx'\rangle + x'^2\sigma_x^2 \,. \tag{2.37}$$

2.2.4 Twiss parameters

A very similar expression can be obtained if we treat Eq. 2.29 as the equation of harmonic oscillator with s-dependent amplitude and frequency of the oscillations around the reference trajectory. Averaging the solutions over the particle distribution, we arrive to

$$\epsilon_x = \gamma_{T_x}(s)x^2 + 2\alpha_x(s)xx' + \beta_x(s)x'^2 \,, \tag{2.38}$$

where $\beta_x(s)$ describes the evolution of the particles' trajectories envelope along the beamline. It is related to the RMS beam size as

$$\sigma_x(s) = \sqrt{\epsilon_x\beta_x(s)} \,. \tag{2.39}$$

α_x describes the correlation between x and x' and is given by

$$\alpha_x(s) = -\frac{1}{2}\frac{d\beta_x(s)}{ds} \,. \tag{2.40}$$

Finally, γ_{T_x} describes the divergence of the beam and is given by

$$\gamma_{T_x}(s) = \frac{1+\alpha_x^2(s)}{\beta_x(s)} \,. \tag{2.41}$$

The treatment of $y - y'$ plane is completely analogous. α, β, γ_T are known as Twiss parameters. For certain given initial conditions they are rather characteristics of the magnetic lattice than the beam. However, they can be easily related to the transverse dynamics of the beam traversing the lattice, as shown above. It is, therefore, convenient to be able to track the Twiss parameters through the lattice using the transport matrices, as it is done for the particles. This is possible by introducing the

beta matrix

$$\mathbb{B} = \begin{pmatrix} \beta & -\alpha \\ -\alpha & \gamma_T \end{pmatrix}, \tag{2.42}$$

where the sub-index x or y is implied. If the section of the beamline is described by the transport matrix $\mathbb{M}$, as introduced above, the initial $\mathbb{B}_i$ transforms at the end of the section into

$$\mathbb{B}_f = \mathbb{M} \cdot \mathbb{B}_0 \cdot \mathbb{M}^T, \tag{2.43}$$

where ^{T} is the transpose operator.

2.2.5 Wake potential and impedance

A proper introduction to the concepts of wake potential and impedance can be found, e.g., in [52]. Here we will summarize the basic definitions, restricting ourselves to the longitudinal dimension only.

Strictly speaking the term "wakefield" is used for the following scenario. A relativistic charged particle is travelling through a conductive pipe. The electromagnetic field created by the particle is almost purely transversal and the particles behind or in front of the source particle are not affected by the field. However, when the shape of the beam pipe changes, there could be some residual fields trailing after the particle. These fields can affect the particles behind the source particle. Suppose, we managed to solve the Maxwell equations for the source particle and calculated the electric field $\vec{E}(z,t)$ and the magnetic field created by the source particle with the charge q_1. The longitudinal *wake function* is then defined as

$$w_\parallel(z) = \frac{1}{q_1} \int_{-\infty}^{\infty} dz'\, E_z(z', (z-z')/c), \tag{2.44}$$

where z is the distance from the source particle and E_z is the longitudinal component of the electric field. We note that the wake function is normalized to the source particle's charge. This makes the wake function a characteristic of the geometry of the problem, rather than of a specific particle bunch traversing this geometry. If the bunch is characterized by the line charge distribution $\lambda(z)$, we can calculate the *wake potential*

$$W_\parallel(s,z) = \int_{-\infty}^{\infty} dz'\, w_\parallel(s, z-z')\lambda(s,z'). \tag{2.45}$$

Here we used two independent coordinates: longitudinal bunch coordinate z and the beamline coordinate s for more convenient interpretation. The wake potential at given s shows the energy kick experienced by a particle at z as the net effect of all other particles at z'. This quantity is already specific to the certain bunch shape, but can be easily scaled with the total charge of the bunch.

Finally, we introduce the longitudinal *impedance*

$$Z(s,k) = -\frac{1}{c} \int_{-\infty}^{\infty} dz\, w_\parallel(s,z) e^{-ikz}, \tag{2.46}$$

where the subscript $_\parallel$ is omitted for $Z(s,k)$ for brevity. In other words, the impedance is the Fourier counterpart of the wake function. Therefore, it is also specific to the geometry of the problem. Since the impedance is formulated in the reciprocal space it

also gives the information about which frequencies are favoured by the environment of the bunch. This is especially convenient when the beam pipe has local cavities. These cavities are characterized by eigenmodes, which show as sharp peaks of the impedance.

The type of the wakefields discussed above are natural for the introduction of wake potential and impedance, but they are not discussed in this work. However, the introduced concepts will be applied to a different kind of self-interaction in an electron bunch.

2.3 Key Accelerator Components

The purpose of this section is to introduce typical components of an accelerator and specific layouts of the beamlines considered in this work. The description of the components is focused on their purpose in the beamline and basic underlying physical phenomena, rather than on their design and technical specifications. FLASH 2020+ layout is explained to the extent needed for the purposes on this work.

2.3.1 Gaussian bunches, pulses and beams

Gaussian shape is one of the most typical approximations for the longitudinal shape of electron bunches and laser pulses, which is also widely used in this work. We refer to the electron bunch as Gaussian if the current (or charge) distribution within the bunch is given by

$$I(z) = I_0 \exp\left(-\frac{z^2}{2\sigma_z^2}\right), \tag{2.47}$$

where I_0 is the peak current and σ_z is called the bunch length. Since we often compare the longitudinal dimension of the bunch to the radiation wavelength, the former is typically given in units of length. We refer to the laser pulse as Gaussian, if the distribution of power (or intensity) within the pulse is given by

$$P(t) = P_0 \exp\left(-\frac{t^2}{2\sigma_t^2}\right), \tag{2.48}$$

where P_0 is the peak power and σ_t is called the pulse duration. Since the pulse duration is typically given in units of time, the longitudinal coordinate is given by time t, rather than by z. It is important to note that the laser pulse can be also given in terms of the electric field $E(t)$ with the equivalent pulse duration $\sqrt{2}\sigma_t$. In this work we discuss only *transform limited* pulses, for which the spectral width is $\sigma_\omega = 1/2\sigma_t$.

Gaussian beams can be used to describe both the FEL output and the seed lasers [53]. In this work the fundamental Gaussian mode is used to model the seed laser. The laser field is then given by

$$E(r,z,t) = \frac{\mathcal{E}_0}{\sqrt{1+(z/z_R)^2}} \exp\left(-\frac{r^2}{w^2(z)}\right) \sin\left[k_L(z-ct)+\psi\right] \exp\left(-\frac{(z-ct)^2}{4c^2\sigma_t^2}\right), \tag{2.49}$$

where $r = \sqrt{x^2+y^2}$ is the radial coordinate, $\mathcal{E}_0$ is the electric filed amplitude, k_L is the laser wave number. The evolution of the transverse size is given by

$$w(z) = w_0\sqrt{1+(z/z_R)^2}, \tag{2.50}$$

where w_0 is called the *waist* and the *Rayleigh length* is

$$z_R = \frac{\pi w_0^2}{\lambda_L}, \tag{2.51}$$

where λ_L is the wavelength of the laser field. The phase term is

$$\psi = -\arctan\left(z/z_R\right) + k_L \frac{r^2}{2R_w(z)} + \psi_0, \tag{2.52}$$

where the first term is referred to as *Gouy phase*, ψ_0 is an arbitrary phase and the radius of curvature of the wavefronts is

$$R_w(z) = z\left[1 + \left(z_R/z\right)^2\right]. \tag{2.53}$$

In the following we will be mostly interested in the on-axis radiation, meaning that the terms of Eq. 2.49 with r will be neglected. The arbitrary phase ψ_0 is also typically neglected, since it only becomes important for extremely short ($\sigma_t \sim \lambda_L/c$) pulses. The Gouy phase introduces an interesting effect near the waist, where the phase velocity of the beam becomes greater than c.

2.3.2 Accelerating RF cavities

Radio Frequency (RF) cavities are the most essential part of linacs as they provide the actual acceleration of the particles. This is done by applying voltage V_{RF} between N_{RF} pairs of electrodes. As the particles with charge q travel through the drifts between the electrodes, they gain energy $\Delta E = V_{\mathrm{RF}} N_{\mathrm{RF}} q$. The voltage is supplied by an RF source, hence the "RF" in the name. In order to suppress radiation from the drift tubes between the electrodes, the accelerating structure is enclosed in a conducting cylinder, hence the "cavity" in the name. If the enclosing cylinder is made of superconducting material, one speaks of superconducting cavities. The advantage of superconducting cavities is lower energy dissipation, which typically allows higher accelerating gradients and higher repetition rate of accelerated electron pulses. Technical parameters, such as operating frequency, cavity geometry etc. are dictated by availability of high power RF sources, minimization of energy dissipation, costs, size and other practical considerations [54].

One important consequence of the electron beam being accelerated by an RF field is non-uniform energy profile of the electron beam. If $V_{\mathrm{RF}}(z) = V_0 \cos\left(\frac{2\pi f}{c} z + \varphi_{\mathrm{RF}}\right)$, where f is the RF frequency, the energy gained by the electrons is also a function of their longitudinal coordinate with respect to the center of the bunch z. The relative phase between the center of the bunch and the crest of the RF pulse φ_{RF} is commonly called RF phase. Examples of energy profiles of an electron beam accelerated on-crest ($\varphi_{\mathrm{RF}} = 0°$) and off-crest ($\varphi_{\mathrm{RF}} = 10°$) are shown in Fig. 2.3, where $f = 1.3$ GHz and $V_0 \cdot N_{\mathrm{RF}} = 25$ MV. Resulting energy profiles have a cosine shape. For practical purposes they are usually characterized by the energy gain of the center of the bunch ΔE, energy chirp $\frac{dE}{dz}$, curvature $\frac{d^2E}{dz^2}$ and the third order derivative. The practical importance of the energy gain is obvious. The energy chirp has practical importance for the bunch compression, as will be explained below. For the bunch compression purposes, the curvature is usually considered as an undesired complication. If necessary, the curvature can be controlled by so-called linearizers. An example of a linearizer is a third harmonic cavity (with the operating frequency $3f$)

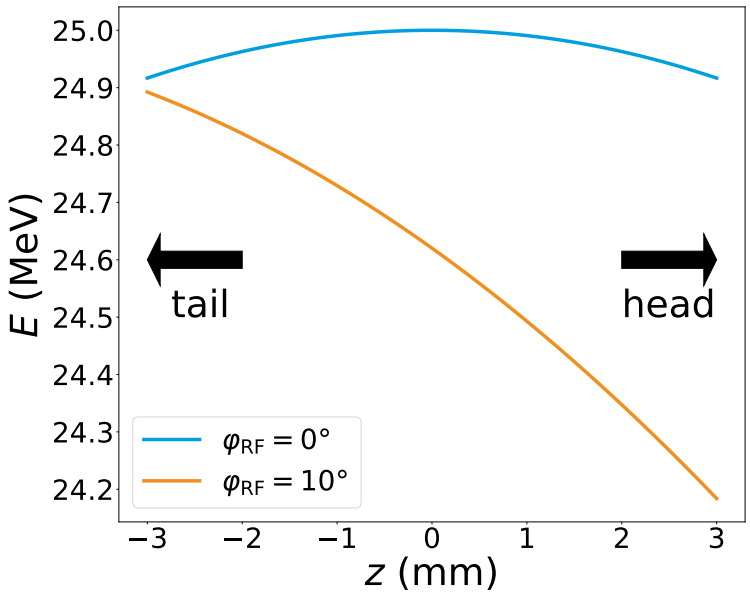

FIGURE 2.3: Energy gain as a function of the bunch coordinate for the electron beam accelerated with different RF phases and the same RF amplitude V_0. Note the directions of the tail and the head of the bunch. Off-crest accelerated bunch gains negative energy chirp.

installed after the usual accelerating module. This provides additional degrees of freedom to control the curvature, while keeping the energy gain and the chirp in a reasonable range.

The electrons, which are more downstream (upstream) with respect to the center of the bunch form the *head* (the *tail*) of the bunch. In Fig. 2.3 the head of the off-crest accelerated bunch has lower energy, than the tail. In our convention this corresponds to negative electron beam energy chirp. The sign of the chirp is very important for the bunch compression.

2.3.3 Chicanes

Chicanes are dispersive elements in the beamline. The basic idea is to deflect the trajectory of the electrons from the straight line in a section of the beamline. As shown in Subsec. 2.1.2, dipole magnets are a natural choice for electron deflectors. Since the deflection angle in a dipole depends on the particle energy, travelling through an arrangement of dipoles introduces longitudinal dispersion. Figure 2.4 shows the layout of a C-type chicane. The lower energy particles experience larger kick, according to Eq. 2.4. Therefore, they are delayed with respect to the reference particle. For the higher energy particles the situation is reversed. The strength of a symmetrical chicane can be characterized by the bending angle ϑ or the radius of curvature R in the first dipole, as shown in Fig. 2.4. These quantities are convenient to use when we discuss the processes inside the chicane itself. When we are only interested in the dispersive effect of the whole chicane, we usually characterize it either by the delay (the difference between the path of the reference particle and the straight line) or the element of the transport matrix R_{56}. For small ϑ we can approximate delay $= R_{56}/2$. The sign of R_{56} can be subject to different conventions. Using the logic that the higher energy particles are effectively pushed forward, for this type of chicane $R_{56} > 0$.

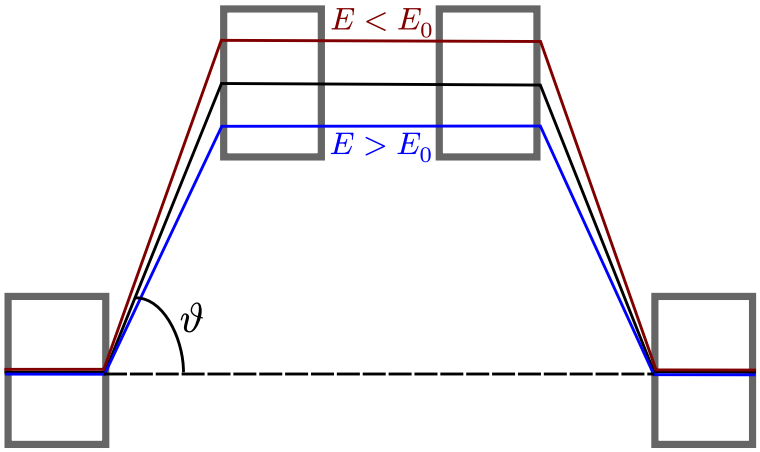

FIGURE 2.4: Layout of a C-type chicane. Lower energy electrons (red) travel longer path than the higher energy electrons (blue). The reference path (black) is used to characterize the chicane.

Chicanes are used for different purposes in the beamline. Sometimes their only purpose is to make electrons go around another component of the beamline, e.g., an in-coupling mirror. In seeded FELs they are used to generate density modulations from energy modulations, as will be shown below. In the linac they are commonly used for the compression of the electron bunch.

Bunch compressors

Let us consider two particles within the bunch, which are characterized by their longitudinal coordinates $z_i^{(1),(2)}$ and relative energy deviation $p_{1,2} = (E_0 + \Delta E_{1,2})/E_0$. After passing through the chicane with certain R_{56}, their coordinates are given by

$$\begin{aligned} z_f^{(1)} &= z_i^{(1)} + R_{56}\frac{\Delta E_1}{E_0}, \\ z_f^{(2)} &= z_i^{(2)} + R_{56}\frac{\Delta E_2}{E_0}. \end{aligned} \tag{2.54}$$

Generally speaking, ΔE can have a correlated part $E(z)$ from the RF linac (see Subsec. 2.3.2) and an uncorrelated part ΔE_{unc}. If we consider only the linear component of $E(z)$ (i.e., electron beam chirp), we obtain

$$\begin{aligned} z_f^{(1)} &= z_i^{(1)}\left(1 + R_{56}\frac{1}{E_0}\frac{dE(z)}{dz}\right) + R_{56}\frac{\Delta E_{\text{unc}}^{(1)}}{E_0}, \\ z_f^{(2)} &= z_i^{(2)}\left(1 + R_{56}\frac{1}{E_0}\frac{dE(z)}{dz}\right) + R_{56}\frac{\Delta E_{\text{unc}}^{(2)}}{E_0}. \end{aligned} \tag{2.55}$$

Subtracting the top equation from the bottom one we get

$$z_f^{(2)} - z_f^{(1)} = \left(z_i^{(2)} - z_i^{(1)}\right)(1 + R_{56}h_1) + R_{56}\frac{\Delta E_{\text{unc}}^{(2)} - \Delta E_{\text{unc}}^{(1)}}{E_0}, \tag{2.56}$$

where $h_1 = \frac{1}{E_0}\frac{dE(z)}{dz}$ is the normalized linear chirp. The left-hand part of the equation is the distance between the particles after they pass through the chicane. The

first term of the right-hand part is the distance between the same particles before the chicane multiplied by $C^{-1} = (1 + R_{56}h_1)$, where C is the linear compression factor. Repeating the procedure for the whole bunch we can rewrite Eq. 2.56 in RMS terms:

$$\sigma_z^{(f)} = \sigma_z^{(i)} (1 + R_{56}h_1) + R_{56}\frac{\sigma_E}{E_0}, \tag{2.57}$$

where $\sigma_z^{(i,f)}$ is the RMS bunch length before and after the chicane and σ_E is the RMS uncorrelated energy spread. If σ_E can be neglected, the definition of C becomes obvious. If $R_{56}h_1 < 0$ the bunch is compressed by the factor of C by the chicane. For this purpose one can combine positive R_{56} of a C-type chicane with negative electron beam chirp, such as shown in Fig. 2.3. At the extreme compression with $R_{56}h_1 = -1$ the minimum achievable length of the compressed bunch is limited by $R_{56}\sigma_E / E_0$.

2.3.4 Undulators

Undulators are periodic arrangements of dipole magnets, as illustrated in Fig. 2.5. Here we consider only planar undulators and not the helical ones. The magnetic

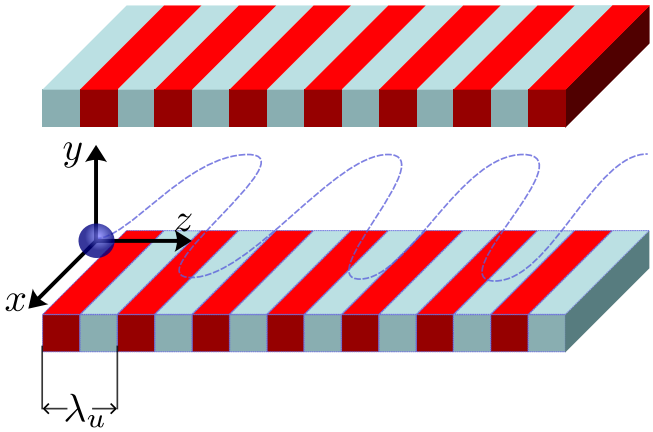

FIGURE 2.5: Schematic illustration of a planar undulator with the period λ_u. The particle moves along a sinusoidal trajectory in the plane of the undulator in the middle between the plates.

field felt by the particle inside the undulator is given by

$$\begin{aligned} B_x &= 0\,, \\ B_y &= B_0 \cosh(k_u y) \cos(k_u z)\,, \\ B_z &= -B_0 \sinh(k_u y) \sin(k_u z)\,, \end{aligned} \tag{2.58}$$

where $k_u = 2\pi/\lambda_u$, λ_u is the undulator period indicated in Fig. 2.5 and B_0 is the peak value of the magnetic filed along the undulator axis. B_z component deflects the particle in the transverse plane proportionally to its p_x and p_y due to the Lorentz force. Using the assumption $p \gg p_x, p_y$ we can neglect this deflection and limit the discussion to the effect of B_y. Using the assumption that the particle displacement in y is much smaller than λ_u we also put $\cosh(k_u y) = 1$. This leaves us with

$$\vec{B} = B_0 \cos(k_u z)\, \hat{e}_y\,. \tag{2.59}$$

The equations of motion then give

$$v_x(t) = \frac{d}{dt}x(t) = -\frac{eB_0}{\gamma m k_u}\sin\left(k_u z\right) . \tag{2.60}$$

Due to the transverse motion the longitudinal velocity component v_z is reduced to

$$v_z(t) = \frac{d}{dt}z(t) = \sqrt{v^2 - v_x^2} = \beta_\gamma c\sqrt{1 - \left(\frac{eB_0}{mck_u}\right)^2 \frac{1}{\beta_\gamma^2\gamma^2}\sin^2\left(k_u z(t)\right)} , \tag{2.61}$$

which is a function of t. Integration of the above expression gives the average longitudinal velocity

$$\bar{\beta}_\gamma = \beta_\gamma\left(1 - \frac{K_u^2}{4\beta_\gamma^2\gamma^2}\right) , \tag{2.62}$$

with

$$K_u = \frac{eB_0}{mck_u} . \tag{2.63}$$

The undulator parameter K_u is commonly used to characterize the amplitude of the electron deflection inside the undulator. In particular, $K = 1$ means that the electrons are deflected by $\approx 1/\gamma$, which is the opening angle of the synchrotron radiation discussed in Sec. 2.1.4. A useful expression to estimate the undulator parameters is

$$K_u = 0.934 \cdot B_0[\mathrm{T}] \cdot \lambda_u[\mathrm{cm}] . \tag{2.64}$$

An important conclusion from Eq. 2.62 is that a relativistic electron ($\beta_\gamma = 1$) is delayed due to the oscillations with respect to the straight on-axis trajectory by the so-called *slippage length*

$$\lambda_{\mathrm{slip}} = \frac{\lambda_u}{2\gamma^2}\left(1 + \frac{K_u^2}{2}\right) \tag{2.65}$$

for each λ_u traveled. Integrating Eq. 2.60 and Eq. 2.61 and using the newly defined K_u we get the solutions of the equations of motion

$$\begin{aligned} x(t) &= \frac{K_u}{\gamma k_u}\sin\left(\bar{\beta}_\gamma c k_u t\right) , \\ z(t) &= \bar{\beta}_\gamma c t - \frac{K_u^2}{8\gamma^2 k_u}\sin\left(2\bar{\beta}_\gamma c k_u t\right) . \end{aligned} \tag{2.66}$$

The above equations tell us that the electron oscillates in x with the frequency $\omega_u = \bar{\beta}_\gamma c k_u$ and in z with $2\omega_u$. If we refer to Eq. 2.18, we could calculate the power radiated due to these oscillations. More importantly at the moment, we can calculate the frequency of the emitted radiation. To do this, we need to keep in mind that the radiated power is given by Eq. 2.18 in the laboratory reference frame. For the reference frame, which is moving along z with the averaged $\bar{\beta}_\gamma c$, the Lorentz factor is

$$\bar{\gamma} = \frac{1}{\sqrt{1 - \bar{\beta}_\gamma^2}} = \frac{\gamma}{\sqrt{1 + K_u^2/2}} . \tag{2.67}$$

Due to the time contraction, in this reference frame the frequency of the oscillations is multiplied by $\bar{\gamma}$. If we do Lorentz transformation for the photon of this frequency

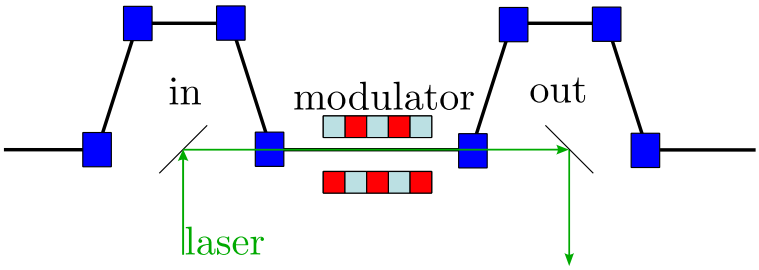

FIGURE 2.6: Schematic representation of a typical modulator layout. The laser is in- and out-coupled using mirrors in the middle of the chicanes. Inside the undulator the laser is co-propagating with the electron beam.

emitted at the polar angle θ, we get

$$\lambda_l = \lambda_u \left(1 - \bar{\beta} \cos\theta\right) , \tag{2.68}$$

where λ_l is the wavelength of the emitted light in the laboratory reference frame. Using Eq. 2.62 and $\cos\theta \approx 1 - \theta^2/2$ for small θ:

$$\lambda_l = \frac{\lambda_u}{2\gamma^2} \left(1 + \frac{K_u^2}{2} + \gamma^2\theta^2\right) . \tag{2.69}$$

An important conclusions from Eq. 2.69 is that for on-axis radiation the slippage length given by Eq. 2.65 is exactly the radiation wavelength.
In order to estimate the bandwidth of the on-axis undulator radiation, we assume that the undulator consists of N_u periods. The electric field of the radiation is

$$E(t) = \begin{cases} E_0 \exp\left(i\omega_l t\right) & \text{inside the undulator}, \\ 0 & \text{outside the undulator} \end{cases} \tag{2.70}$$

with the amplitude E_0 and frequency $\omega_l = 2\pi c/\lambda_l$. Taking the Fourier transform of the field above $E(\omega)$ we get the spectral distribution of the radiated power

$$P(\omega) \sim |E(\omega)|^2 \sim \mathrm{sinc}^2 \left(\pi N_u \frac{\omega_l - \omega}{\omega_l}\right) . \tag{2.71}$$

An important conclusion from the above equation is that bandwidth of the undulator radiation can be estimated as $1/N_u$.

Modulators

One particular implementation of the undulators is energy modulation of the electron beam by the means of an external laser. Such devices are called modulators. An illustration of the typical layout of a modulator is shown in Fig. 2.6. First, the laser beam is in-coupled to the electron beamline. For this purpose one typically uses a chicane (which might also simultaneously serve another purpose) to deflect electrons from the straight path, which allows to insert a mirror into the beamline. Then, the laser co-propagates with the electron beam inside the undulator. We assume the laser field to be a plane wave linearly polarized along x:

$$E_x(z,t) = \mathcal{E}_0 \cos\left(k_l z - \omega_l t + \psi_0\right) , \tag{2.72}$$

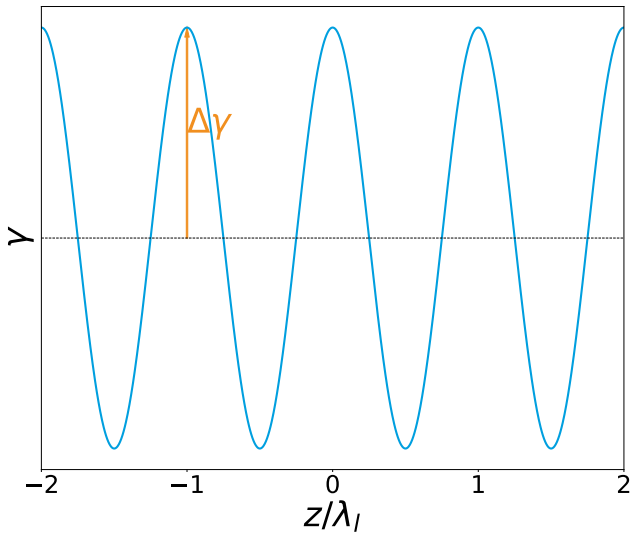

FIGURE 2.7: Longitudinal phase space of energy-modulated electron beam. For laser-induced cosine modulation the modulation amplitude is defined as shown.

where the sub-index L now indicates the laser's wavenumber k_L and angular frequency ω_L, $\mathcal{E}_0$ is the amplitude of the laser electric field and ψ_0 is a random phase. The Lorentz force $F_x = -eE_x$ is then responsible for the energy exchange described by

$$m_0c^2\frac{d\gamma}{dt} = -ev_x(t)E_x(t)\,. \tag{2.73}$$

We assume that the energy of the electron does not change significantly and its harmonic motion in $x(t)$ is unaffected and is still described by Eq. 2.66. The above equation tells us that the energy is transferred from the electron to the field or vice versa depending on the sign of the product $v_x(t)E_x(t)$. Hence, the energy exchange goes steadily in one or the other direction, if the sign remains the same throughout the undulator. Since the laser field travels by the straight trajectory with velocity c, the electron is delayed with respect to the field by the slippage length given by Eq. 2.65. The sign of $v_x(t)E_x(t)$ remains the same if this slippage length is equal to the wavelength of the laser field. The rigorous derivation of this condition from Eq. 2.73, which we skip here, introduces the *pondermotive phase*

$$\psi(t) = (k_L + k_u)\,z(t) - \omega_L t + \psi_0\,. \tag{2.74}$$

If this phase remains constant ($d\psi/dt = 0$), the energy exchange is sustained. This gives the resonant laser wavelength

$$\lambda_L = \frac{\lambda_u}{2\gamma^2}\left(1 + \frac{K_u^2}{2}\right)\,, \tag{2.75}$$

which is identical to the slippage length. The electrons inside the electron bunch have different ψ_0, depending on their position with respect to the center of the bunch. As a result, in the reference frame moving with $\bar{\beta}_\gamma$, the energy profile of the bunch acquires a cosine shape. The shape is characterized by the wavelength of the laser field and by the *modulation amplitude* $\Delta\gamma$, as illustrated in Fig. 2.7. A useful

expression to estimate the modulation amplitude is

$$\Delta\gamma = \sqrt{\frac{P_L}{P_A}}\frac{2K_u L_u \mathrm{JJ}}{\gamma w_0}, \tag{2.76}$$

where P_L is the seed laser power, $P_A = I_A m_0 c^2/e$, L_u is the total length of the undulator, I_A is the Alfvén current, $\mathrm{JJ} = J_0(\zeta/2) - J_1(\zeta/2)$ with $\zeta = K_u^2/(2+K_u^2)$ and w_0 is the transverse size of the laser beam.

While Eq. 2.76 demonstrates some important scaling laws, it can certainly be improved. In particular, we can take into account the focusing of the laser beam and the finite laser pulse duration using the expressions from Subsec. 2.3.1. Then we arrive to a more realistic expression for the energy modulation from [55]:

$$\frac{d\gamma}{d\hat{s}} = \frac{eE_0 K_u L_u \mathrm{JJ}}{2m_e c^2 \gamma}\frac{\cos\hat{\psi}}{\sqrt{1+(q\hat{s})^2}} e^{-(\hat{s}/\tau - z/c\sigma_t)^2/4}, \tag{2.77}$$

where $\hat{\psi} = 2\pi\nu\hat{s} - \arctan(q\hat{s}) + \psi_0 + k_L z$,

$$\nu = \frac{2N_u(\gamma-\gamma_r)}{\gamma_r}, \quad q = \frac{L_u}{z_R}, \quad \tau = \frac{c\sigma_t}{N_u\lambda_L},$$

$\hat{s} = s/L_u$ is the dimensionless coordinate along the undulator and $-1/2 < \hat{s} < 1/2$, σ_t is the width of the Gaussian laser pulse, z_R is the Rayleigh length of the laser beam. The detuning parameter ν can be used to include the effect of electron beam chirp on the modulation amplitude. In case of pure linear electron beam chirp the detuning parameter is the function

$$\nu(z) = \frac{2N_u}{\gamma_r}\frac{d\gamma}{dz} z. \tag{2.78}$$

It is interesting to note that due to the Gouy phase shift mentioned in Subsec. 2.3.1, the maximum modulation amplitude is achieved at a detuned energy $\gamma \neq \gamma_r$. We will keep this in mind while optimizing the modulators of the seeding section.

2.3.5 FLASH 2020+

Now that we have introduced the typical machine components, in this subsection we will discuss the layout of the future seeded FEL facility within the FLASH 2020+ project. The main features of the machine are described in [56, 57]. The schematic layout is shown in Fig. 2.8. The facility has three beamlines: FLASH1, FLASH2 and

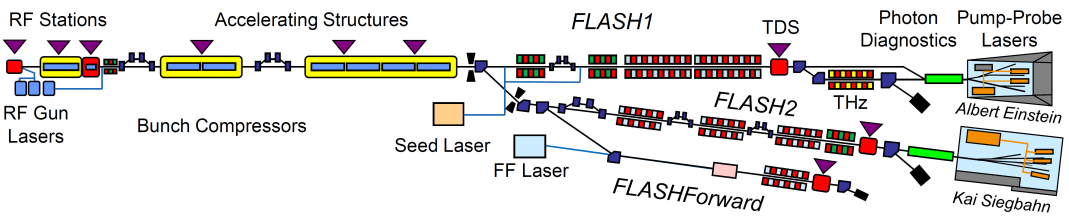

FIGURE 2.8: Schematic layout of FLASH 2020+ facility. Taken from https://flash.desy.de/

FLASHForward. The latter is reserved for a beam-driven plasma wakefield experiment [58]. FLASH2 is a SASE FEL beamline and FLASH1 is a seeded FEL beamline. All beamlines are served by a common linac. The electron bunches are generated by the injector laser and immediately accelerated in the normal-conducting RF cavity to 5.6 MeV. After that the beam is further accelerated by the superconducting accelerating module ACC1. Normally, the beam is accelerated off-crest to induce a negative chirp, as disscussed in Subsec. 2.3.2. Then, the phase space is linearized by a 3rd-harmonic cavity ACC39. After that the beam goes through the laser heater (essentially a modulator), the design and purpose of which is explained at the end of this chapter. The beam is then compressed inside the first bunch compressor chicane BC1. The typical value of the compression factor inside BC1 is 4-5. This is followed by additional acceleration in the modules ACC23, typically also off-crest to provide additional chirp for compression in BC2. After this the beam gets compressed for the second time in the second bunch compressor chicane BC2. The typical value of the compression factor is also 4-5. Finally, the beam is accelerated to the final energy by the accelerating modules ACC4567, which are commonly set on-crest. The final beam energy ranges between 750 MeV and 1.35 GeV. This is needed to cover the wavelength range of the seeded FEL radiation from 60 nm to 4 nm.

Thanks to the superconducting RF cavities, FLASH can provide high-brilliance bunches at the repetition rate of the injector laser (up to 3 MHz), making FLASH 2020+ a unique seeded FEL user facility operating at high repetition rate (up to 1 MHz given by the seed laser system). Another feature of the facility is parallel operation of the SASE FEL beamline FLASH2 and the seeded FEL beamline FLASH1. Since the two schemes typically require different compression, the FLASH2 beamline has an additional bunch compressor chicane in front of the undulators. The compression can be also to some extent controlled by flexible RF system, allowing acceleration of bunches injected in FLASH1 and FLASH2 by the same RF cavities with different amplitudes and phases.

The seeding section of FLASH1 directly follows the linac. It contains two modulators, three chicanes (only one is shown in Fig. 2.8) and the seed lasers system feeding the two modulators with two laser pulses. The spectro-temporal properties of the seeded FEL radiation are largely defined by the quality of the seed laser pulses. This puts strict requirements on the seed lasers, which need to provide wavelength tunability and typically short pulse duration. The nominal duration of the second seed laser pulse is 50 fs.

2.4 Free Electron Laser Configurations

The purpose of this section is to explain FEL process in classical theory in enough depth to understand advantages and challenges of pre-bunching techniques, in particular EEHG.

2.4.1 Laser amplifier

Equation 2.75 tells us that the electron energy and the undulator parameters have to be chosen properly to enable the amplification of an incident wave with the wavelength λ_l by the electron. In an electron bunch, though, electrons have slightly different energies. If the mean energy γ_r of the electron bunch is chosen such that Eq. 2.75 is satisfied (*resonant electron energy*), for an individual electron in the bunch we define

the relative energy deviation

$$\eta = \frac{\gamma - \gamma_r}{\gamma_r} \ll 1 \,. \tag{2.79}$$

The energy deviation has to be small for efficient amplification. Since the individual electron's energy is different from the resonant one the pondermotive phase ψ is not constant. By taking the derivative of Eq. 2.74 and using Eq. 2.61 for electron velocity v_z inside the undulator and Eq. 2.75 for γ_r, for small energy deviations η we obtain

$$\frac{d\psi}{dt} = 2k_u c\eta \,. \tag{2.80}$$

Using the newly defined η and γ_r we can also rewrite Eq. 2.73 as

$$\frac{d\eta}{dt} = -\frac{e\mathcal{E}_0 K_u}{2m_e c\gamma_r^2} \cos\psi \,. \tag{2.81}$$

The above equations are called *pendulum equations* and are very important in the FEL theory. They describe single electron's behavior in the longitudinal phase space given by the energy deviation from the resonant energy η and the pondermotive phase ψ. However, it is still unclear how this pendulum-like behavior of electrons can amplify the light wave. In fact, in a reasonable assumption that the electron distribution is uniform ($\rho(z) = \rho_0$) the net amplification along the undulator will be zero. To facilitate the amplification, the electron distribution must have density modulations of the same periodicity as the light wave

$$\rho(z) = \rho_0 + \rho_1(z)e^{i\psi(z)} \,, \tag{2.82}$$

where $\rho_1(z)$ is the amplitude of the density modulation. It also follows from Eq. 2.8 that the current $j(z)$ will have a component $j_1(z)$ with the same periodicity. The wave equations 2.11 give the relation between the electric field $\vec{E}(z)$ and $j_1(z)$. By employing *slowly-varying envelope* approximation and neglecting higher-order derivatives of $E_x(z)$ we arrive to

$$\frac{dE_x}{dz} = -\frac{\mu_0 c K_u}{4\gamma} j_1(z) \,, \tag{2.83}$$

which describes the evolution of the radiation field. The density modulations also create a longitudinal *space charge field*. From the Maxwell equations with slowly varying envelope approximation we get

$$E_z(z) = -\frac{i\mu_0 c^2}{\omega_l} j_1(z) \,. \tag{2.84}$$

Further assuming that the electron distribution is periodic in ψ we can express j_1 as the first-order Fourier component:

$$j_1 = j_0 \frac{2}{N} \sum_{n=1}^{N} \exp\left(-i\psi_n\right) \,, \tag{2.85}$$

where the index n stands for the number of individual electrons and N is the number of electrons in the bunch. As a result we can write down the coupled first-order

equations

$$\begin{aligned}
\frac{d\psi_n}{dz} &= 2k_u\eta_n\,, \\
\frac{d\eta_n}{dz} &= -\frac{e}{m_e c^2\gamma_r}\mathrm{Re}\left[\left(\frac{K_u E_x}{2\gamma_r} - \frac{i\mu_0 c^2}{\omega_l} j_1\right)\exp\left(i\psi_n\right)\right]\,, \\
j_1 &= j_0\frac{2}{N}\sum_{n=1}^{N}\exp\left(-i\psi_n\right)\,, \\
\frac{dE_x}{dz} &= -\frac{\mu_0 c K_u}{4\gamma_r} j_1\,,
\end{aligned} \tag{2.86}$$

where we assumed $d/dt = c\cdot d/dz$ and $n = 1\ldots N$. The real part operator Re appears in the above equations since the quantities j_1 and E_x are complex. This set of equations can be solved numerically for a given electron distribution and it can demonstrate the most important aspects of the FEL process. However, an analytical solution would provide more intuitive insights into the physics of FEL. The analytical solution can be derived if we make an additional assumption that the density modulations remain small. In this case ψ_n and η_n of individual electrons can be parameterized as

$$\begin{aligned}
\psi_n(z) &= \psi_n(0) + 2k_u\eta z + \mathrm{Re}\left[a(z)e^{i\psi_n(0)}\right]\,, \\
\eta_n(z) &= \eta + \mathrm{Re}\left[b(z)e^{i\psi_n(0)}\right]\,.
\end{aligned} \tag{2.87}$$

With such parameterization we essentially consider an electron beam with the central energy $\eta \neq 0$. The energy dynamics of the individual electron is represented by the complex function $b(z)$, which is the same for all electrons. Similarly, the phase dynamics is given by $a(z)$ on top of the linear term. The individuality of each electron is then reduced to their initial phases $\psi_n(0)$. Considering $a(z)$ and $b(z)$ as small, we can employ the perturbation approach to rewrite the set of equations as a third-order differential equation with respect to E_x:

$$E_x''' + i4k_u\eta E_x'' + \left(k_p^2 - 4k_u^2\eta^2\right)E_x' - i\Gamma^3 E_x = 0\,, \tag{2.88}$$

where the prime operator $'$ stands for d/dz,

$$\Gamma = \left(\frac{\mu_0 K_u^2 e^2 k_u n_e}{4\gamma_r^3 m_e}\right)^{1/3} \tag{2.89}$$

is the gain parameter and

$$k_p = \sqrt{\frac{2\lambda_l}{\lambda_u}}\frac{\omega_p^*}{c} \tag{2.90}$$

is the space charge parameter with ω_p^* being the plasma frequency in the rest frame of the bunch

$$\omega_p^* = \sqrt{\frac{n_e e^2}{\gamma_r \epsilon_0 m_e}}\,. \tag{2.91}$$

Our goal here is to demonstrate that Eq. 2.88 has a solution, that results in amplification of the field. For this purpose, we consider on-resonance electrons $\eta = 0$ and assume that the gain parameter Γ is large enough to neglect the term with k_p. In this

case Eq. 2.88 reduces to

$$E_x''' - i\Gamma^3 E_x = 0\,. \tag{2.92}$$

By looking for solutions of this equation in the form of $E_x(z) = Ae^{\alpha z}$ we can show that there is a solution with a positive real part of α, which means exponential growth of the field amplitude. More commonly one speaks about the power gain, characterized by the *gain length*

$$L_g = \frac{1}{\sqrt{3}\Gamma}\,. \tag{2.93}$$

Assuming the initial electron density modulation $j_1(0) = 0$ and the initial field amplitude $E_x(0)$ given by the power of the incident laser field P_{in}, the output power is estimated as

$$P_{\text{out}} = \frac{P_{\text{in}}}{9} e^{z/L_g}\,. \tag{2.94}$$

The factor $1/9$ in the above equation originates from the fact that the "gain" solution is one of the three possible solutions and the incident field amplitude $E_x(0)$ is distributed among them. Another consequence of the existence of the other solutions is that the gain does not kick in immediately. It takes typically on the order of $2L_g$ of distance inside the undulator for the gain component to assert dominance and for Eq. 2.94 to become valid. The exponential gain continues until $\approx$ 20 gain lengths. After that the gain reaches saturation, where the electrons lose as much energy to the radiation as they gain from the radiation. In the saturation regime our assumption of high gain parameter Γ fails and Eq. 2.92 is no longer valid. The FEL radiation power oscillates around a value called *saturation power* P_{sat}.

Using the gain parameter Γ we can introduce the so-called Pierce parameter

$$\rho_{\text{FEL}} = \frac{\Gamma}{2k_u}\,. \tag{2.95}$$

The same quantity can be written down in more practical terms

$$\rho_{\text{FEL}} = \left(\frac{1}{\gamma^3}\frac{I}{I_A}\frac{\lambda_u^2}{2\pi\sigma_x^2}\frac{\text{JJ}^2}{32\pi}\right)^{1/3}\,. \tag{2.96}$$

This quantity can be used for estimation of FEL bandwidth, i.e., the maximum allowed relative energy deviation for an electron to participate in the FEL gain. The same quantity defines the maximum power that can be extracted from the electron beam in the form of FEL light. If we introduce the beam power as

$$P_e = \frac{\gamma m_e c^2 I_0}{e}\,, \tag{2.97}$$

the maximum extracted power can be approximated by

$$P_{\text{sat}} \sim \rho_{\text{FEL}} P_e\,. \tag{2.98}$$

Effect of energy spread

The expressions for the saturation power P_{sat} and the gain length L_g are derived without taking into account several aspects of electron and radiation beams, e.g., the transverse distribution of the electron beam and natural diffraction of the radiation field. Most importantly for this work, the contribution of the electron beam energy

spread is neglected. The effect of these factors can be formulated [59] in terms of increased gain length

$$L_g^* = \frac{L_g}{\chi} \tag{2.99}$$

and decreased saturation power

$$P_{\text{sat}}^* = \chi^2 P_{\text{sat}}\,, \tag{2.100}$$

where the function χ depends on the additional factors that we want to include. If we want to include only the energy spread σ_E, according to [60]

$$\chi(\sigma_E) = \frac{\exp\left(-a\tilde{\mu}_E^2\right)}{1 + b\tilde{\mu}_E^2}\,, \tag{2.101}$$

where $a = -3.4 \cdot 10^{-2}$, $b = 0.185\dfrac{\sqrt{3}}{2}$ and

$$\tilde{\mu}_E = 2\frac{\sigma_E}{E_0 \rho_{\text{FEL}}}\,. \tag{2.102}$$

2.4.2 Start-up of FEL

The example of the FEL laser amplifier allows to demonstrate the basic FEL physics, but it immediately raises the question of the source of the initial field. In particular, in the highly demanded spectral range of XUV and soft X-rays the choice of high-power sources is very limited. Equations 2.86 tell us that the FEL process can be also initiated by the initial electron density modulations. Assuming considerable $j_1(0) \neq 0$ and $E_x(0) = 0$ as the initial conditions, the third-order FEL equations can be solved in a similar way as for the laser amplifier. Unlike the previous case, for the initial density modulation the radiation power starts to grow from 0 immediately. After $\approx 2L_g$ it enters the exponential gain regime.

This promising alternative, in turn, raises the question of where would the density modulations come from. One possible answer to this question is *shot noise*. In reality, the electron distribution is never truly smooth and has a very rich spectral content, which also includes modulations at the target wavelength (whatever we choose it to be). Admittedly, these initial modulations are quite small and can not dominate the radiation field evolution given by the coupled equations. The electrons radiate undulator radiation, described in Subsec. 2.3.4, independently from each other. This radiation is called *spontaneous radiation*. The spontaneous radiation from the first $2L_g$ of the undulator acts as the initial radiation in the following sections of the undulator. We have to keep in mind, however, that the spontaneous radiation is not a monochromatic wave, as we assumed before. The properties of the resulting FEL radiation are derived from the stochastic nature of the spontaneous radiation. In particular, the spectral properties and the output power show considerable shot-to-shot jitter.

In order to overcome the limitations of SASE, we can use pre-bunching techniques. For this, the radiator has to be preceded by a dedicated seeding section, which typically consists of modulators with external lasers and dispersive elements. There are two such schemes: HGHG and EEHG. The latter one consists of two modulators and two chicanes, while the first one needs only one of each. Since the focus of this work is EEHG, we will discuss EEHG in detail and refer to other works for comparison of the two techniques, e.g., [19]. The most important advantage of

EEHG in comparison to HGHG is the possibility of reaching high harmonics of the seed laser (on the order of 100). Aiming at such high harmonics of the seed laser is necessary to operate seeded FEL in soft X-ray range, since high-power laser sources typically do not reach wavelengths shorter than UV.

Optimization of an idealized EEHG setup

In order to understand the principle of EEHG and introduce the most important concepts we assume the beam phase space distribution to be

$$f_0(z,p) = f(z)\sqrt{2\pi}e^{-p^2/2}, \tag{2.103}$$

where $p = (E - E_0)/\sigma_E$. The initial longitudinal phase space for such a beam is illustrated in Fig. 2.9 (a). First, the electron beam is energy-modulated in the first

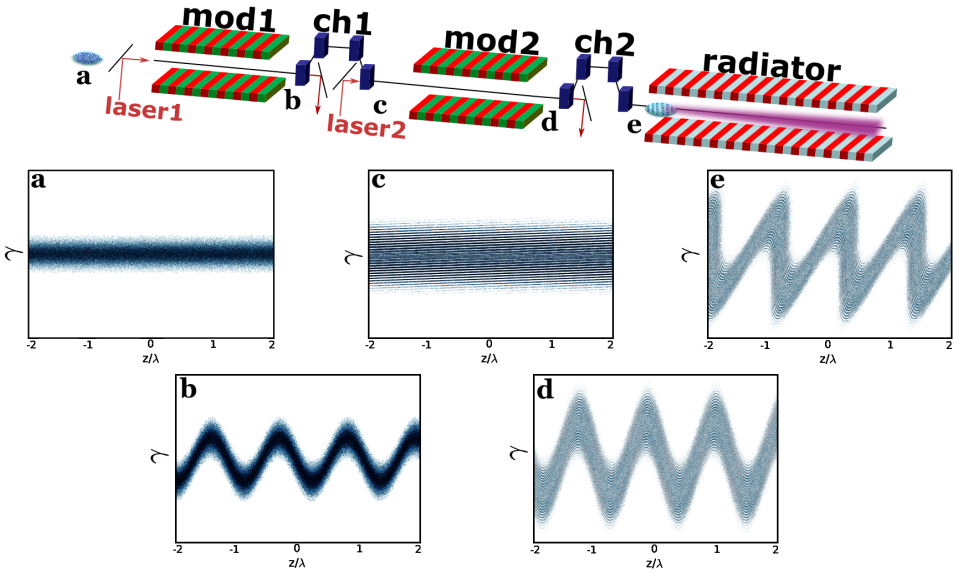

FIGURE 2.9: Schematic representation of EEHG FEL set-up and phase space transformations. The color scale in sub-plots a-e is arbitrary and intended for illustration purposes only.

modulator (mod1) to modulation amplitude $A_1 = \Delta E_1/\sigma_E$, as shown in Fig. 2.9 (b). Then, the beam goes through the first dispersive section (ch1). The longitudinal dispersion in ch1 is relatively high and characterized by $B_1 = k_1 R_{56}^{(1)} \sigma_E/E > 0$. The modulation is over-sheared and filamentation of the longitudinal phase space appears, as shown in Fig. 2.9 (c). This striped structure of the longitudinal phase space is distinctive to the EEHG seeding scheme and is the source of its greatest advantages and challenges, as will be discussed later. Then, the beam is energy-modulated again in the second modulator (mod2) to $A_2 = \Delta E_2/\sigma_E$, as shown in Fig. 2.9 (d). Finally, the density modulations at the target wavelength are created by applying $B_2 = k_1 R_{56}^{(2)} \sigma_E/E > 0$ in the second dispersive section (ch2) to the energy-modulated beam. Intuitively, the combination of mod2 and ch2 rotates the (almost) horizontal stripes in Fig. 2.9 (c) to make them vertical. If we project the phase space shown in Fig. 2.9 (e) on the z-axis, we see that those vertical stripes are essentially density spikes. If the spikes are separated by the target wavelength, they are essentially the density modulation at the target wavelength.

The evolution of the phase space can be written as

$$\begin{aligned} P_1 &= P + A_1 \sin(k_1 z) \\ z_1 &= z + B_1 P_1 / k_1 \\ P_2 &= P_1 + A_2 \sin(k_2 z_1) \\ z_2 &= z_1 + B_2 P_2 / k_2 . \end{aligned} \tag{2.104}$$

Applying the transformations above to the initial beam distribution (Eq. 2.103) we arrive to the final beam distribution at the exit of the second chicane:

$$\begin{aligned} f_f(z,p) = f(z)\sqrt{2\pi}\exp\Bigg\{ -\frac{1}{2}\Big[p - A_2 \sin\left(Kk_1 z - KB_2 p\right) \\ - A_1 \sin\Big[k_1 z - \left(B_1 + B_2\right) p + A_2 B_1 \sin\left(Kk_1 z - KB_2 p\right)\Big]\Big]^2 \Bigg\} \end{aligned} \tag{2.105}$$

which can be then integrated over p to obtain beam density distribution

$$N(z) = \int_{-\infty}^{\infty} f_f(z,p) dp \, . \tag{2.106}$$

The efficiency of pre-bunching the beam is then evaluated as bunching factor

$$b_{n,m} = |\langle N(z) e^{-i(n+Km)k_1 z} \rangle| = \bar{b}_{n,m} \tag{2.107}$$

Skipping the derivation we arrive to a useful formulation of the bunching close to the target harmonic:

$$b_{n,m}(k) = \bar{b}_{n,m}(k) \int dz f(z) e^{-iz(k-k_E)} \, , \tag{2.108}$$

where $k_E = a_E k_1$ is the wavenumber of the target harmonic. This way we separate spectral properties given by the integral term from the amplitude envelope defined by optimization of the working point. The bunching envelope at the target harmonic for an idealized EEHG lattice is

$$\bar{b}_{n,m} = \left| e^{-\xi_E^2/2} J_n\left(-\xi_E A_1\right) J_m\left(-a_E A_2 B_2\right) \right| \, , \tag{2.109}$$

where $a_E = n + mk_2/k_1$ is the harmonic number, n and m are integer numbers and $\xi_E = nB_1 + a_E B_2$. ξ_E is the EEHG scaling parameter and it is typically advantageous to minimize its absolute value. Numerically this happens approximately at $\xi_E = j'_{n,1}/A_1$, where $j'_{n,1}$ is the first root of J'_n. Typically a larger A_1 helps to minimize ξ_E, but one should keep in mind the detrimental effect of the uncorrelated energy spread on the FEL performance. The EEHG working point is basically defined by the choice of $A_{1,2}$. The optimal value of $B_{1,2}$ are then given by

$$B_2 = \frac{j'_{m,1}}{a_E A_2} \, , \quad B_1 = \left(\xi_E - a_E B_2\right)/n. \tag{2.110}$$

During the optimization procedure one should also keep in mind that $R_{56}^{(2)}$ includes dispersion not only of the second chicane, but also that of the second modulator. The latter can be easily calculated, considering that for the resonance condition (Eq. 2.75)

to be fulfilled, the electron beam should be delayed by λ_2 per modulator period. This consideration is slightly complicated by the fact that the modulation grows continuously inside the modulator. Hence, if we want to isolate the contribution of R_{56} of the modulator to B_2 in the above equations, we need to integrate the product of $A_2(s)B_2(s)$ over the beamline coordinate s. Assuming that the energy modulation grows linearly inside the modulator, as implied by Eq. 2.76, the integral

$$\int_{\text{mod2}} A_2(s)B_2(s)ds$$

can be replaced by effective value $A_2B_2|_{\text{mod2}}/2$. In other words, $R_{56}^{(2)}$ is a sum of R_{56} of ch2 and a half of R_{56} of mod2.
In the start-up regime the power of the coherent radiation from the pre-bunched beam starts to grow inside the FEL amplifier according to [59]

$$P(z) = \frac{1}{3}\rho_{\text{FEL}}|b_{n,m}|^2 P_e \left(\frac{z}{L_g}\right)^2 . \tag{2.111}$$

An important conclusion from Eq. 2.111 is that the properties of the start-up radiation, which is later amplified by the exponential FEL gain, are derived from the properties of the bunching defined by Eq. 2.107.

EEHG with energy modulations

The idealized setup above can be generalized to include unwanted energy modulations. However, it is important to distinguish the modulations appearing upstream of the first chicane (Δp_1) or downstream of it (Δp_2):

$$\begin{aligned} P_1 &= P + A_1(z)\sin(k_1 z) + \Delta p_1(z) \\ z_1 &= z + B_1 P_1/k_1 \\ P_2 &= P_1 + A_2(z_1)\sin(k_2 z_1) + \Delta p_2(z_1) \\ z_2 &= z_1 + B_2 P_2/k_2 \,. \end{aligned} \tag{2.112}$$

The term Δp_1 then can be used to capture electron beam energy correlations from the linac, in particular linear chirp and curvature. The effect of both was investigated in detail [19, 61, 39]. Here we highlight the most important conclusions form those studies.
The expression for the bunching spectrum is modified as

$$b_{n,m}(k) = \exp\left[-\frac{1}{2}\left(\zeta_E + \frac{k-k_E}{k_1}B\right)^2\right] \times \tag{2.113}$$

$$\int_{-\infty}^{+\infty} dz f(z) J_m\left[-\frac{k}{k_1}B_2A_2(z)\right] J_n\left[-\left(\zeta_E + \frac{k-k_E}{k_1}B\right)A_1(z)\right] \times \tag{2.114}$$

$$\exp\left[i\left[-\zeta_E\Delta p_1 + (k-k_E)\right]\right], \tag{2.115}$$

where $B = B_1 + B_2$. The generalized bunching envelope can be then defined as

$$\bar{b}_{n,m}(k) = e^{-\xi^2(k)/2} J_n\left[-\xi(k)A_1(0)\right] J_m\left[-kA_2(0)B_2/k_1\right] , \tag{2.116}$$

with

$$\xi(k) = \frac{k}{k_1} B - mKB\,, \tag{2.117}$$

where $K = k_2/k_1$ and $A_{1,2}(0)$ are assumed to correspond to the design working point values. With the linear chirp characterized by the dimensionless parameter

$$h_1 = \frac{dE}{dz}\frac{1}{k_1\sigma_E} \tag{2.118}$$

the modulation $\Delta p_1(z)$ becomes

$$\Delta p_1(z) = h_1 k_1 z \tag{2.119}$$

and the peak of the bunching spectrum shifts to

$$a = \frac{n + mK(1 + h_1 B_1)}{1 + h_1 B}\,. \tag{2.120}$$

For the original set-up optimized for non-chirped case we will also observe a decrease in the bunching amplitude. However, we can easily obtain the same bunching amplitude as in the original set-up by adjusting $R_{56}^{(2)}$. With pure linear chirp the spectral width at the target harmonic becomes

$$\sigma_{h1} = \frac{\sigma_0}{1 + mKh_1 B_1/a_E}\,. \tag{2.121}$$

With pure quadratic chirp in small curvature regime the spectral width becomes

$$\sigma_{h2} = \sigma_0\left(1 + \chi_E^2/2\right)\,, \tag{2.122}$$

where $h_2 = \dfrac{d^2E}{dz^2}\dfrac{1}{2\sigma_E k_1^2}$ is dimensionless quadratic correlation and $\chi_E = 2\xi_E h_2 k_1^2 \sigma_z^2$. The effects of the linear chirp will be illustrated and estimated for the 4 nm EEHG set-up at FLASH in Ch. 3. Generally speaking, EEHG is known to be less sensitive to Δp_1 than HGHG.

However, Δp_2, which doesn't exist for HGHG, can be far more detrimental. In order to estimate its effect on EEHG efficiency, we can represent it as a Fourier series:

$$\Delta p_2 = \sum_{\mu=0}^{\infty} p_2(k_\mu)\sin(k_\mu z + \varphi_{2\mu})\,, \tag{2.123}$$

where k_μ are discrete wavenumbers, $p_2(k_\mu)$ are corresponding amplitudes and φ_μ are random phases. The bunching amplitude is then modified to

$$\begin{aligned} b_{nm}(k) =& \bar{b}_{nm}(k) \times \\ & \prod_{\mu=0}^{\infty}\sum_{l_1=-\infty}^{\infty}(-1)^{l_1} J_{l_1}(-a_E B_2 p_2(k_\mu)) e^{-il_1\varphi_{2\mu}}\,. \end{aligned} \tag{2.124}$$

From the equation above we can derive the modified bandwidth of the bunching profile:

$$\sigma_k^2 = \bar{\sigma}_k^2 + \sum_{\mu=0}^{\infty}\left[\frac{(a_E B_2)^2}{2}\left(p_2(k_\mu)k_\mu\right)^2\right]\,, \tag{2.125}$$

where the first term represents the bandwidth in the absence of Δp_2.

EEHG with finite seeds

In Subsec. 2.4.2 we assumed that the laser field in the modulators is a pure plane wave. In other words, we assumed the laser pulse duration to be infinite in both modulators. If the seed laser pulse is finite, only a part of the electron bunch is effectively seeded. From Eq. 2.109 we can conclude that the length of the seeded part is defined by the widths of the central peak of the Bessel functions $J_{m,n}$. For a well-optimized EEHG set-up at a high harmonic number the width of J_m is typically much smaller. This is certainly true if the duration of the first seed laser pulse is infinite or much longer than the second seed laser pulse.

The effective length of the bunch σ_z^{eff} can be approximately related to the duration of the seed σ_{s2} by [62]

$$\sigma_z^{\text{eff}} \approx \frac{7}{6}\frac{\sigma_{s2}}{m^{1/3}}\,. \tag{2.126}$$

2.5 Impact of Collective Effects on Beam Dynamics

The purpose of this section is to introduce different collective effects considered in this work to answer some essential questions:

- how can one picture this collective effect?
- what is its potential implication for EEHG?
- what could be the mitigation strategy?

The collective effects under consideration can be independently subdivided by two criteria: (i) radiative or non-radiative; (ii) correlated or uncorrelated. Four permutations of these two criteria give us four collective effects explained in more detail below (IBS, ISR, LSC and CSR). Microbunching instability can be considered as a separate phenomenon, however, due to its close connection to LSC and CSR it has been added to this section as well.

2.5.1 ISR

From Lienard-Wiechert potential we can derive average power emitted by an electron due to accelerated motion [63]. Longitudinal acceleration typically results in negligible amount of radiated power. For transverse acceleration (bending) the level of radiated power is far more significant. In our setup the bending mostly takes place in the chicanes. Therefore, we can estimate average power emitted by a particle inside a dipole of a chicane by [64]:

$$P = \frac{e^2 c}{6\pi\epsilon_0}\frac{1}{(m_0c^2)^4}\frac{E^4}{R^2}\,, \tag{2.127}$$

where R is the bending radius, ϵ_0 is vacuum permittivity, E is the energy of the particle. The important conclusion from Eq. 2.127 is that the emitted power grows as E^4. This means that the effects of synchrotron radiation become rapidly more important as the particle is accelerated to high energies. Since the energy emitted by radiation is equivalent to the particle energy loss, synchrotron radiation is an important aspect of the beam dynamics.

Equation 2.127 allows to calculate total energy loss by a particle beam while traversing certain trajectory. In linear machines the synchrotron radiation from dipoles is typically considered as a detrimental effect, which spoils the beam quality. To understand the mechanism behind it we have to remember that Eq. 2.127 is derived in classical treatment and does not take into account the quantum nature of the light emission. In the quantum treatment single photons of different energies are emitted by single electrons at different moments of time while passing a bending dipole. Such a treatment is formulated in [17] and predicts energy diffusion of the particle bunch. The energy diffusion leads, in turn, to diffusion in relative longitudinal position of particles within the bunch. In context of FELs this can lead to smearing of bunching, if the longitudinal diffusion is comparable to the bunching wavelength, as explained in [65]. The same concept is applied to EEHG scheme in [31] in a detailed tutorial-like manner. We will follow the latter work to explain the calculation procedure for EEHG bunching diffusion due to ISR.

The energy diffusion can be understood as random energy kicks applied to a particle at different points in the beamline. This is somewhat similar to adding $\Delta p_{1,2}$ in Eqs. 2.112, except in this case the kicks are not a function of z and have stochastic nature instead. The last of Eqs. 2.112 will be then:

$$z_2 = z_1 + B_2 P_2 / k_2 + \frac{[B_*(s)\Delta p_*(s)]}{k_2}\,, \tag{2.128}$$

where $\Delta p_*(s)$ is the amplitude of the random kick obtained at beamline coordinate s and

$$B_*(s) = \begin{cases} \zeta_E & \text{before ch1}\,, \\ \zeta_E + (B_2 - \zeta_E)\frac{B(s)}{B_1} & \text{inside ch1}\,, \\ B_2 & \text{between chicanes}\,, \\ B_2\left(1 - \frac{B(s)}{B_2}\right) & \text{inside ch2}\,, \\ 0 & \text{after ch2}\,, \end{cases} \tag{2.129}$$

where $B(s)$ represents the fraction of corresponding chicane's longitudinal dispersion up to the beamline coordinate s. The last term in Eq. 2.128 results in an additional factor to the bunching:

$$\langle e^{-iB_*(s)\Delta p_*}\rangle = e^{-iB_*(s)\langle\Delta p_*\rangle} e^{-\frac{1}{2}B_*^2(s)\Delta p_{*\mathrm{RMS}}^2} \tag{2.130}$$

First, we estimate the bunching suppression due to ISR inside the chicanes. For simplicity we want to lump the effect to the exit of each chicane. In order to do this, we need to introduce a number of assumptions. We assume that the beamline is optimized well enough to neglect ζ_E in Eq. 2.129. Another assumption is that the dispersion is distributed along the chicanes in a symmetric way. This allows to replace s-dependent parts in Eq. 2.130 by constant values and finally get to corrected bunching envelope:

$$\tilde{b}_{n,m} = \bar{b}_{n,m} \exp\left(-\frac{i}{2}B_2\langle\Delta p_*\rangle\right) \exp\left(-\frac{1}{2}B_2^2 f_{ISR}\Delta p_{*\mathrm{RMS}}^2\right)\,, \tag{2.131}$$

where

$$f_{ISR} = \frac{\frac{158}{7} + 69\frac{l_d}{l_b} + 54\frac{l_d^2}{l_b^2}}{64\left(1 + \frac{3l_d}{2l_b}\right)^2}\,, \tag{2.132}$$

where l_b is the length of the chicane dipole and l_d is the length of the central drift (GENESIS convention). The average energy loss $\langle \Delta p_* \rangle$ is given by Eq. 2.127 integrated over electron path through the four magnets of the chicane and

$$\Delta p_{*\mathrm{RMS}}^2 = \frac{55 r_e^2}{24\sqrt{3}\alpha} \gamma^5 \left(4 l_b\right) \left(\frac{e\mathcal{B}}{m_e v \gamma}\right)^3 \frac{E^2}{\sigma_E^2}, \tag{2.133}$$

where r_e is the classical electron radius, α is the fine structure constant, $\mathcal{B}$ is the magnetic field. The complex exponential term in Eq. 2.131 would be responsible for wavelength shift with respect to the target wavelength, but would not suppress the bunching amplitude. For this reason we will focus on the second exponential term, which we denote as

$$\eta_{ISR} = \exp\left(-\frac{1}{2} B_2^2 f_{ISR} \Delta p_{*\mathrm{RMS}}^2\right). \tag{2.134}$$

The bunching suppression caused by ISR can be also estimated for the modulators. For the first modulator, however, ISR-induced energy spread can be simply considered as an increase to the initial energy spread σ_E, as follows from Eq. 2.129. The energy spread gained in the second modulator enters Eq. 2.130 with a much larger factor B_2, illustrating sensitivity of EEHG to intermediate phase space diffusion. For a modulator

$$\Delta p_{*\mathrm{RMS}}^2 = 4 L_u d_{ISR}^2 / \left(3\pi\rho_u^3\right) \frac{E^2}{\sigma_E^2}, \tag{2.135}$$

where L_u is the length of the modulator,

$$d_{ISR} = r_e \left(\frac{55\gamma^5}{24\sqrt{3}\alpha}\right)^{1/2}, \tag{2.136}$$

and bending radius inside the modulator

$$\rho_u = \frac{m_e v \gamma}{e\mathcal{B}_u}, \tag{2.137}$$

where $\mathcal{B}_u$ is the peak magnetic field.

Analyzing the equations above, we can conclude that the effect of ISR scales strongly with the electron beam energy and would be substantially reduced at lower beam energy. However, the beam energy is dictated by the requirements for FEL operation and is not a free parameter for optimization of the seeding section. Another option for mitigating the effect of ISR can be the adjustments in the chicanes. In particular, we can try to change the geometry of the chicanes while keeping their R_{56} constant or vice versa. Of course, the layout of the chicanes has to be decided during the design phase and can hardly be considered as a free parameter during the operation.

2.5.2 IBS

Intra-beam scattering can be understood as momentum exchange between electrons due to random one-on-one collisions within the bunch. Generally speaking, the momentum exchange happens in all three planes (x', y', p). However, we can make the same argument as in [33] that for high energy X-ray FEL driver beams the momentum diffusion in transverse planes is negligible compared to the initial widths of

the distributions $\sigma_{x'}$ and $\sigma_{y'}$, which are mostly defined by the photo-cathode emission. For this reason, we will restrict the discussion of the effect of IBS on the energy spread. For the analytical estimation we will again follow [31].

The analytical treatment of bunching suppression due to IBS is very similar to that for ISR. The difference between the two is that there is no net energy loss due to IBS, therefore for IBS we naturally have $\langle \Delta p_{*\mathrm{RMS}} \rangle = 0$. One other difference is that IBS takes place not only inside the dipoles, but also in drift spaces. The energy diffusion due to IBS in a chicane is

$$\Delta p^2_{*\mathrm{RMS}} = L/L_{IBS} \left(\frac{\beta_{\mathrm{nom}}}{\beta} \right)^{1/2}, \tag{2.138}$$

where L is the length of the chicane β_{nom} is the nominal (or average) value of the beta function,

$$L_{IBS} = \frac{2}{\pi^{1/2} \ln \Lambda} \frac{\epsilon_N^{3/2} \gamma^{3/2} \beta_{nom}^{1/2}}{r_e I / I_A}, \tag{2.139}$$

where ϵ_N is the normalized emittance, I is the peak current of the bunch, I_A is Alfvén current and

$$\Lambda = \frac{2\lambda_D}{\gamma} \frac{I}{ec} \frac{\rho_{FEL} \beta}{2\gamma\sigma_x}, \tag{2.140}$$

where λ_D is the Debye length given by

$$\lambda_D = \sqrt{\frac{\sigma_x^2}{4\pi r_e n_e}}, \tag{2.141}$$

where n_e is the electron density. The argument of the logarithm term in Eq. 2.139 calls for some additional comments. The term originates from the calculation of scattering amplitudes between two particles. The scattering amplitude depends on the so-called impact parameter, i.e., the transverse offset between the scattered particle and the "target". The final expression contains the term $\ln(b_{max}/b_{min})$, where b_{min} and b_{max} are the minimal and the maximal considered values of the impact parameter. There is some ambiguity in the choice of these two values. Here, for the maximum value we calculate the Debye length for a narrow cylindrical beam (Eq. 2.141). Beyond the Debye length the Coulomb force between two electrons would be screened by other electrons to $1/e$ of its amplitude. The minimum impact parameter value is chosen such, that the momentum exchange in the single scattering event would kick the scattered electron out of the FEL bandwidth, estimated by ρ_{FEL}. The latter can be estimated by Eq. 2.96. Since in this work we do not consider the FEL amplifier in detail, we can simply take a typical value of $\rho_{FEL} \approx 10^{-3}$. Such laxity can be further justified by arguing that the logarithm is a slowly-varying function and the choice of the cut-off typically does not fundamentally change the results of the IBS calculations [33].

The effect of IBS on EEHG bunching is represented by the factor

$$\eta_{IBS} = \exp\left(-\frac{1}{2} f_{IBS} \Delta p^2_{*\mathrm{RMS}} B_2^2 \right), \tag{2.142}$$

where

$$f_{IBS} = \frac{\frac{158}{7} + 99\frac{l_d}{l_b} + 144\frac{l_d^2}{l_b^2} + 69\frac{l_d^3}{l_b^3}}{64\left(1 + \frac{5l_d}{4l_b}\right)\left(1 + \frac{3l_d}{2l_b}\right)^2}. \tag{2.143}$$

The effect of IBS can be also estimated for the second modulator or, to be precise, for the space in between the two chicanes. In this case the factor becomes

$$\eta_{IBS} = \exp\left(-\frac{1}{2}\Delta p_{*\mathrm{RMS}}^{2} B_2^2\right), \tag{2.144}$$

and L in Eq. 2.138 becomes the distance between the chicanes.

Analyzing the equations above, we see that the effect of IBS scales strongly with the overall length of the seeding section. Unfortunately, in a realistic machine the overall size is hardly a subject to change. Hence, as in the case of ISR, we are restricted to adjustments of geometrical and dispersive properties of the chicanes.

2.5.3 CSR

When the electron beam traverses a bending magnet, the radiation emitted by the tail electrons can catch up with the head electrons. Such dipole radiation is quite broad in spectrum and can be considered as a sum of spectral components. Some of those components can interact with the electron beam in a coherent way, if there is an electron density modulation (i.e., bunching) at the same wavelength. For wavelengths longer than the electron bunch itself there is always significant bunching, which is why CSR at such wavelengths is generally present and manifests itself as an energy modulation of the electron bunch. This modulation is commonly referred to as "wake". Although the term is somewhat different from the definition in Subsec. 2.2.5, the mathematical treatment is identical.

In the FEL community CSR is typically considered as a detrimental effect in the linac, in particular in bunch compressors. The effect of CSR on beam dynamics can be basically traced back to CSR-induced energy kicks and consequent beam transport. We can imagine a reference particle following the design trajectory in the phase space. If this particle obtains a small energy kick due to CSR it will no longer follow the design trajectory, but will start to oscillate around it. These oscillations in transverse phase space ($x - x'$ and $y - y'$) effectively increase the area occupied by the particle, which results in an increase in transverse emittance [66, 67]. Since the CSR kicks are longitudinally correlated, unlike for ISR and IBS, they do not directly contribute to uncorrelated energy spread. Instead, these correlated energy kicks can be converted to electron density modulations by R_{56} of the lattice [68, 69]. This effect is known as microbunching, which is discussed in the next section.

However, CSR takes place not only in the linac, but basically everywhere in the beamline, including the seeding section. The problem of CSR is especially relevant for EEHG for two reasons. One is that the over-shearing chicane has to be quite strong, which generally favours radiation forces. The second is that the wake obtained in the first chicane would enter the EEHG equations as Δp_2, which is potentially dangerous, as was mentioned in Subsec. 2.4.2. Therefore, in order to estimate the effect of CSR on EEHG performance it is essential to calculate the CSR wake.

There are several models for CSR calculation, so the choice of models used in this work should be explained. In principle, one could calculate the radiative interaction between particles directly from retarded Lienard-Wiechert potential [70]. While this approach implies fewer simplifications compared to other models, practical use of this approach has numerical limitations. In particular, it is necessary to store the history of radiation fields through a large time window.

Many models are based on the fundamental work [20]. One common approximation in these models is 1D-approximation, which neglects the transverse distribution

of the electron beam. The adequacy of this approximation can be estimated by the criterion[66]

$$\sigma_\perp \sigma_z^{-2/3} R^{1/3} \ll 1\,, \tag{2.145}$$

where $\sigma_\perp$ is the transverse beam size, σ_z is the bunch length, and R is the bending radius. This criterion is typically fulfilled for moderately compressed electron beams [71], such as ones used in seeded FELs. Existing 1D models can be further subdivided into categories based on additional underlying assumptions. Below we give formulations of the models used in this work using impedance formalism.

Free space steady-state CSR model

So-called free space (FS) models do not take into account the effects of the vacuum chamber. The applicability of such models is defined by

$$\sigma_z \ll 1/k_{th}\,, \qquad k_{th} = \pi\sqrt{R/h^3}\,, \tag{2.146}$$

where h is the height of the chamber and k_{th} is the threshold wavenumber. The significance of k_{th} is that the radiation components below the threshold value are strongly suppressed due to the boundary conditions given by the chamber. Since the coherent part of the radiation is located in $\lambda \geq \sigma_z$ spectral region (in the absence of microbunching), the CSR wake is effectively suppressed. Assuming the condition is fulfilled, the CSR impedance for FS-SS model is given by [72]

$$Z_{FS}(k) = (-0.94i + 1.63)\frac{Z_0 k^{1/3}}{4\pi R^{2/3}} l_b\,, \tag{2.147}$$

where $Z_0 = 377\ \Omega$ is the impedance of free space and l_b is the length of the bending magnet.

Parallel-plates steady-state CSR model

If the condition given by Eq. 2.146 is not fulfilled, one should consider using a model which takes the chamber into account. The simplest of them is steady-state parallel plates (PP) model, where the beam is assumed to traverse the bend in the middle between two perfectly conducting infinite parallel plates. In this case the impedance can be written as [73]:

$$\begin{aligned} Z_{PP}(k) =& \frac{2\pi Z_0}{h}\left(\frac{2}{kR}\right)^{(1/3)} l_b \times \\ & \sum_{\nu=0}^{\infty}\Big\{ \mathrm{Ai}'(X_\nu^2)\left[\mathrm{Ai}'(X_\nu^2) - i\mathrm{Bi}'(X_\nu^2)\right] + \\ & X_\nu^2 \mathrm{Ai}(X_\nu^2)\left[\mathrm{Ai}(X_\nu^2) - i\mathrm{Bi}(X_\nu^2)\right]\Big\}\,, \end{aligned} \tag{2.148}$$

where $\nu = 0, 1, 2...$, Ai and Bi are Airy functions of the first and the second kind, respectively, and

$$X_p = \frac{(2\nu+1)\pi}{h}\left(\frac{R}{2k^2}\right)^{1/3}.$$

Free space CSR model with transient effects

The FS-SS model given by Eq. 2.147 implies that the tail-head interaction takes place (only) inside the bend with constant efficiency per unit length of the trajectory. This can be a good approximation for long bends, where CSR interaction reaches saturation and can indeed be assumed to grow linearly with the distance inside the bend. A more general consideration also takes into account the interactions which happen within the electron beam as it enters and leaves the bend. The importance of these so-called transient effects can be significant for shorter bends. This can be explained by the explicit formulations of CSR wakes inside the bending magnet explained in [74] in context of the particle tracking code `ELEGANT` [75] and originally formulated in [20]. The longitudinal wake function of a bunch $W_{\parallel b}$ is given by

$$\frac{\partial W_{\parallel b}(s,z)}{\partial s} = T_1(s,z) + T_2(s,z), \tag{2.149}$$

where T_1 is the steady-state CSR component, and T_2 is the entrance transient part. The two terms are given by

$$T_1(s,z) = K \int_{z-z_L}^{z} \frac{d\lambda(s,z')}{dz'} \left(\frac{1}{z-z'}\right)^{1/3} dz', \tag{2.150}$$

$$T_2(s,z) = K \frac{\lambda(s,z-z_L) - \lambda(s,z-4z_L)}{z_L^{1/3}}, \tag{2.151}$$

where s is measured from the entrance of the bend, the slippage length z_L is given by

$$z_L = \frac{s^3}{24R^2} \tag{2.152}$$

and the scaling factor K by

$$K = \frac{Z_0 c}{4\pi} \frac{2}{(3R^2)^{1/3}}. \tag{2.153}$$

From Eqs. 2.151-2.152 we can conclude that, generally speaking, with increasing distance into the magnet $T_2(s)$ plays increasingly less important role in Eq. 2.149. This can be illustrated on a specific example. In Fig. 2.10 the instantaneous values of $T_{1,2}(s,z)$ are compared for $R = 10.7\,\mathrm{m}$ and Gaussian $\lambda(z)$ with $\sigma_z = 96\,\mu\mathrm{m}$. The line charge density is assumed to be frozen with respect to the beamline coordinate s and its peak value corresponds to 500 A peak current. We see that when the bunch enters the bend (small s) the transient effects are comparable or even larger than the steady-state part. If the bend is long ($> 1\,\mathrm{m}$ in this case), the wake will be dominated by the steady-state part. For magnets $\approx 0.5\,\mathrm{m}$ long the transient effects are expected to be significant.

In [49] it was demonstrated that this model can be equivalently formulated in terms of instantaneous impedance

$$\frac{\partial Z_{\parallel b}(s,k)}{\partial s} = K(ik)^{1/3}\left[\Gamma\left(\frac{2}{3}\right) + \frac{1}{3}\Gamma\left(-\frac{1}{3}, ikz_L\right)\right] - \frac{Ke^{-4ikz_L}}{z_L^{1/3}}, \tag{2.154}$$

where $\Gamma(a) = \int_0^\infty t^{a-1}e^{-t}dt$ is the Euler gamma function and $\Gamma(a,z) = \int_z^\infty t^{a-1}e^{-t}dt$ is the incomplete gamma function. The model was extended in [44] to include the wakes obtained by the electron bunch after the bend in a subsequent drift section.

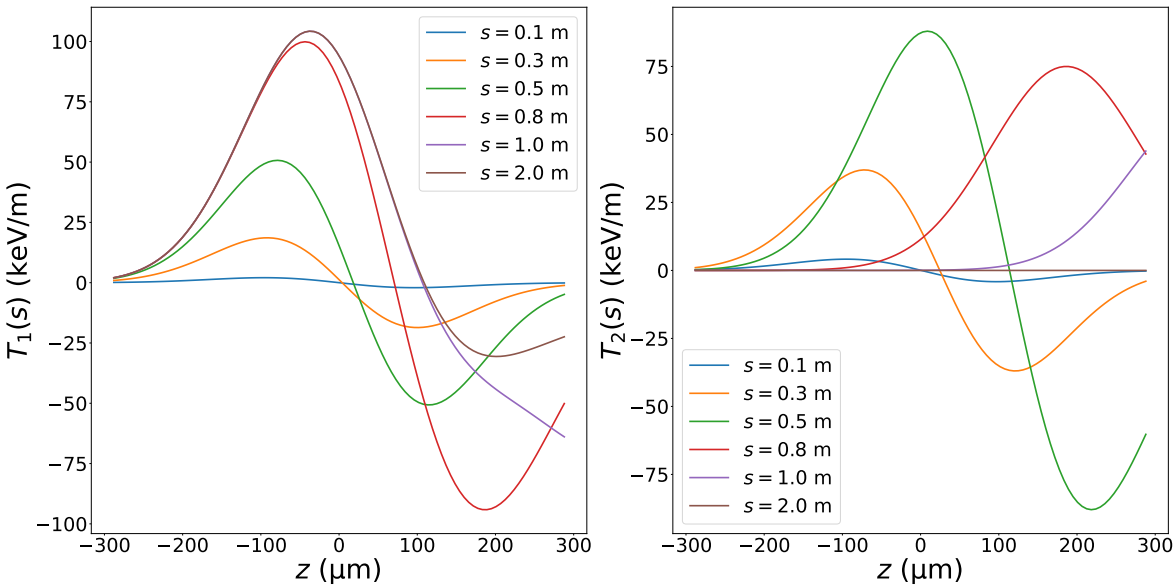

FIGURE 2.10: Contributions of steady-state (left) and transient (right) terms of Eq. 2.149. For the chosen parameters of the bend and the electron bunch the transient component is comparable to the steady-state component up to $\approx$ 0.5 m and decreases substantially after $\approx$ 1 m.

The wake is then given by

$$\frac{\partial W_{\parallel d}(s,z)}{\partial s} = T_3(s,z) + T_4(s,z)\,, \tag{2.155}$$

where T_3 and T_4 are given by

$$T_3(s,z) = -\frac{Z_0 c}{\pi}\frac{1}{l_b+2s}\lambda\left(z - \frac{l_b^2}{6R^2}(l_b+3s)\right)\,, \tag{2.156a}$$

$$T_4(s,z) = \frac{Z_0 c}{\pi}\left[\frac{\lambda(z-\Delta z_{max})}{l_b+2s} + \int_{z-\Delta z_{max}}^{z}\frac{1}{s'+2s}\frac{d\lambda(z')}{dz'}dz'\right]\,, \tag{2.156b}$$

$$\begin{aligned} s' = &-s + \frac{1}{2}\sqrt{4s^2 + Y^{1/3}(Y-16s^3)^{1/3}} \\ &+ \frac{1}{2}\sqrt{8s^2 - Y^{1/3}(Y-16s^3)^{1/3} + \frac{2Y-16s^3}{\sqrt{4s^2+Y^{1/3}(Y-16s^3)^{1/3}}}}\,, \end{aligned} \tag{2.157}$$

$Y = 24R^2(z-z')$ and

$$\Delta z_{max} = \frac{l_b^3}{24R^2}\frac{l_b+4s}{l_b+s}\,. \tag{2.158}$$

Unfortunately, Eq. 2.155 does not allow analytical formulation of corresponding impedance, as the calculation diverges [76].

CSR calculation with transient and chamber effects

Currently, no analytical model is offered that captures both the transient and the chamber effects. In this work the CSR impedance with transient and chamber effects is produced by `CSRZ` [49] numerical code. The code offers an alternative 1D model, based on calculation of the electromagnetic fields by solving Maxwell's equations in paraxial approximation. The resulting parabolic equations have the form:

$$\frac{\partial \vec{E}_\perp}{\partial s} = \frac{i}{2k}\left[\nabla_\perp^2 \vec{E}_\perp - \frac{1}{\epsilon_0}\nabla_\perp \rho_0 + \frac{2k^2 x}{R(s)}\vec{E}_\perp\right], \tag{2.159}$$

where $\vec{E}_\perp = (E_x(x,y,s;k), E_y(x,y,s;k))$ is the complex amplitude of the transverse electric fields and $R(s)$ is the s-dependent bending radius along the beam orbit. In the case of the chicane depicted in Fig. 2.4, $R^{-1}(s)$ is a step function equal to $\pm R^{-1}$ in a bend and 0 in a drift. The transverse charge density is denoted by ρ_0 and does not vary along s. The longitudinal component of the electric field can then be calculated as

$$E_s(x,y,s;k) = \frac{i}{k}\left(\nabla_\perp \cdot \vec{E}_\perp - \mu_0 c J_s\right), \tag{2.160}$$

where J_s is the current density, which gives the longitudinal instantaneous impedance as

$$\frac{\partial Z_\parallel(s,k)}{\partial s} = -\frac{1}{q}E_s(x_c, y_c, s; k), \tag{2.161}$$

where (x_c, y_c) denotes the center of the beam in the transverse plane. In practical calculations, the beamline is sliced into a certain number of sections. For each section, the impedance is lumped by integrating the instantaneous impedance as

$$\Delta Z_\parallel(k) = \int_{s_1}^{s_2} \frac{\partial Z_\parallel(s,k)}{\partial s} ds, \tag{2.162}$$

where (s_1, s_2) indicates the location of an impedance section along the beam orbit. $\Delta Z_\parallel(k)$ is then imported in `ELEGANT` tracking simulation using the `ZLONGIT` element located at s_2. The impedance is calculated step-wise for the whole chicane, allowing CSR to propagate into the drifts and subsequent dipoles.

Using sufficient slicing is important when the line charge distribution $\lambda(z)$ changes significantly inside the chicane. This is the case if the electron beam has a strong linear chirp, as illustrated in Fig. 2.11. In this work each dipole of the chicane is sliced in 4 sections. In order to verify that this slicing is sufficient for the nominal chirp value of -15 MeV/ps (or $h = 0.016$ if we follow the notation in [61]), we compare resulting CSR wakes at the exit of the chicane for slicing into different number of sections N: (i) the impedance is lumped to the exit of the chicane ($N = 1$); (ii) the chicane is sliced into $N = 4$ sections with impedance lumped to the end of the drifts; (iii) 4 dipoles are sliced in 4 sections + 4 drifts ($N = 20$). The total wake at the exit of the chicane can be then calculated as

$$\Delta W_\parallel(z_1) = \sum_{i=1}^{N} \Delta W_\parallel^{(i)}(z_1) = q\sum_{i=1}^{N}\int_{-\infty}^{\infty} \Delta Z_\parallel^{(i)}(k) \exp\left(-\frac{k^2 {\sigma_z^{(i)}}^2}{2}\right) e^{ikz_1} dk, \tag{2.163}$$

where $\sigma_z^{(i)}$ is the Gaussian width of the electron bunch at the entrance of section i. Comparing $N = 1$ to the sliced cases in Fig. 2.12 we see that the compression in the chicane changes the wakes significantly. At the same time, we see that slicing the

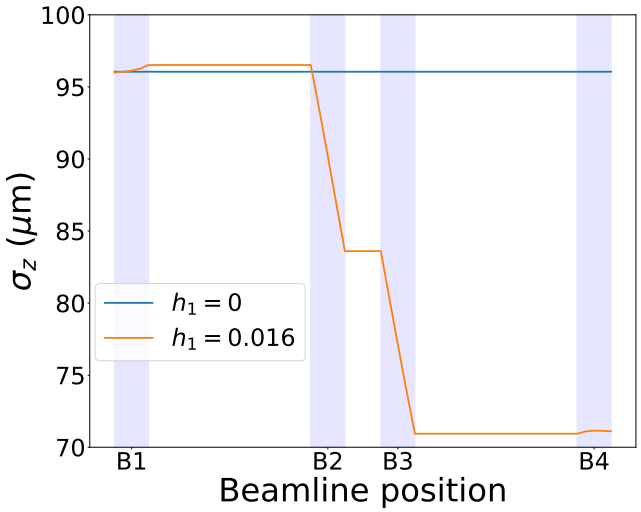

FIGURE 2.11: Evolution of the bunch length σ_z inside ch1 for nominal electron beam chirp ($h = 0.016$) and without the chirp ($h = 0$).

bends in 4 parts is more than enough to capture the effect.

The inter-dipole tracking of CSR can be to some extent formulated analytically to derive more general conclusion about its importance for specific cases. As demonstrated in [50], we can consider the inner wall of the chamber as a mirror for CSR emitted in one dipole and propagating to the next dipole after being reflected. In order to estimate if such trailing fields are expected to effect the bunch considerably, we consider the example illustrated in Fig. 2.13. Suppose, we have two consecutive dipoles separated by the distance $2L_d$. The dipoles have the same bending radius R, which is typical in a C-type chicane. The distance between the beam and the chamber wall x_h is assumed to be constant. In parallel plates model it would correspond to half-distance between the plates. Suppose, the radiation from the first dipole is reflected at the center of the drift space and catches up with the electron bunch in the next dipole. The path difference between the electrons and the photons is then

$$\Delta s_h = 2R(\tan\theta_h - \theta_h) + 2L_d\left(\frac{1}{\cos\theta_h} - 1\right), \tag{2.164}$$

where

$$\cos\theta_h = \frac{R(x_h + R) + L_d\sqrt{L_d^2 + 2Rx_h + x_h^2}}{(R + x_h)^2 + L_d^2}. \tag{2.165}$$

The angle θ_h should be comparable to half of the bending angle of the dipole. Otherwise, this scenario will not play out for most of the emitted radiation from point A. If this condition is satisfied, it makes sense to check if the path difference given by Eq. 2.164 is on the order of the bunch length σ_z. If $\Delta s_h \gg \sigma_z$ the bunch is not affected considerably by the trailing fields.

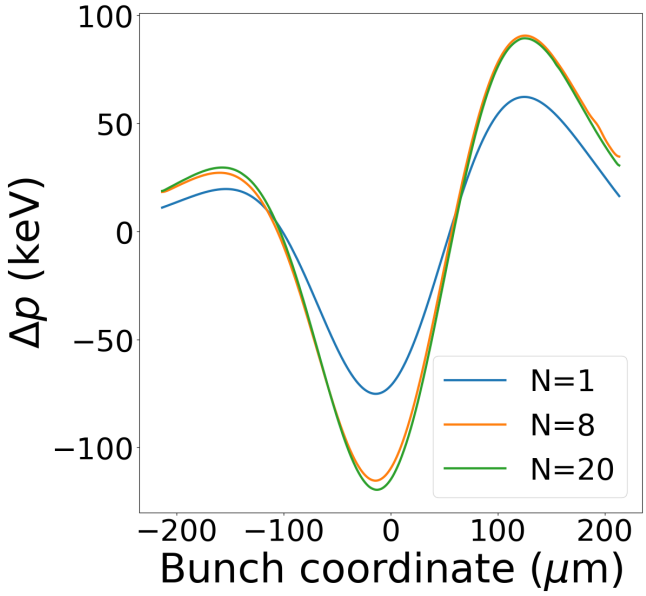

FIGURE 2.12: CSR wakes at the exit of ch1 for different slicing

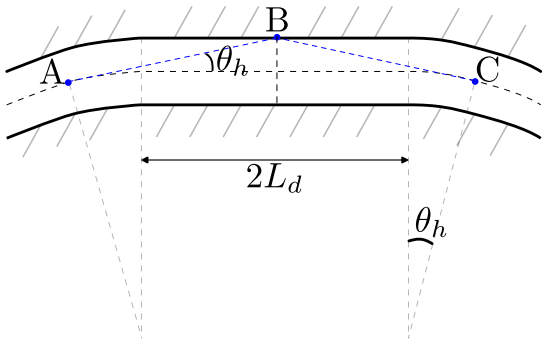

FIGURE 2.13: Geometrical representation of inter-dipole CSR interaction. CSR produced in the first dipole at point A is coupled back to the bunch at point C in the next dipole.

2.6 Mitigation of Microbunching Instability with Laser Heater

Microbunching instability (MBI) is energy and density modulations in the electron bunch typically in μm wavelength range. The mechanism of its development has a lot of similarities to the FEL techniques discussed in Subsec. 2.4.

The electron distribution at the beginning of the linac is not completely smooth and has initial inhomogeneities, which can be considered in the form of electron density modulations at various wavelengths λ_{in}. As in the discussion of SASE FEL, the initial density modulations are small and are essentially noise. These density modulations can be the source of CSR in bunch compressors, which would induce an energy modulation at the same wavelength in the bunch [77]. The modulations also produce space charge fields at λ_{in} as the electron bunch propagates through the beamline. By the time the electron bunch reaches the bunch compressor chicane, the space charge fields imprint energy modulations at λ_{in}. As the bunch propagates through the chicane, two things happen: (i) the bunch gets compressed, effectively reducing the wavelength of the modulations by the compression factor C; (ii) the energy modulations at λ_{in} are exposed to the longitudinal dispersion of the chicane and can generate density modulations, much like during the last stage of EEHG.

Combined those two effects increase the electron density modulations at λ_{in}/C after the chicane with respect to the initial distribution. This increase is called *microbunching gain*. If the energy modulations upstream of the bunch compressor are described with the integrated impedance $Z(k)$, the gain in the bunch compressor can be estimated as [15]:

$$G = Ck\,|R_{56}|\,\frac{I_0}{\gamma I_A}\,\frac{|Z(k)|}{Z_0}\exp\left(-\frac{1}{2}C^2k^2R_{56}^2\frac{\sigma_E^2}{E_0^2}\right), \tag{2.166}$$

where R_{56} is the longitudinal dispersion of the bunch compressor. The impedance of CSR contribution to the impedance was discussed in detail above. Since CSR takes place inside the chicane, one also should use the corresponding fraction of R_{56} in Eq. 2.166, as we did in Subsec. 2.5.1. However, it was shown [14] that the contribution of LSC can be dominant. The LSC-induced impedance per unit length is given by [78]

$$Z_{\text{LSC}} = \frac{iZ_0}{\pi k r_b^2}\left[1 - \frac{kr_b}{\gamma}K_1\left(\frac{kr_b}{\gamma}\right)\right], \tag{2.167}$$

where r_b is the beam radius and K_1 is the modified Bessel function of the second kind. If the transverse cross section of the beam is not round, r_b can be approximated as $\sqrt{\sigma_x^2 + \sigma_y^2}$. At high energies Z_{LSC} scales as $\sim \gamma^{-2}$. If there are several compression stages in the beamline, the process is repeated for density modulations at λ_{in}/C. Roughly speaking, the gain at λ_{in}/C is considerable if the relative displacement of the electrons due to the energy modulation at λ_{in} and the the longitudinal dispersion of the chicane is comparable to λ_{in}/C. This condition narrows down the wavelengths at which the microbunching can be considerably amplified for a specific machine layout and typically puts it in the µm range. One also has to keep in mind, that the uncorrelated energy spread of the electron bunch is exposed to the same longitudinal dispersion, which results in smearing of the longitudinal position of the electrons. An important conclusion here is that the microbunching gain can be suppressed by the uncorrelated energy spread upstream of the chicane.

MBI causes increased slice energy spread [79], which is of utmost importance for FEL performance, as follows discussed in Subsec. 2.4.1. MBI is particularly harmful for externally seeded FELs [16, 80, 13], as it can harm such key features as narrow bandwidth and shot-to-shot stability. In order to mitigate the MBI gain in the linac a device called laser heater (LH) can be used [22]. The basic idea is to use a laser modulator to induce additional uncorrelated energy spread, which suppresses the MBI gain as shown in Eq. 2.166. Layout of such a device is shown in Fig. 2.14. First, the laser is incoupled in the beamline by the mirror inserted in dedicated LH chicane. The laser induces an energy modulation in the electron bunch inside the undulator. Two screens on both sides of the undulator are used to ensure transverse overlap between the laser beam and the electron beam. After the undulator, the energy-modulated electron beam goes through the bunch compressor chicane. The energy modulation experiences the large longitudinal dispersion inside the chicane. This causes smearing of the modulation and effective increase of uncorrelated energy spread. The laser pulse is decoupled from the beamline by the mirror in the middle of the chicane and can be used for laser diagnostics. The OTR screen in the middle of BC1 can be used for electron beam diagnostics.

In this work the OTR screen is used to quantify the induced energy spread by the laser heater. The idea behind such a measurement is illustrated in Fig. 2.15. Particles with energies $p - \sigma_E$ and $p + \sigma_E$ acquire different bending angles ϑ_1 and ϑ_2 while

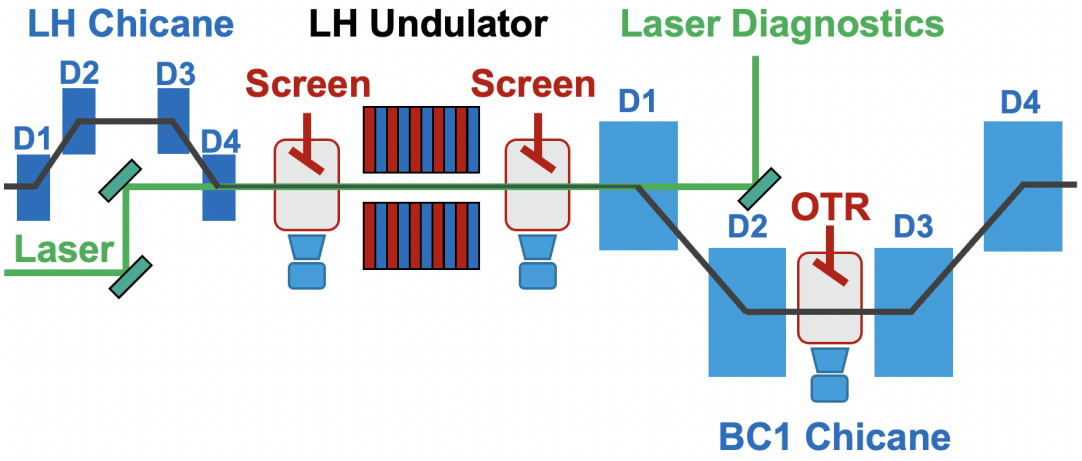

FIGURE 2.14: Schematic layout of the LH section at FLASH. Electron beam direction from left to right. Not to scale.

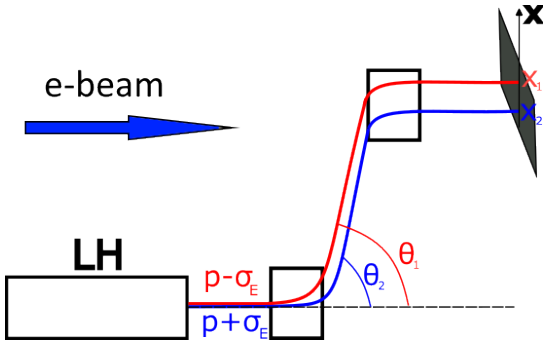

FIGURE 2.15: An illustration of LH-induced energy spread measurement with OTR screen in BC1. The energy spread σ_E is converted to beamsize σ_x.

traveling through the first dipole of BC1. The second dipole of BC1 puts the particles on parallel trajectories. The offset in x, acquired in the drift between the dipoles, can be easily calculated from the geometry of the chicane. This offset will contribute the the beam size measured at the OTR screen.

One can distinguish three regimes of the laser heater operation. The first regime is when the laser heater is off or set to low laser power. Then the microbunching-induced slice energy spread is large. With increasing laser heater laser power the energy spread of the electron beam induced by the laser hater is increased, while the microbunching-induced contribution is reduced. At some laser heater laser power we reach the second regime, when the slice energy spread is minimized. In this case the resulting slice energy spread, which is the sum of the intrinsic energy spread and contributions from the laser heater and the microbunching, is lower than the energy spread without the laser heater. We call this regime *optimal heating*. If we keep increasing the laser power even further, at certain point the laser heater contribution will become larger than the contribution of the microbunching. From this point on increasing the laser power will only increase the total slice energy spread. We call this regime *overheating*.

Chapter 3

Results

3.1 Ideal EEHG performance

The purpose of this section is to summarize results of EEHG simulations without the collective effects. This is done to define the parameter space, as well as to quantify and document the reference point for later discussion of the simulations with collective effects.

The most important parameters of the simulation set-up are given in Tab. 3.1. Both seed lasers are assumed to operate at the same wavelength of 300 nm, so $k_1 =$

Electron beam energy	1350 MeV
Initial rms energy spread	150 keV
Bunch length (Gaussian)	96 µm
Peak current	500 A
Seed lasers wavelength	300 nm
Target harmonic	75
Modulators length (periods)	30
$R_{56}^{(1)}$	7.05 mm
$R_{56}^{(2)}$	81.3 µm
A_1	3.10
A_2	5.18
z_R	3 m

TABLE 3.1: Nominal parameters of 4 nm EEHG working point

k_2. The target harmonic 75 is achieved by the combination of $n = -1$ and $m = 76$. The performance of the idealized set-up can be concisely characterized by the bunching spectrum, which is given in Fig. 3.1. The peak is very sharp due to relatively long bunch length of 96 µm. The position of the peak is defined by the phase term in Eq. 2.108 and is centered exactly at the target wavelength for the ideal set-up. During the optimization of the set-up we are effectively trying to match the maximum of the bunching envelope to this peak position. The envelope is given by Eq. 2.109 and shown in Fig. 3.1 with the dashed orange line.

Since no other working points are discussed in this work, from this moment we will denote $b_{-1,76}$ simply as b or bunching.

3.1.1 Electron beam chirp

The nominal electron beam chirp for the 4 nm EEHG working point is -15 MeV/ps, which is equivalent to $h_1 = 0.016$ using the definition in Eq. 2.118. The presence of the electron beam chirp changes the beam dynamics of EEHG starting from the very

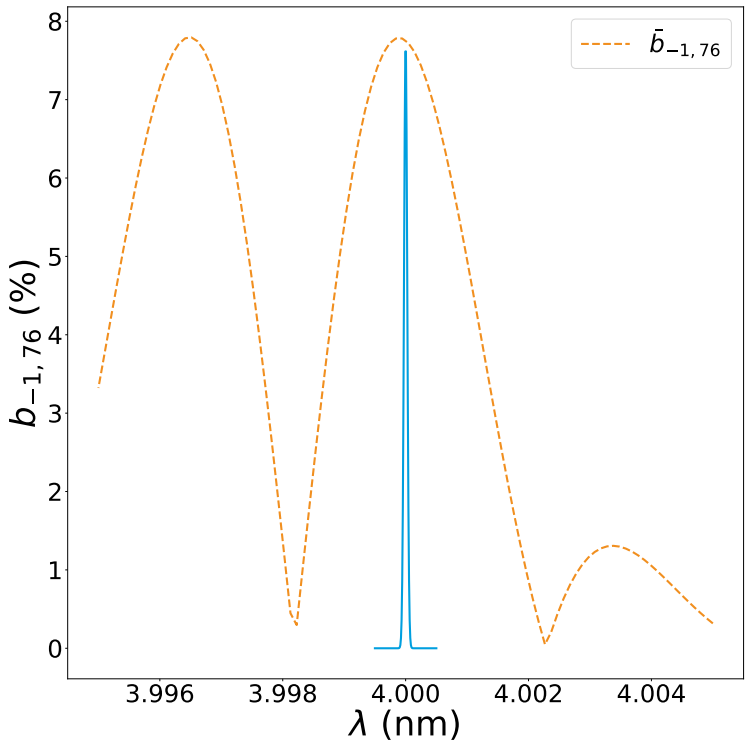

FIGURE 3.1: Bunching spectrum of an idealized EEHG setup give by Eq. 2.108. The dashed orange line indicates the bunching envelope given by Eq. 2.116. The amplitude of the bunching peak is mostly defined by the envelope, while the width is defined by the bunch length.

beginning of the seeding section, namely mod1. The effect of the electron beam chirp on the modulation amplitude can be calculated analytically using Eq. 2.77, 2.78. In Fig. 3.2 we compare the analytical formula with simulation results. We see that the simulation results are well-fit with the analytical formula. However, there are two comments we should make here. First, the number of periods of the modulator from the analytical fit is $N_u = 28.9$ instead of 30 given in Tab. 3.1. This can be explained by the fact that the outer poles of the modulator are set to lower peak magnetic field, than given by the resonant condition. This is done to compensate for transverse dispersion of the modulator. We can also see that the maximum modulation is not achieved at $z = 0$, where the electrons have exactly the resonant energy. This is likely due to the Gouy phase shift, mentioned in Subsec. 2.3.4. The results for mod2 are completely analogous. In the following we will detune the modulators' K_u in a way that the maximum modulation takes place at the center of the bunch, where we have the most electrons. Also, according to the discussion in Subsec. 2.4.2 we adjust the $R_{56}^{(2)}$ to have the same maximum bunching amplitude as in the non-chirped case.

In Fig. 3.3 we see that due to the linear chirp the bunching profile changes from flat to a bell-shaped curve. This is due to $A_1 = A_1(z)$ and $A_2 = A_2(z_1)$ in Eq. 2.112. For a strongly chirped beam and sufficiently narrow-band (long) modulators both functions change significantly along the bunch. The bunching envelope given by Eq. 2.109 becomes a function of z, as we see in Fig. 3.3. The width of the bunching profile in Fig. 3.3 is defined by the width of $J_m(-a_E A_2(z) B_2)$. The bunching in the center of the bunch, however, is the same as in non-chirped case, provided the slight adjustments to the modulators and ch2 mentioned above. We also note the increase

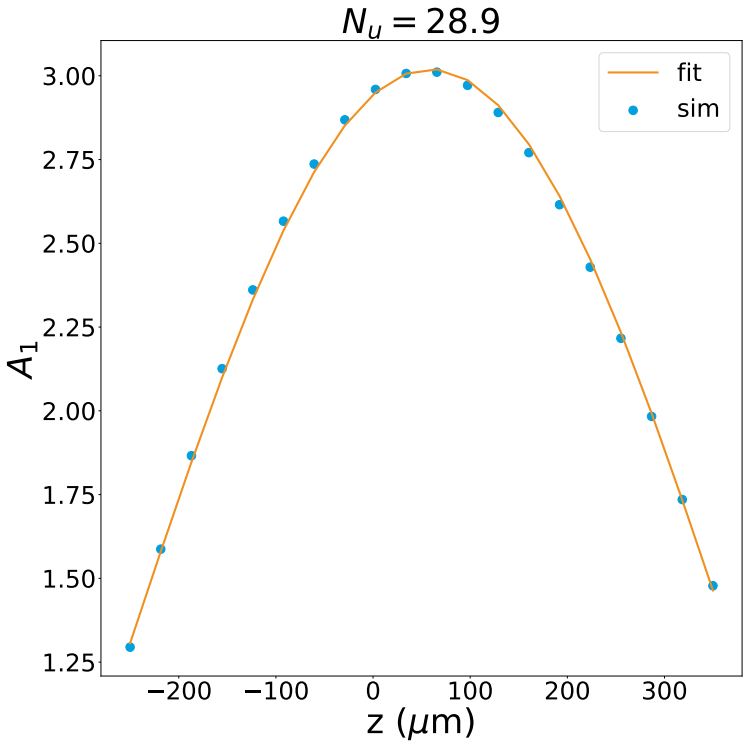

FIGURE 3.2: Modulation amplitude along the bunch with the nominal electron beam energy chirp. The fit is done using Eq. 2.77 with $\sigma_t = \infty$ and N_u as a free parameter.

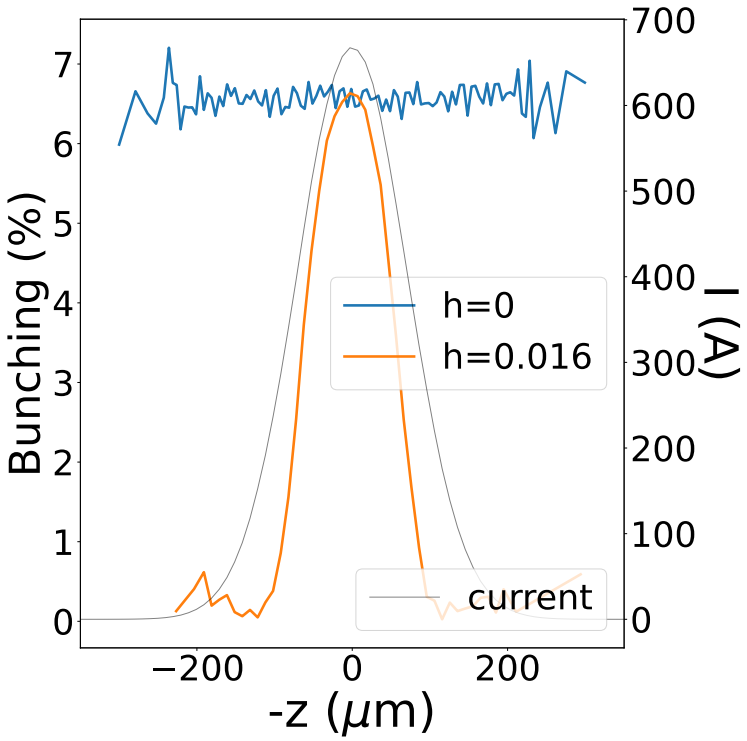

FIGURE 3.3: Bunching profile for different values of linear chirp. The bunch current profile for the chirped case is given in black.

in the peak current due to compression of the chirped beam in ch1.

The effect of the electron beam chirp on the bunching spectrum is illustrated in

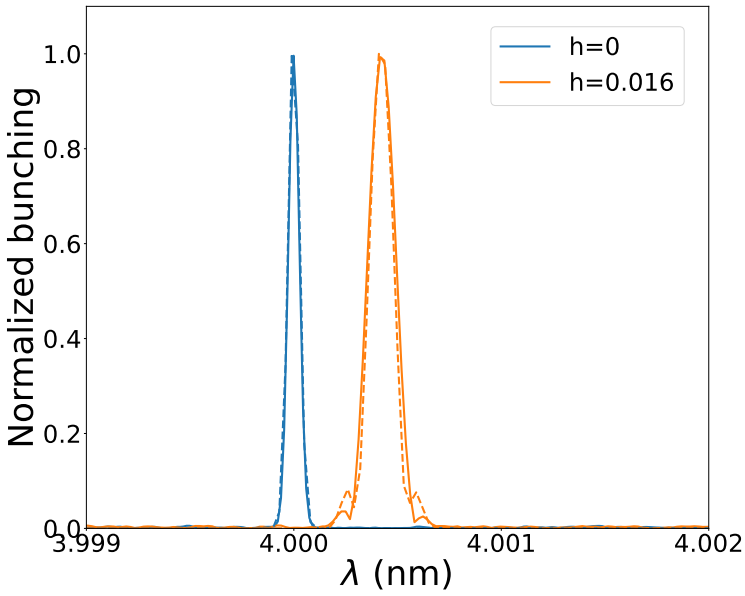

FIGURE 3.4: Analytical (dashed lines) and numerical (solid lines) bunching spectra for chirped and non-chirped beams.

Fig. 3.4. For a non-chirped beam the numerical bunching spectrum is in perfect agreement with Eq. 2.108. For the chirped beam the agreement with Eq. 2.115 is more modest, which we address to the fact that the formula is derived in the approximation $A_2(z_1) = A_2(z)$. This implies that the longitudinal profile of the bunch changes sufficiently slow, which is not exactly fulfilled, as shown in Fig. 2.11. However, we observe the broadening and the wavelength shift as was discussed in Subsec 2.4.2. The side-bands in the chirped beam spectrum can be addressed to sum- and difference-frequency generation, where the interfering frequency signal describes the bunching envelope from Fig. 3.3.

3.1.2 Finite laser pulse

For easier analysis we assume that the seed laser in mod1 remains infinite. We believe it is a fair approximation, since the dependence of the bunching envelope on $A_1(z)$ is relatively low in our parameter space. The dependence of the RMS width of the bunching profile σ_b^{RMS} on the duration of the second seed laser σ_t (Gaussian) is illustrated in Fig. 3.5 and compared to analytically calculated RMS width of J_{76}. The theoretical values agree with the simulations very well. As expected, the dependence is linear with the slope $k = 0.32$. The theoretical number for the slope given by Eq. 2.126 is $k = 0.39$, which is in good agreement with the simulations.

In the absence of the energy modulations $\Delta p_{1,2}$ from Eq. 2.112 the spectral width is defined by the Fourier counterpart of σ_b^{RMS}. This is illustrated in Fig. 3.6, where the bandwidth of the bunching spectrum is inversely proportional to the seed duration and converges to a constant value in the limit of infinite seed duration. The bandwidth in the limit of the infinite seed is defined by the Fourier counterpart of the electron bunch length.

The combined effect of the electron beam chirp and the finite seed duration on the

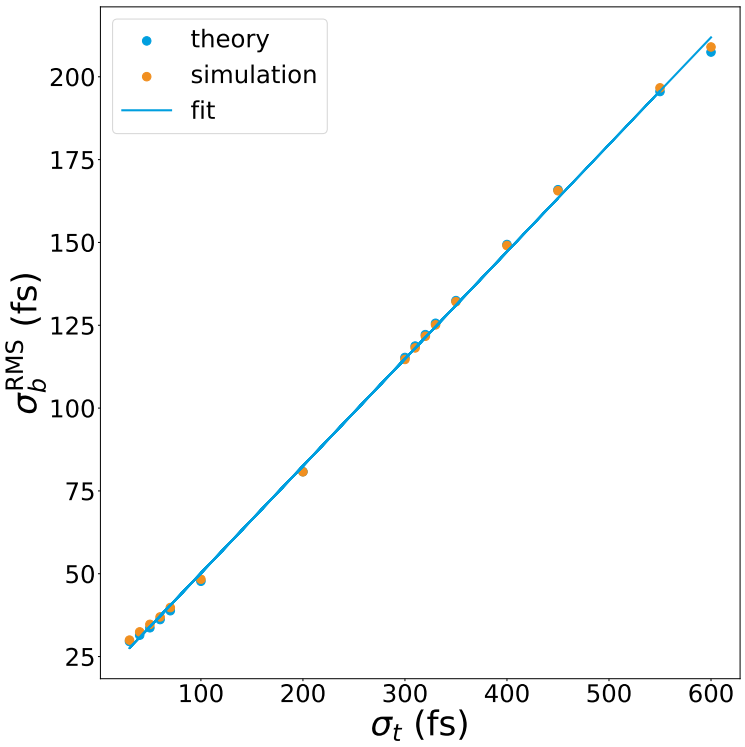

FIGURE 3.5: The width of the bunching profile as a function of the second seed duration. The theoretical linear dependence is well reproduced.

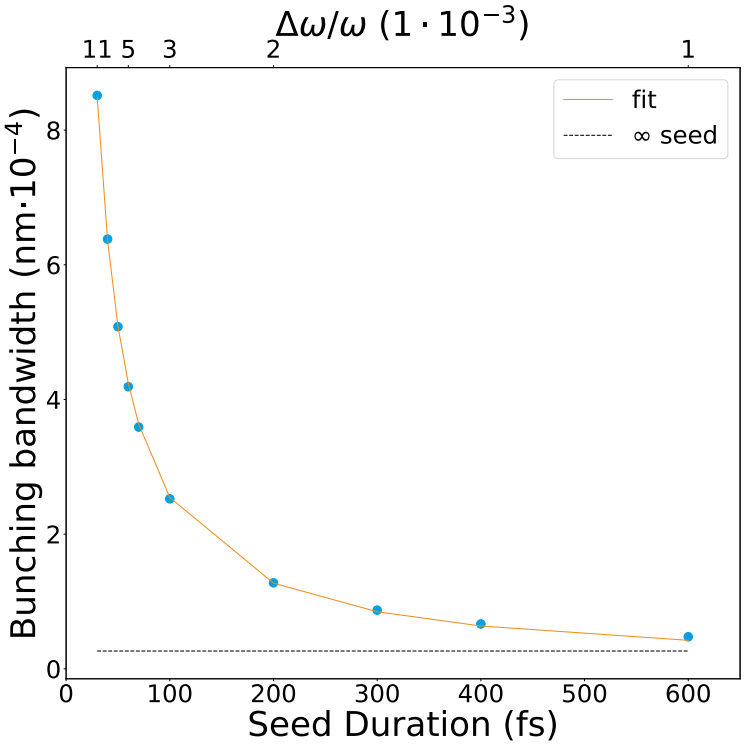

FIGURE 3.6: Spectral width of the bunching as a function of the duration of the seed. The fit illustrates the Fourier limit given by the effective length of the bunch.

width of the bunching profile is demonstrated in Fig. 3.7. The chirp is set to the nominal value $-15\,\mathrm{MeV/ps}$. The simulations agree well with the theoretical values. For longer seed duration the width of the bunching profile significantly deviates from the values given by the seed duration shown in Fig. 3.5.

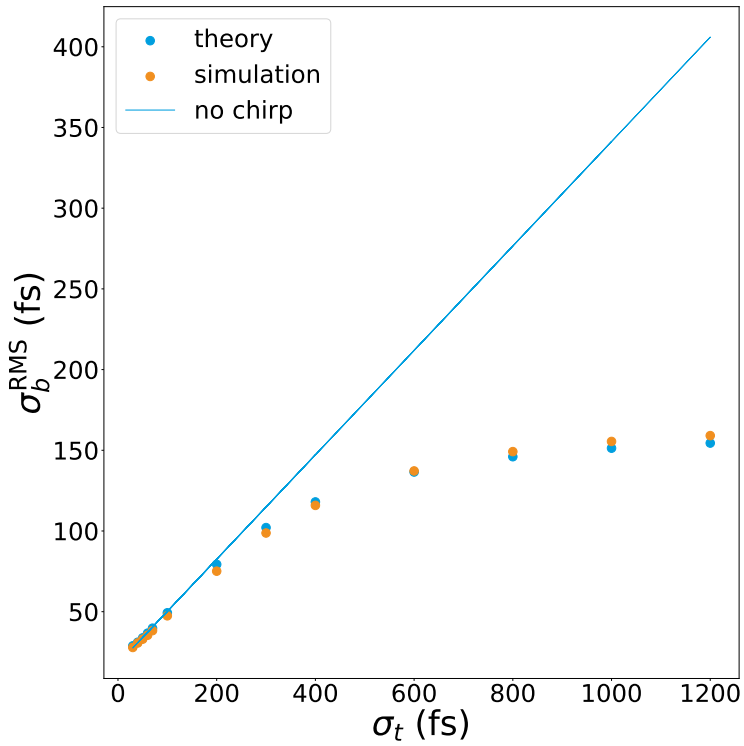

FIGURE 3.7: The width of the bunching profile as a function of the second seed duration for the nominally chirped electron beam. For long seed duration the deviation from the linear dependence from Fig. 3.5 is substantial.

3.2 Analytical calculations for ISR and IBS

In this section we summarize the results of investigation of the effects of ISR and IBS on EEHG harmonic conversion efficiency. As indicated in Sec. 2.5.1 - 2.5.2, we will see how these effects are scaled with geometrical and dispersive properties of the two chicanes in EEHG setup.

We start with calculating the distribution of the energy diffusion rate due to ISR and IBS. The results are given in Fig. 3.8. We assume that the energy diffusion due to ISR has a constant rate within each magnet. The energy diffusion in the two modulators is larger than that in the chicanes. However, since the longitudinal smearing is defined by the product of the energy diffusion and B_*, the bunching smearing from mod1 will be small. The energy diffusion due to IBS is mostly defined by the charge density. It is notably increased in ch1 due to compression of the electron bunch. Additional variations of the diffusion rate are due to the slight changes of the transverse size following the design electron beam optics in the seeding section (see App.C). We

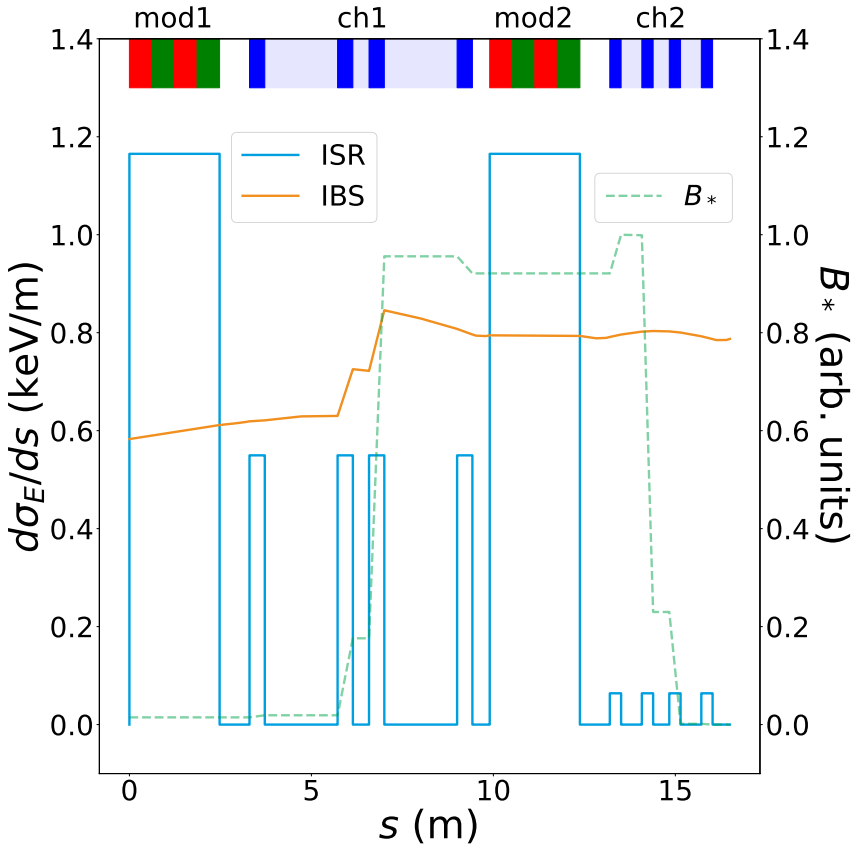

FIGURE 3.8: Distribution of the energy diffusion rate due to ISR and IBS and $B_*(s)$ from Eq. 2.129 along the seeding section. Diffusion due to ISR takes place in magnets. Diffusion due to IBS is enhanced by compression in ch1. B_* is large between ch1 and ch2.

can use Fig. 3.8 to estimate the induced energy spread and the bunching smearing due to ISR and IBS for each component of the nominal setup. The results are given in Tab. 3.2. We see that the effect of ISR is hardly notable everywhere except mod2, where we expect to lose about 5 % of the bunching amplitude. The effect of IBS is significantly more pronounced with the smallest contribution coming from mod1.

	ISR		IBS	
	σ_E^{ind} (keV)	$1-\eta_{\text{ISR}}$	σ_E^{ind} (keV)	$1-\eta_{\text{IBS}}$
mod1	2.9	$7\cdot10^{-4}$	1.5	$9\cdot10^{-4}$
ch1	0.7	$1\cdot10^{-3}$	4.1	9%
mod2	2.9	5%	1.7	7%
ch2	0.1	$2\cdot10^{-5}$	1.9	4%

TABLE 3.2: Contribution of individual components to the induced energy spread σ_E^{ind} and bunching smearing factor $\eta_{\text{ISR,IBS}}$.

Calculating the bunching smearing factor for the whole seeding section together, including drifts in between the components, we arrive to $\eta_{\text{ISR,IBS}} = 0.78$. This means that overall we expect to lose roughly 20 % of the bunching amplitude.

Let us now see if we can reduce these losses. Generally speaking, the choice of optimization parameters is fairly wide. However, we will restrict ourselves to those that are specific for the seeding section and do not influence the rest of the machine, including the seed lasers. This leaves us with optimizing the chicanes. Reducing the dispersion in the chicanes would reduce the overall B_*, which reduces the smearing. However, we have to keep in mind that the dispersion is essential for optimization of ideal EEHG setup, as explained in Subsec. 2.4.2. The other option is to change the lengths of the drifts and the dipoles of the chicanes, while keeping their R_{56} and overall lengths constant. On one hand, this could redistribute the dispersion along the seeding section and thus change the integral in Eq. 2.130 for both ISR and IBS. On the other hand, for ISR changing the dipole length can be a way to control the diffusion rate as well. Therefore, we could scan the R_{56} and the dipole length of the two chicanes to see if the effects of ISR and IBS could be mitigated.

Now we choose the range for the parameter scans. Since the R_{56} of the chicanes is of utmost importance for optimization of the idealized EEHG setup, we have to choose the range for the R_{56} of both chicane such that we stay within the bunching envelope given by Eq. 2.109. The bunching envelope for the chosen working point as a function of $R_{56}^{(1)}$ is given in Fig. 3.9. The points where the amplitude of the envelope drops to half of its maximum value can be used as an indication for the reasonable R_{56} range. From the figure we conclude that a reasonable range for $R_{56}^{(1)}$ is 6.40-7.21 mm. For the discussion of the chicane geometry we assume that the overall length of each chicane remains the same, while the lengths of the chicane dipoles and the drifts in between are changed. Here, it might happen, that we assume a dipole so short that its magnetic field has to unreasonably large in order to provide the same dispersion. The required magnetic field as a function of the dipole length of the first chicane is shown in Fig. 3.10. Assuming the magnetic field limit around 1 T, we conclude that the lower limit for the dipole length in the first chicane is 0.18 m. The higher limit is somewhat arbitrary and we choose it to be twice the nominal length. While scanning the dipole lengths it is convenient to make use of Eq. 2.132 and Eq. 2.143 instead of recalculating $B_*(s)$ every time. With this approach, however, we neglect C_1 in Eq. 2.129. The contribution of C_1 to the bunching smearing is expected to be small, but before neglecting it completely, we will quantify the dependence of the bunching smearing in ch1 due to IBS (the largest contribution) on $R_{56}^{(1)}$. The dependency is shown in Fig. 3.11. We see that the sensitivity of the effect to $R_{56}^{(1)}$ is very low. Changing the R_{56} in the chosen range only affects the 4th digit of η_{IBS}.

The same arguments for choosing the range can be applied to the second chicane.

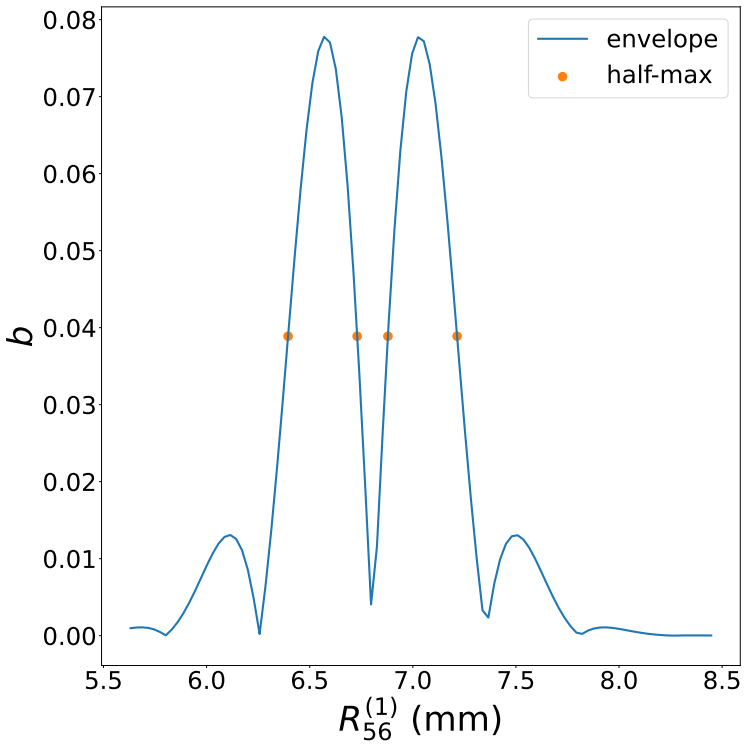

FIGURE 3.9: Bunching envelope as a function of $R_{56}^{(1)}$.

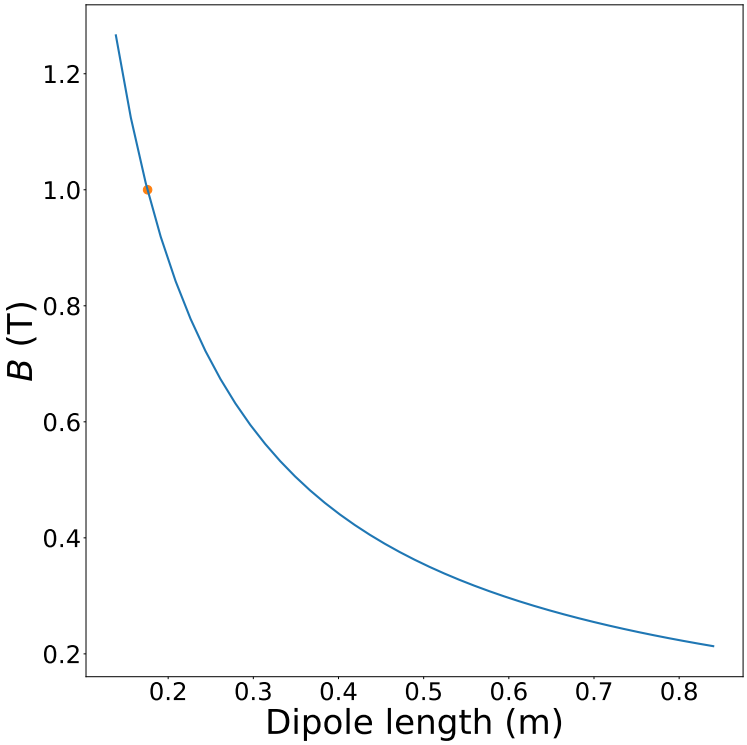

FIGURE 3.10: Magnetic field required for nominal dispersion as a function of dipole length in ch1.

The bunching envelope as a function of $R_{56}^{(2)}$ is given in Fig. 3.12. The same logic as for ch1 gives the range for $R_{56}^{(2)}$ of 88.66-92.74 µm. The required magnetic field as a

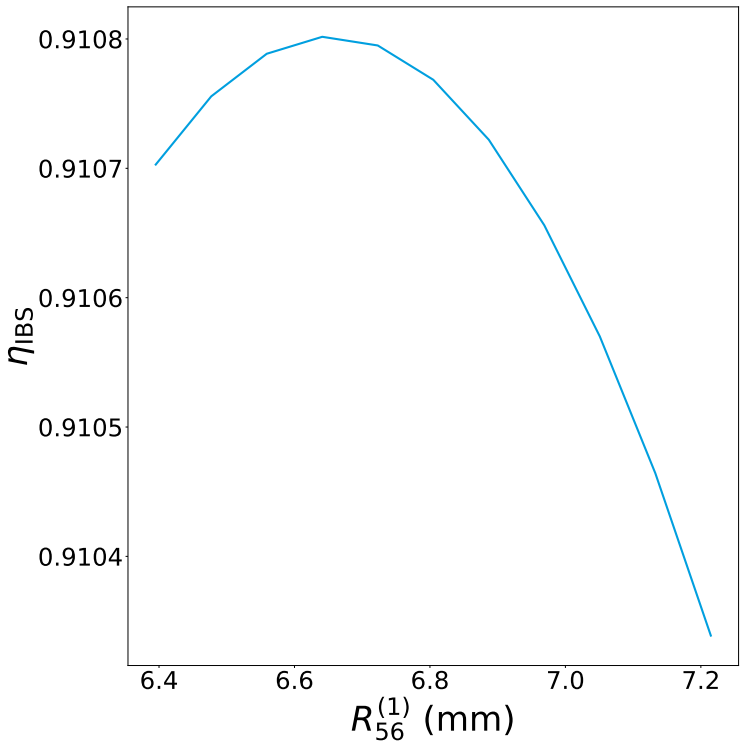

FIGURE 3.11: Scaling of the bunching smearing due to IBS in the first chicane with its R_{56}. The sensitivity is very low.

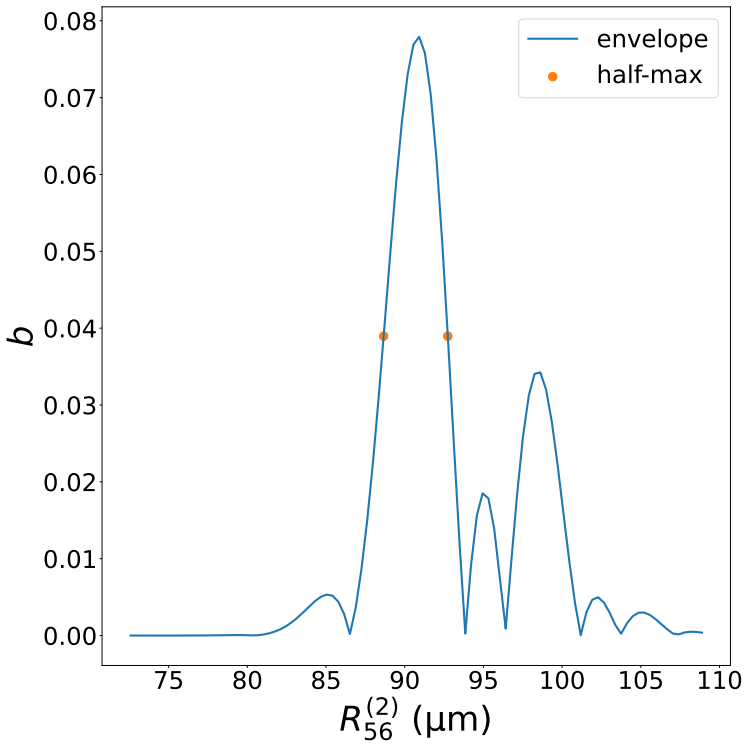

FIGURE 3.12: Bunching envelope as a function of $R_{56}^{(2)}$.

function of the dipole length of the second chicane is given in Fig. 3.13. Since ch2 has much less dispersion, it is not surprising that the lower limit for the dipole length

is quite arbitrary in this case. We choose the range from half to twice the nominal length for ch2.

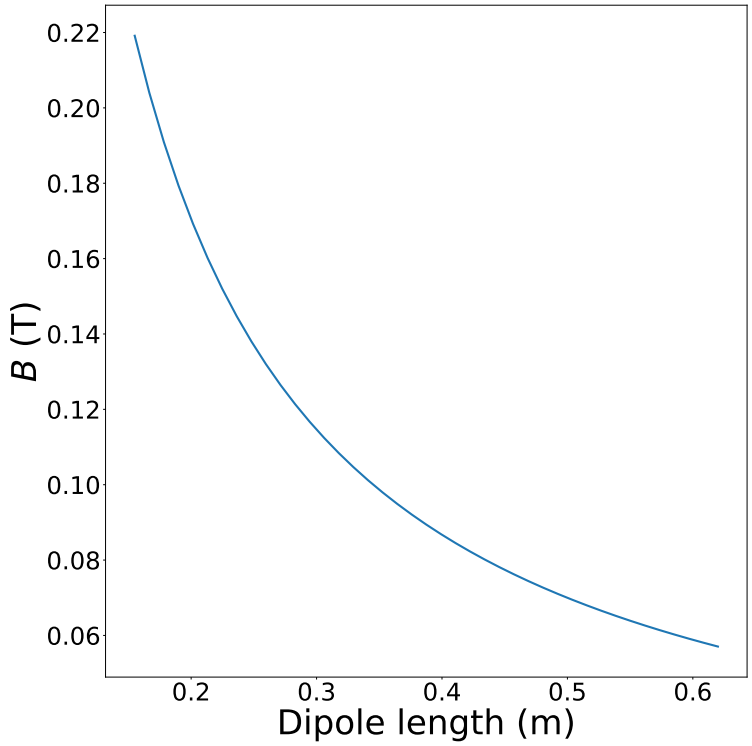

FIGURE 3.13: Magnetic field required for nominal dispersion as a function of dipole length in ch2.

3.2.1 ISR

The bunching reduction due to the ISR in the first chicane as a function of the dipole length for several values of $R_{56}^{(1)}$ is given in Fig. 3.14. We see that the effect is quite small in the whole parameter space. The effect is enhanced for shorter dipoles and larger dispersion. However, even for the shortest dipole length and the highest dispersion value we would lose less than 1 % of the bunching. For completeness, a similar plot for the second chicane is given in Fig. 3.15. We see that the effect is even smaller for ch2, which is expected given a much smaller bending angle compared to ch1.

3.2.2 IBS

For the discussion of IBS it is also convenient to make an additional simplification and neglect the compression of the electron bunch in ch1 due the the linear chirp from the linac. Before neglecting it, we estimate its importance for the bunching smearing factor η_{IBS}. Removing the effect of compression from the diffusion rate due to IBS given in Fig. 3.8 and recalculating the smearing factor of the whole seeding section we get $\eta_{\mathrm{IBS}} = 0.83$. This means that the bunch compression in ch1 enhances the effect of IBS by roughly 30 % compared to the case without the compression.

As discussed above, the effect of $R_{56}^{(1)}$ on the bunching smearing is neglected in dipole length scans. Fig. 3.16 shows how the bunching smearing in the first chicane scales with the dipole length only for the nominal $R_{56}^{(1)}$. The effect of redistributing

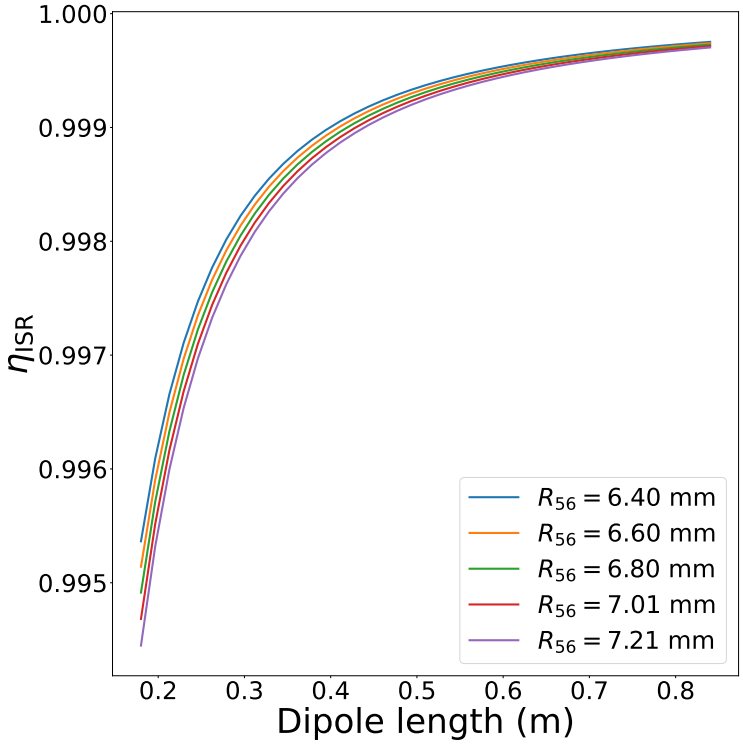

FIGURE 3.14: Bunching smearing due to ISR as a function of the dipole length of the first chicane.

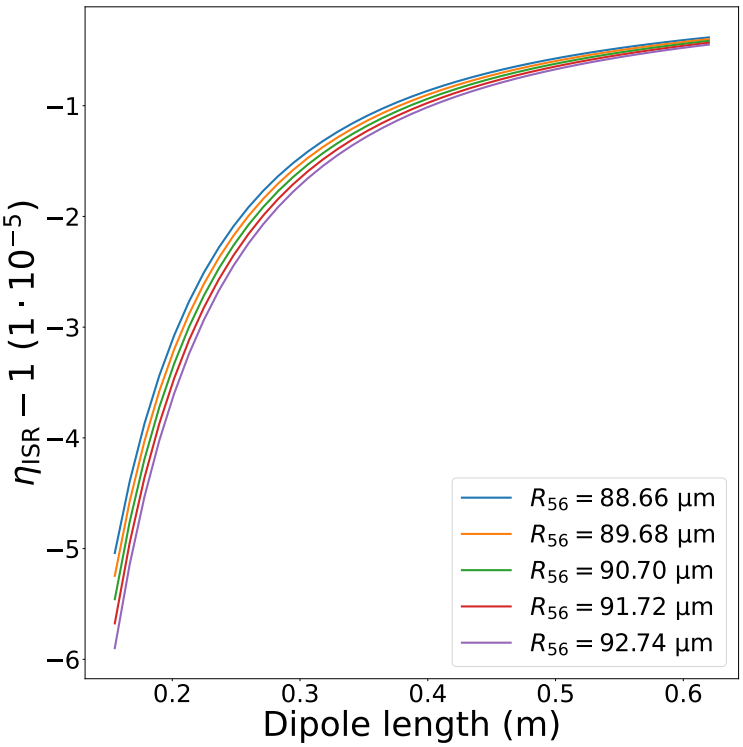

FIGURE 3.15: Bunching smearing due to ISR as a function of the dipole length of the second chicane.

the longitudinal dispersion along ch1 on the smearing is, unfortunately, very weak.

The scaling of the bunching smearing due to IBS in the second chicane is given

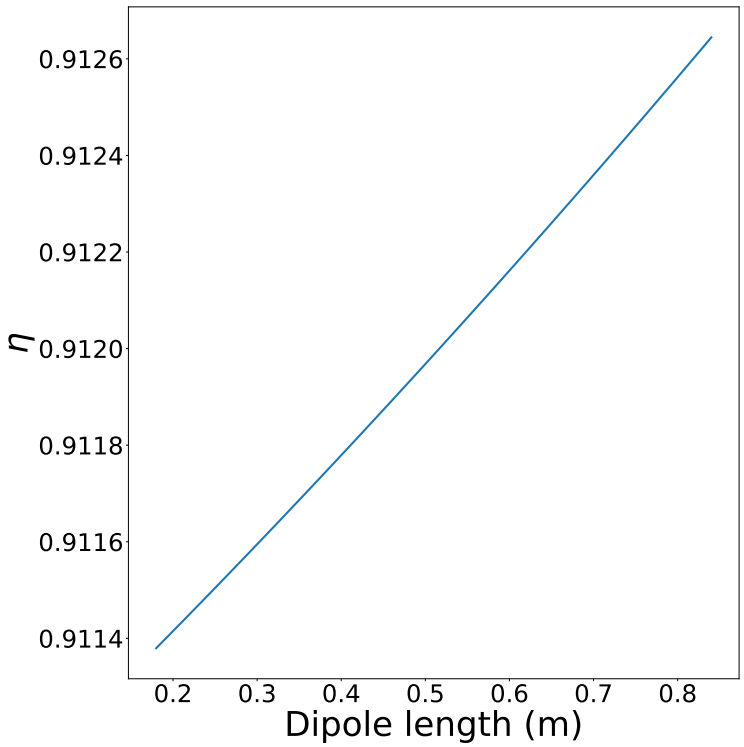

FIGURE 3.16: Scaling of the bunching smearing factor due to IBS in ch1 with its dipole length for nominal $R_{56}^{(1)}$.

in Fig. 3.17. We see that the smearing is quite insensitive to the dipole length. Its sensitivity to $R_{56}^{(2)}$ looks a bit more promising, but compared to that of the bunching envelope given by Eq. 2.109 is also negligible.

3.2.3 Summary of the section

As an intermediate summary, we conclude the both ISR and IBS are relatively insensitive to the parameters of the chicanes. This means that there is not much room for targeted minimization of their detrimental effect on EEHG bunching efficiency. On the other hand, their net effect is estimated to reduce the bunching amplitude by roughly 20 % for the nominal 4 nm EEHG working point. This reduction in the amplitude is unlikely to prevent an optimized EEHG set-up from producing well-above-noise initial density modulation for the amplifier.

3.3 Simulation results for CSR

The purpose of this section is to summarize results of simulations of CSR in EEHG lattice and its effect on EEHG performance. The results include calculation of CSR impedance in the first chicane using CSRZ code, as well as CSR-induced energy kicks throughout the chicane and EEHG bunching spectra obtained with particle tracking code `ELEGANT`. The simulation results are presented in the order of increasing complexity. First, we show the results for a simplified case of zero electron beam energy chirp. Later, we will lift this assumption and investigate its influence for our nominal parameters.

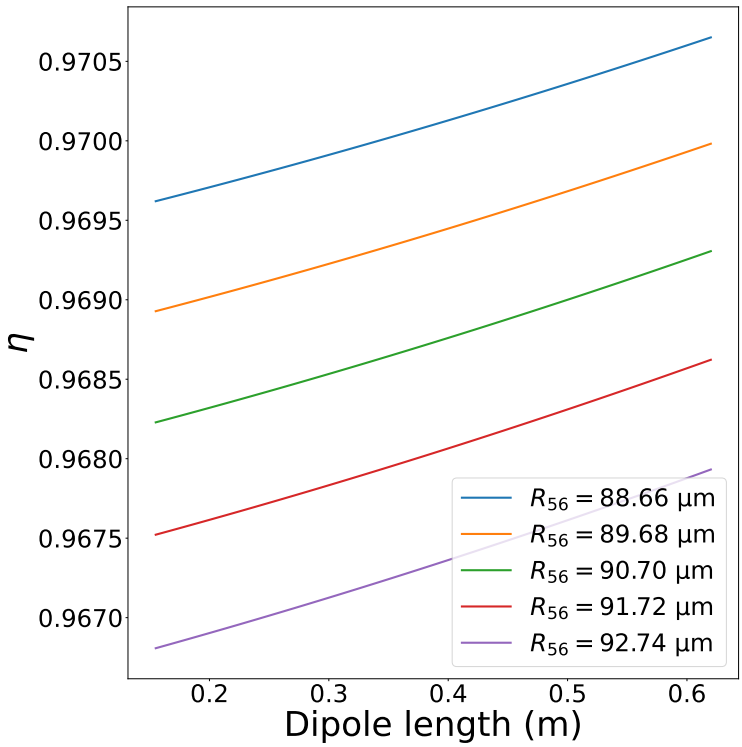

FIGURE 3.17: Scaling of the bunching smearing factor due to IBS in ch2 with its dipole length for different $R_{56}^{(2)}$.

3.3.1 CSR impedance and wake potential

We start by comparing CSR impedance given by different models. The purpose of this subsection is to highlight the importance of the two effects discussed in Subsec. 2.5.3 - transient effects and shielding - using the numerical example of EEHG chicane at FLASH. Since CSRZ model includes both effects, as well as inter-dipole radiative interaction, it is used as a benchmark.

Figure 3.18 shows CSR impedance of the first dipole of ch1. It is important to note that we assume no microbunching in the initial electron beam. Therefore, we can focus only on the part of the spectrum, which corresponds to macro-size of the bunch. The spectrum of the Gaussian bunch used in simulations is shown in Fig. 3.18 as dashed gray line. Within the bunch spectrum we see significant differences between PP and CSRZ models, which include shielding, and FS-SS model, which does not. Since the low-k components are significantly suppressed by shielding we expect a significant difference in energy kicks obtained by the bunch in the first dipole.

In Fig. 3.19 we compare the wake potentials calculated from the impedance shown in Fig. 3.18 for the initial bunch. First, we see that the amplitude of the wake given by FS-SS is indeed about 2 times larger than given by the other two models. Another fundamental difference between models with and without shielding is head-to-tail interaction. Without the boundary conditions given by the chicane chamber this type of interaction is not possible. For PP and CSRZ models the reflections of the radiation from the chamber walls enable positive energy kicks to the tail of the bunch (to the right in Fig. 3.19). By comparing results for FS-SS and PP models to CSRZ we can say that both shielding and transient effects are important for wake calculation in the first bend.

The role of shielding can be investigated in more detail by comparing wakes for

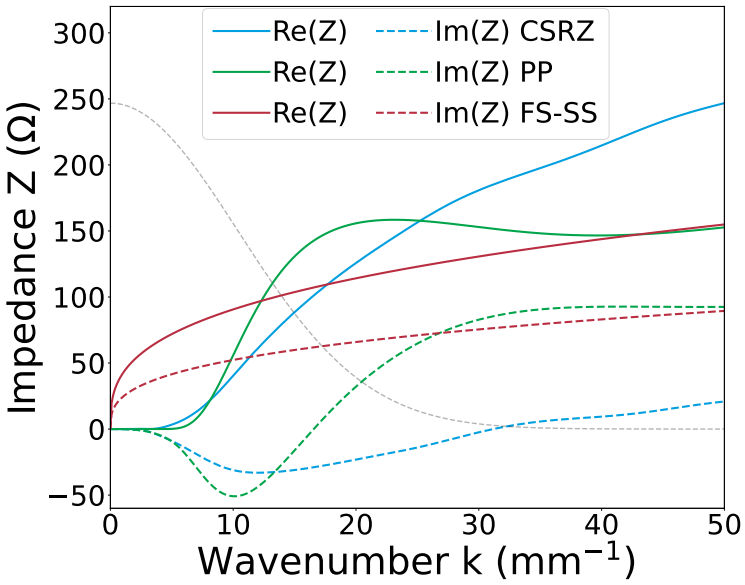

FIGURE 3.18: Total impedance of the first dipole of ch1. The dashed gray line is the spectrum of the initial bunch. Low k components are significantly suppressed by shielding (PP and CSRZ models) inside the bunch spectrum region.

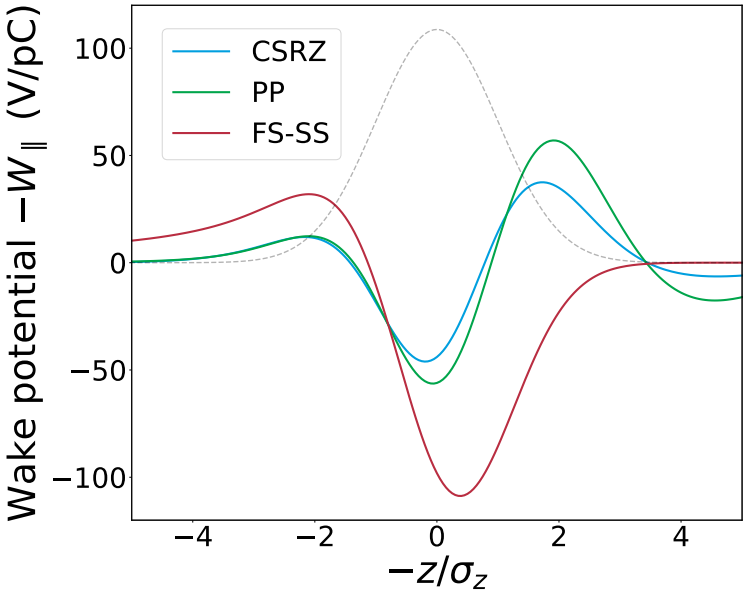

FIGURE 3.19: Total wake potential of the first dipole of ch1. The bunch head is to the left. The normalized current profile is given by the dashed gray line.

two transient models – CSRZ and FS-TR. Figure 3.20 shows the evolution of the wake through the first dipole for the two models. The dipole is sliced into 4 parts and the integrated wake is calculated for each quarter. Since both models include transient effects (in this case at the entrance of the bend) the difference between the two models can be solely attributed to shielding. In the first quarter of the dipole the reflection and re-coupling of the radiation does not have enough time to develop and the two models give very similar results. However, with increasing distance into

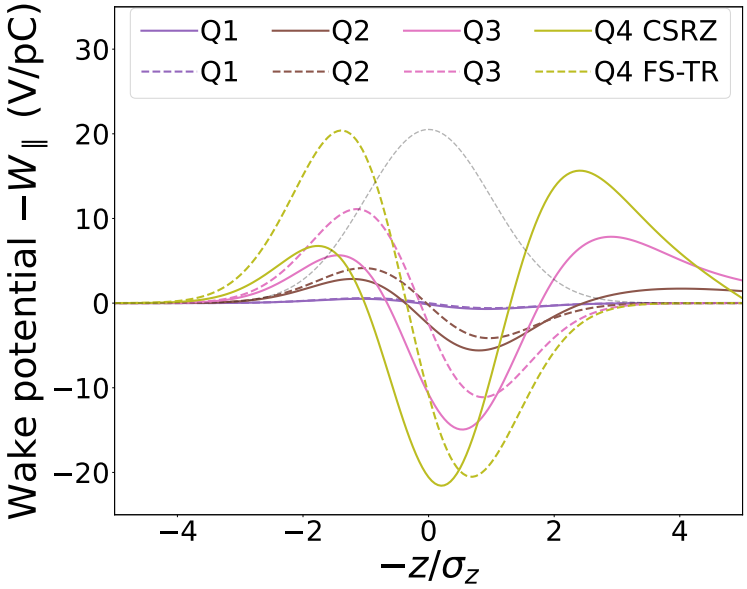

FIGURE 3.20: CSR wakefield of i-th quarter of the bend. The normalized current profile is given by the dashed gray line.

the dipole the effect plays an increasingly larger role and the shapes of the wakes get closer to those in Fig. 3.19. For both models we can also compare the wakes obtained

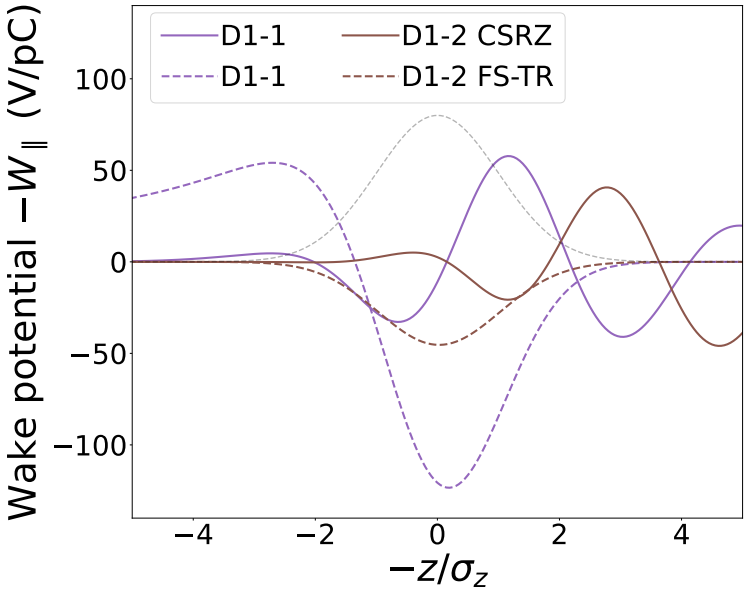

FIGURE 3.21: CSR wake in the drift after the first dipole. D1-1 and D1-2 indicate the first and second half of the drift. The normalized current profile is given by the dashed gray line.

in a drift following the dipole. In Fig. 3.21 we see a surprisingly large discrepancy in overtaking field between the two models in the first half of the drift, which is again attributed to the shielding effect. We can also see the difference in dynamics of the wakes for the two models in a drift. In FS-TR model the wake mainly decays in amplitude with distance from the dipole and also slightly changes in shape. When we compare D1-1 to D1-2 in CSRZ model we see that the second one is somewhat of a

delayed version of the first one with slight change in amplitude. This is an illustration of the radiation catching up with the electron bunch after multiple reflections. The reflections can also catch up with the bunch in the subsequent dipole. This sce-

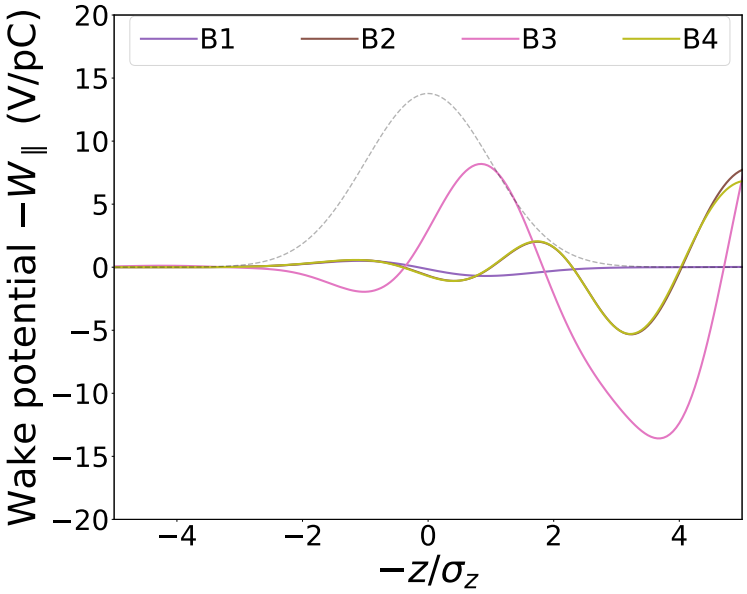

FIGURE 3.22: CSR wake in the first quarter of the i-th dipole of the chicane for CSRZ model. The normalized current profile is given by the dashed gray line.

nario is illustrated in Fig. 3.22. In the first quarter of the first dipole the overtaking field starts to develop and trailing field is absent. The wakes in the first quarter of B2 and B4 show trailing fields developed in B1 and B3 respectively and transported through identical drifts. These wakes are almost identical, as expected. In contrast, the wakes in the first quarter of B3 shows a much stronger trailing filed from B2. This is expected, since the drift between B2 and B3 is much shorter than the outer drifts. Recalling Eqs. 2.164-2.165 for B3 we estimate $\theta_h = 0.023\,\text{rad}$, which is fairly close to the half of the bending angle $\vartheta = 0.039$. The path difference Δs_h is about $3\sigma_z$, where we observe the largest amplitude of the trailing field in Fig. 3.22.

One also should keep in mind that the importance of the trailing fields depends not only on the chicane and chamber geometry, but also on the bunch length. Namely, if the bunch would be much shorter than in our example, the trailing fields would act only on a small portion of the particles in the tail of the bunch. An illustration for this statement for our chicane geometry is given in Fig. 3.23, where we show the wake in the first quarter of the 3rd dipole (B3) for different bunch lengths. From Fig. 3.23 we see that with decreasing length of the Gaussian bunch the amplitude of the wake drastically increases. This also applies to the trailing field, best represented for this estimation as the positive spike of the wake potential around 85 µm. In order to estimate how many particles are affected by this spike for each bunch length, we find z-positions of half-maximum points for the peak for each bunch length. Then we calculate the percentage of the particles between those points with respect to the whole bunch. With such estimation we conclude that for $\sigma_z = 96\,\mu\text{m}$ 39.3 % of the particles are affected by the spike, while 27.8 % are affected for $\sigma_z = 66\,\mu\text{m}$ and only 11.9 % are affected for $\sigma_z = 40\,\mu\text{m}$.

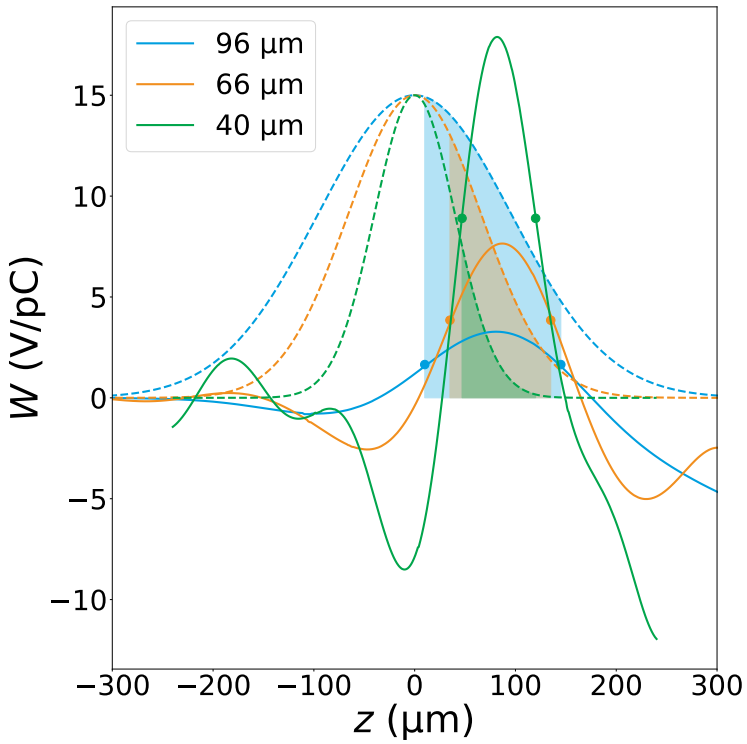

FIGURE 3.23: CSR wake in the first quarter of the 3rd dipole of the chicane for CSRZ model for σ_z=96 µm, 66 µm and 40 µm. The normalized current profiles are given by the dashed lines of the corresponding color. Half-maximum points for the peak at 85 µm are given as dots of the corresponding color.

3.3.2 Results of particle tracking simulations

Now that we illustrated the differences between different CSR models, we include CSR in ELEGANT simulations. The purpose of this subsection is to check the agreement between particle tracking simulations and analytical expressions given in Subsec. 2.5.3, quantify accumulated energy kicks at the exit of ch1 and estimate their effect on the bunching spectrum.

Infinite seeds, no electron beam chirp

We start with simplest case of infinite seed laser pulses and without the electron beam energy chirp.

The comparison of analytically calculated wakes and particle tracking results after the first dipole of ch1 is shown in Fig. 3.24. In the figure we see that the energy centroids from simulations are reasonably close to the analytical wakes and demonstrate some of the same features as Fig. 3.19. We note here that the time window is changed to $(-3\sigma_z, 3\sigma_z)$. This is done to avoid large numerical noise at the low-populated edges of the bunch to interfere with the analysis. We see that FS-SS model gives much larger energy kicks than the other two models. This can not be explained solely by the shielding, since FS-TR gives much more reasonable value for the kicks. This serves as another indication that both transient and shielding effects are important in our case. In the following we will not consider FS-SS model.

In Fig. 3.25 we see that FS-TR model gives much larger energy kicks at the exit of

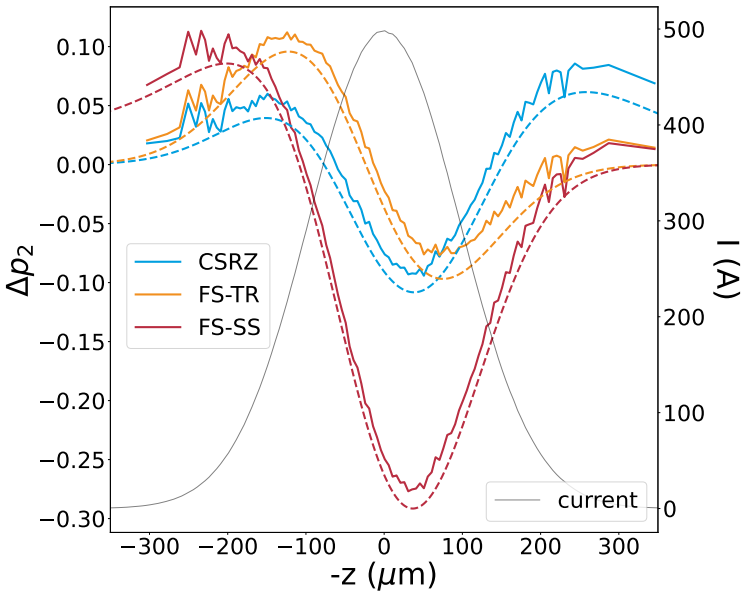

FIGURE 3.24: Energy centroid from particle tracking (solid lines) and theoretical CSR wakes (dashed lines) after the first bend for different CSR models. Bunch current profile is given in black. The bunch head is on the left.

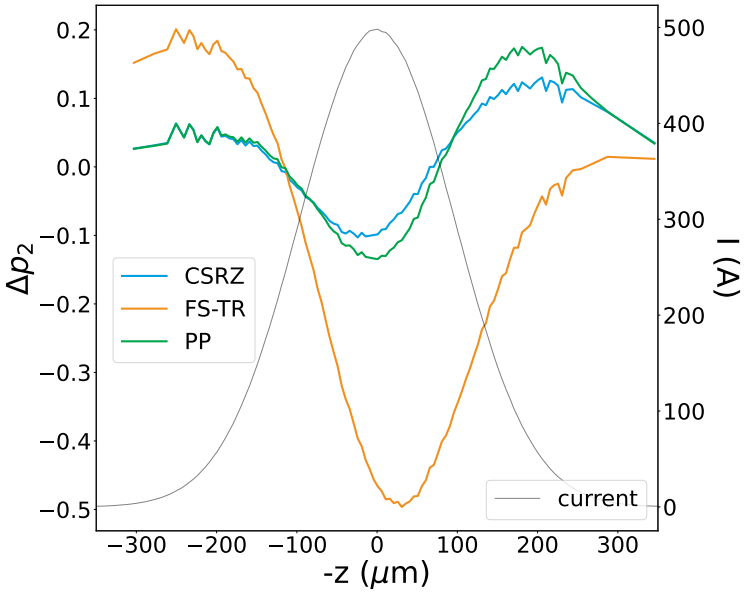

FIGURE 3.25: Energy centroid from particle tracking after the first drift for different CSR models. Bunch current profile is given in black. The bunch head is on the left.

the first drift compared to the other two models. This also confirms the conclusions made from Fig. 3.21. The kicks given by PP and CSRZ are reasonably close.

In Fig. 3.26 we see that at the exit of the chicane the CSRZ and PP models accumulate a notable difference in the trailing kick, while the overtaking kick is almost identical. There is also some difference in the amplitude of the kick around the center of the bunch, which is expected to provide most of the contribution.

In Fig. 3.27 we see that without CSR the shape of the spectrum is defined by the

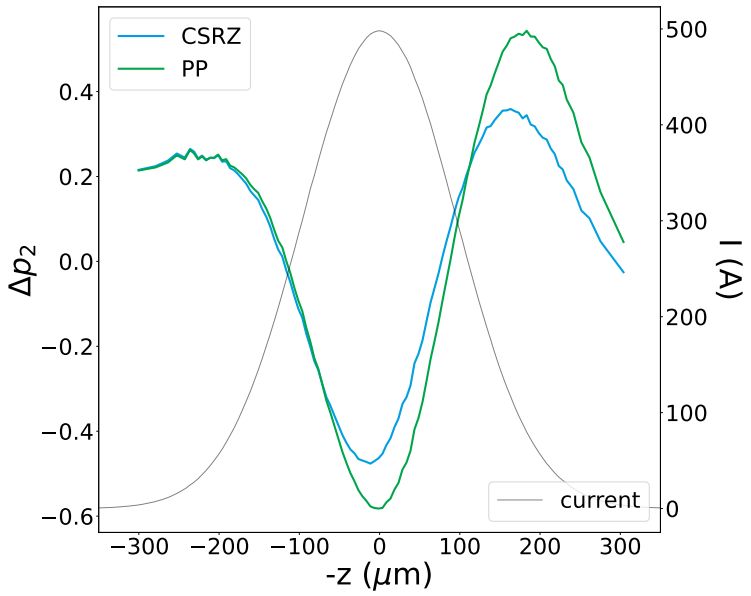

FIGURE 3.26: Energy centroid from particle tracking after the first drift for different CSR models. Bunch current profile is given in black. The bunch head is on the left.

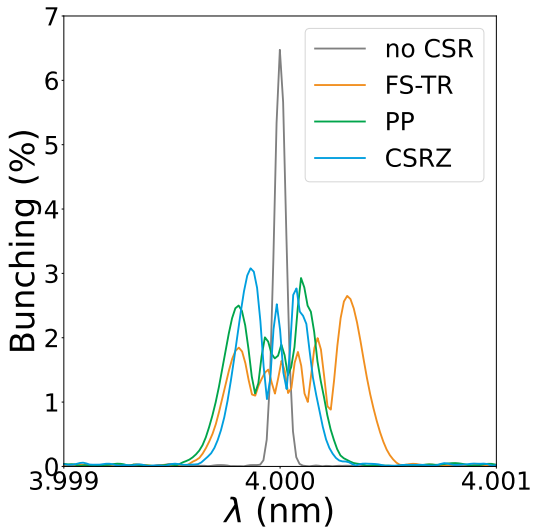

FIGURE 3.27: Bunching spectrum at the exit of ch2 for different CSR models.

shape of the electron bunch. With CSR the EEHG bunching spectrum obtains a complex structure and its bandwidth is effectively increased. Visually, we can say that FS-TR model gives the maximum bandwidth, which is consistent with the large value of the wake compared to other models. RMS spectral bandwidths for differ-

no CSR	FS-TR	PP	CSRZ
1.9×10^{-5} nm	2.2×10^{-4} nm	1.5×10^{-4} nm	1.2×10^{-4} nm

TABLE 3.3: RMS bunching bandwidth for different CSR models for a non-chirped electron beam

ent CSR models are given in Tab. 3.3. We can see that in general CSR increases the

bandwidth by an order of magnitude. We can also see that for FS-TR model the bandwidth is significantly larger than for the other two models, which correlates with the amplitudes of the wakes in Fig. 3.25.

We can also calculate the expected bandwidth from Eq. 2.125. As an example, we do such estimation for PP wake. The wake is shown in Fig. 3.28 in blue in the range

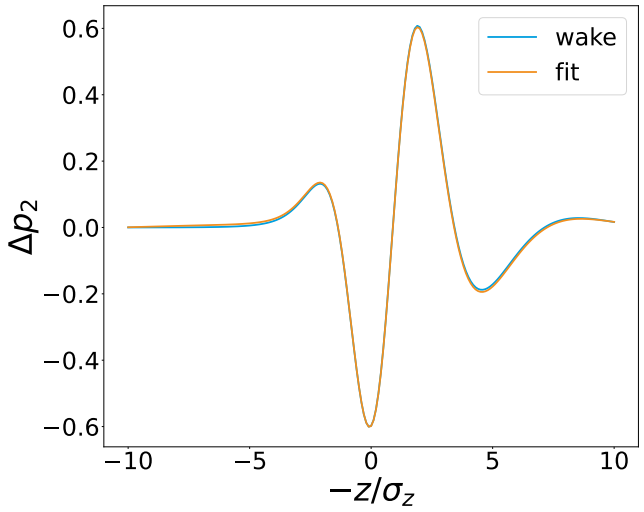

FIGURE 3.28: CSR-induced energy modulation at the exit of ch1 calculated with PP model and its decomposition in monochromatic components.

of $(-10\sigma_z; 10\sigma_z)$. Such large time window (compared to the figures in this section) is chosen in order to increase the resolution of the Fourier transform of the wake. The result of FFT is shown in Fig. 3.29. The spectral content of the wake is concentrated in $k_\mu < 5\,\mathrm{mm}^{-1}$. Using the amplitudes from Fig. 3.29 we can reconstruct the initial

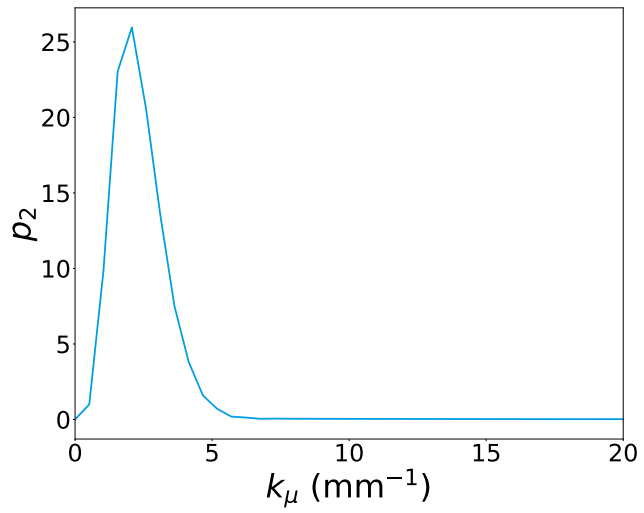

FIGURE 3.29: Fast Fourier transform of the CSR wake calculated with PP model

wake. The random phases φ_μ are used as free parameters for the fit. The results of the fit is shown in Fig. 3.28 in orange. We can see that the decomposition worked quite well, hence the extracted amplitudes are trustworthy. By using Eq. 2.125 we get an estimate for the induced bandwidth of about 1.1×10^{-4} nm. The agreement

between this value and the numerical value given in Tab. 3.3 is sufficiently good, considering that the spectral content of the wake does not really satisfy $k_\mu \gg 1/\sigma_z$, for which Eq. 2.125 was derived. Unfortunately, the accuracy of the formula does not allow to use it to compare different CSR models.

Qualitatively we can also explore another interpretation of the spectral broadening. By looking at Fig. 3.25 we can locally approximate the wake with varying linear chirp along the bunch. For example, FS-TR model gives relatively large positive chirp for the head half of the bunch. Combined with positive R_{56} of the second chicane this would lead to decompression of the bunch. In the bunching spectrum this would show as a red shift. This can be seen in Fig. 3.27 as the largest peak of the spectrum for FS-TR at a slightly larger wavelength. On the other hand, for CSRZ and PP models we see that considerably "chirped" parts are located more or less symmetrically around the center of the bunch and have opposite signs of the chirp. The shapes of the corresponding spectra in Fig. 3.27 also show somewhat symmetrical features around the central wavelength and are closer to it, compared to the largest peak of FS-TR. Therefore, we can theorize that the CSR-induced bandwidth is the result of varying linear chirp along the bunch, which makes different parts of the bunch contribute to bunching at slightly different wavelengths.

Infinite seeds, nominal electron beam chirp

The purpose of this subsection is to show how the effect of CSR changes due to electron beam chirp in the limit of infinite seed laser pulses.

In Fig. 3.30 we see that the effect of CSR on the chirped bunch is very similar to

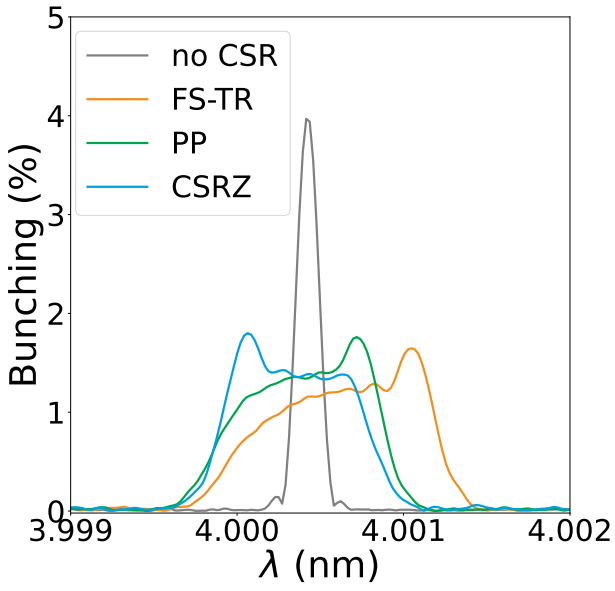

FIGURE 3.30: Bunching spectra for different CSR models with $h_1 = 0.016$ linear chirp.

the non-chirped case. The central wavelength is shifted by about 5×10^{-4} nm, as mentioned in Subsec. 2.4.2. The calculated RMS bandwidth for each case is given in Tab. 3.4. We can calculate the CSR-induced bandwidth and compare them for chirped and non-chirped cases. The induced bandwidth is larger in the chirped

case. This is expected, since the compression in ch1 increases the peak current in the bunch and, consequently, the CSR fields.

no CSR	FS	PP	CSRZ
4.4×10^{-5} nm	3.5×10^{-4} nm	2.8×10^{-4} nm	2.6×10^{-4} nm

TABLE 3.4: RMS bunching bandwidth for different CSR models for a chirped electron beam

3.4 Mitigation strategies

The purpose of this section is to illustrate the mitigation strategies for the effects of CSR and microbunching discussed above and their implementation at FLASH. The mitigation of the effect of ISR is not discussed here, because the effect is negligibly small. The mitigation of the IBS is also not discussed because of the practical constraints. For example, a good way to mitigate IBS would be to reduce the total length of the beamline or the nominal dispersion of the chicanes. Both are not very realistic.

3.4.1 Mitigation of the CSR effect

One of the established ways to mitigate the effect of CSR on the EEHG bunching efficiency is to use a short seed laser, limiting the seeded part of the bunch. The effect of the CSR wake is then reduced to its part, which is induced upon the seeded part of the bunch. The effective CSR-induced energy variation is then smaller than in the case of the infinitely long seed. As a result, the CSR-induced bandwidth is reduced.

In the presence of the CSR-induced energy modulation the total bandwidth is the square sum of the Fourier-limited bandwidth discussed above and the CSR-induced bandwidth according to Eq. 2.125. Since the relevant part of the CSR wake is defined by the seed duration, the CSR-induced bandwidth is also a function of the seed duration. In the limit of very short seed the total bandwidth is defined by the Fourier limit of the seeded part of the bunch. This is illustrated in Fig. 3.31, where the CSR wake is given by the FS-TR and CSRZ models. For seed duration less than 200 fs the effect of CSR is virtually absent. For seed duration longer than 200 fs the bandwidth of the bunching spectrum starts to deviate from the Fourier limit and the difference between the two models starts to show. In the limit of infinite (or very long) seed duration the bandwidth is one order of magnitude larger than the bandwidth given by the Fourier limit. In Fig. 3.31 we assumed no electron beam chirp.

Since we have already observed a substantial effect of the electron beam chirp on the CSR-induced bandwidth in Subsec. 3.3.2, we now show how the nominal chirp changes the results. In Fig. 3.32 we see that not only the bandwidth, but also the optimal seed duration strongly depends on the combination of the electron beam chirp and CSR. The contribution of the chirp itself to the bandwidth is rather small compared to the CSR contribution.

Since the optimization of the bandwidth depends on the electron beam chirp, we consider the complete range of chirp values anticipated at FLASH. The results are shown in Fig. 3.33 with a larger number of points around the minimal bandwidth. We see that the value of the optimal seed duration changes considerably in the given range of chirp values. The optimal values are summarized in Tab. 3.5.

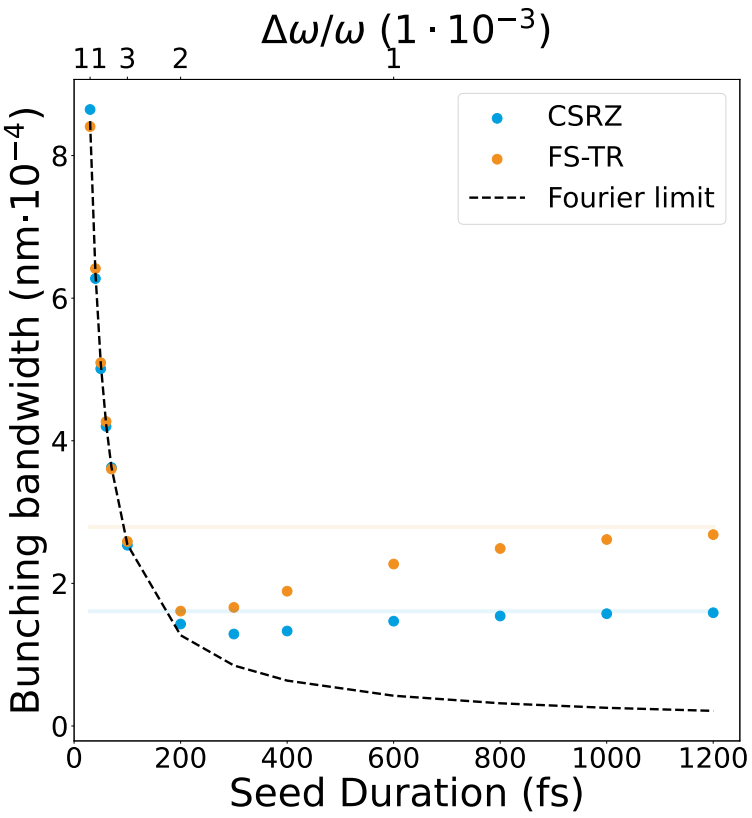

FIGURE 3.31: Spectral width of the bunching as a function of the duration of the seed for different CSR models without electron beam chirp. Horizontal lines show the limit of infinite seed duration. The bandwidth starts to deviate from the Fourier limit at $\approx$ 200 fs seed duration.

Electron beam chirp (MeV/ps)	0	8	15	20
Optimal seed duration (fs)	300	220	160	110

TABLE 3.5: Optimal seed duration, which gives the minimal bandwidth, for different values of electron beam chirp.

3.4.2 Experimental results of microbunching suppression

In this section we review results from Laser Heater commissioning at FLASH. The purpose of this section is to demonstrate LH capabilities in suppressing microbunching instability and eventually improving FEL performance.

Induced energy spread

The first thing we check is how much energy spread we manage to induce. For this purpose we insert an OTR screen in the middle of BC1, as shown in Fig. 2.14. The induced energy spread can then be derived as

$$\sigma_E^{ind} = D\sqrt{\sigma_x^2|_{P_L} - \sigma_x^2|_0}\,, \tag{3.1}$$

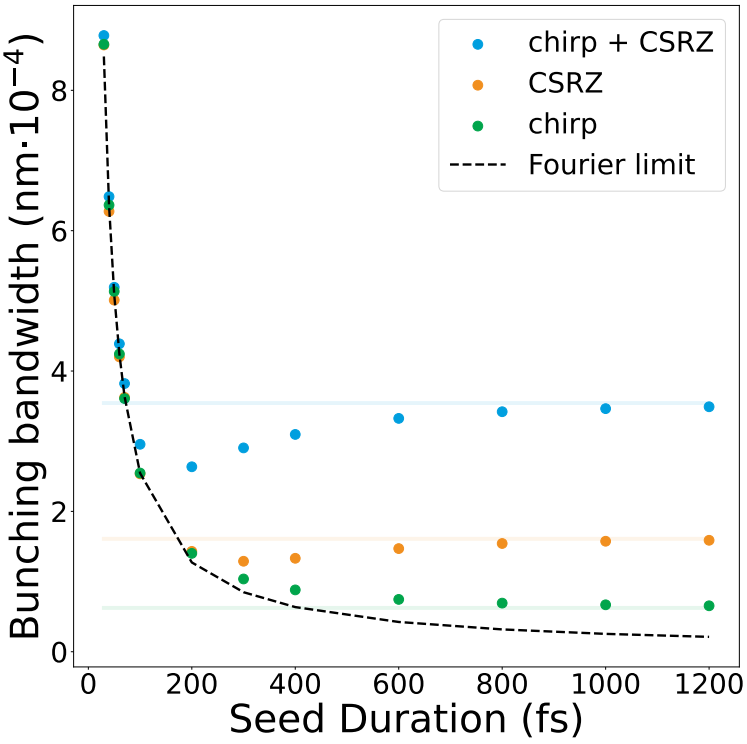

FIGURE 3.32: Spectral width of the bunching as a function of the duration of the seed for nominal electron beam chirp with CSR calculated with CSRZ model. Horizontal lines show the limit of infinite seed duration. The optimal seed duration depends on the combination of electron beam chirp and CSR.

where $\sigma_x|_{P_L}$ is the beam size measured with laser peak power P_L, and D is the inverse transverse dispersion, which we treat as an empirical constant. To find this constant we changed the central energy of the beam by changing the amplitude of ACC1. The resulting linear fit, shown in Fig. 3.34, gives $1/D = -685\,\mathrm{pix/MeV}$. As follows from Eq. 3.1, the resolution of the measurement is limited by $\sigma_x^2|_0$. The beam size at zero laser heater laser power consists of the natural beam size ($\sqrt{\beta_x \epsilon_x}$) and the effect of transverse dispersion on both (intrinsic) uncorrelated and correlated energy spread. To achieve the highest possible resolution we minimized the contribution of the natural beam size by minimizing β_x at the screen location with an upstream quadrupole. We also used specific settings of ACC1 and ACC39, which minimize projected energy spread.

Figure 3.35 shows the results of the measurement of the induced energy spread as a function of the laser heater laser peak power. From Fig. 3.35 we see that the measured data can be fit very well with the theoretical $\sigma_E \sim \sqrt{P_L}$ dependence. When compared to simulations, however, we measured almost 2 times less heating than expected. The possible reasons for this difference include non-perfect transverse overlap, non-optimal electron trajectory through the undulator and laser pulse transport losses. Despite that, the nominal value of induced energy spread of 10 keV is comfortably achieved at 2 MW with large overhead in available laser peak power. Therefore, we expect to be able to fully suppress microbunching, as predicted by

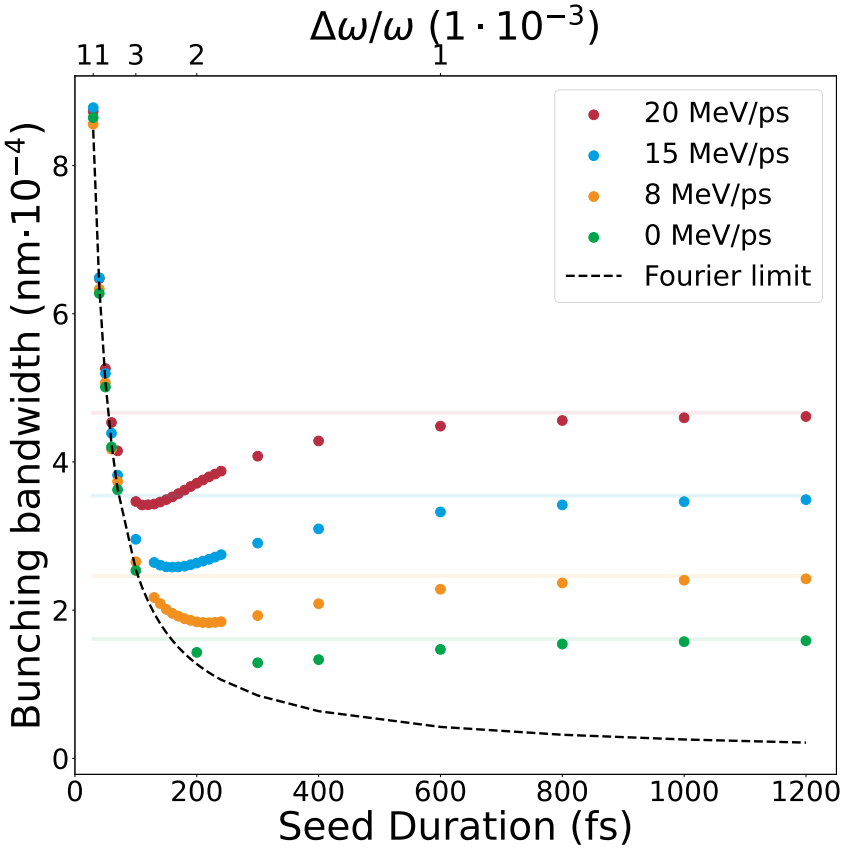

FIGURE 3.33: Spectral width of the bunching as a function of the duration of the seed for several values of electron beam chirp with CSR calculated with CSRZ model. Horizontal lines show the limit of infinite seed duration. The optimal seed duration depends on the electron beam chirp.

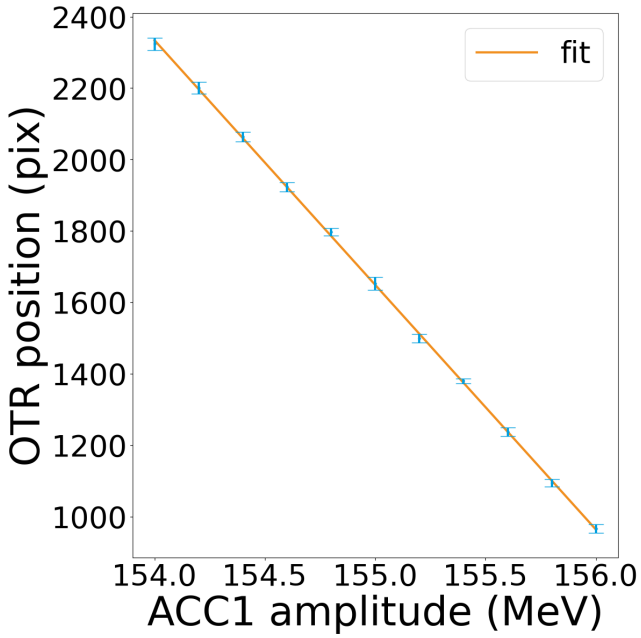

FIGURE 3.34: Energy calibration of the OTR screen in BC1.

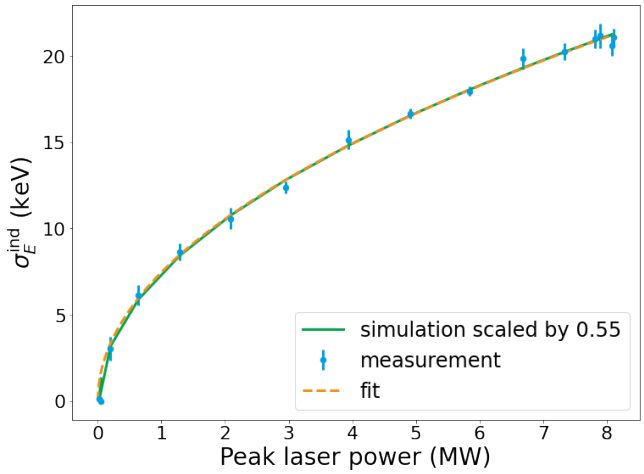

FIGURE 3.35: Laser heater induced energy spread as a function of the peak laser power. Measured values are well reproduced by `elegant` simulations but about 2 times smaller than the results of the simulation.

simulations [81].

MBI suppression

The microbunching suppression is confirmed by phase-space measurements done with S-band TDS LOLA, shown in Fig. 3.36. In Fig. 3.36 we can see that with laser heater laser off ($P = 0$ MW) there is well-pronounced microbunching in the beam. When the laser peak power is set to $P = 2$ MW the induced energy spread in the electron beam is ≈10 keV, as follows from Fig. 3.35. One can see that at this level of uncorrelated energy spread the microbunching is effectively suppressed. When the laser power is set to maximum $P = 8$ MW, the electron distribution is smeared and obtains double-horn structure.

Improvement of SASE FEL

Although the microbunching is fully suppressed with 10 keV induced energy spread, it doesn't necessarily mean that this is the optimal point to operate the LH. As was mentioned in Sec. 2.6, the optimal point for FEL performance results in from interplay between suppressed microbunching and induced energy spread. This is illustrated in Fig. 3.37. The figure shows integrated intensity of SASE signal in FLASH2 obtained by Gas Monitor Detector. In region 2 the laser heater is off, so this level of SASE intensity can be used as a reference. In region 3 the laser peak power was set to 1.3 MW, which is considerably lower than the nominal 2 MW. Nevertheless, the SASE intensity is much lower than in the reference case. The optimal SASE intensity is achieved in region 1, where the peak laser power was on the order of 0.1 MW. The optimal LH setting is specific to the operation mode and has to be found for each case. Nevertheless, Fig. 3.37 demonstrates that such setting can be found in FLASH configuration and it probably lies at low laser heater laser power region.

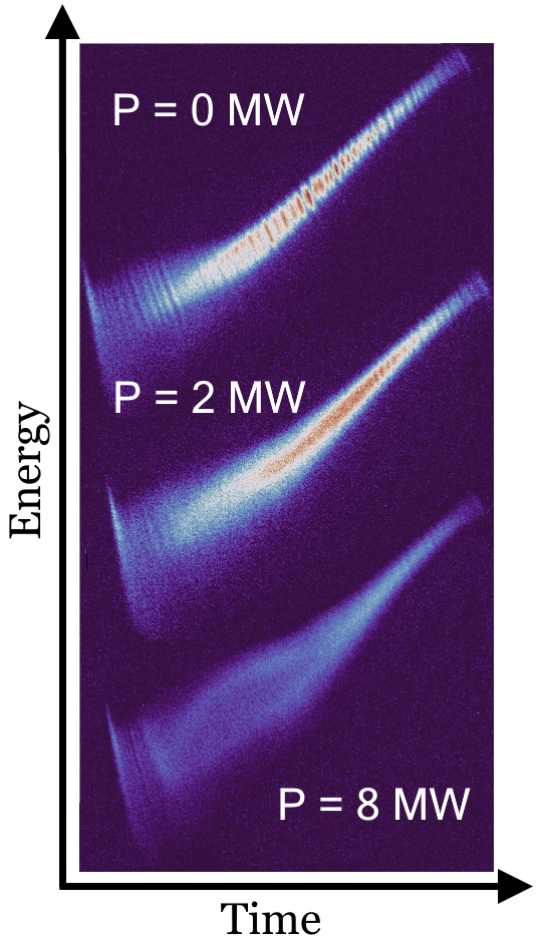

FIGURE 3.36: LOLA TDS images at different peak laser power. The microbunching is significantly reduced at moderate laser power. At high laser power the electron distribution is distorted and shows the 'double-horn' feature.

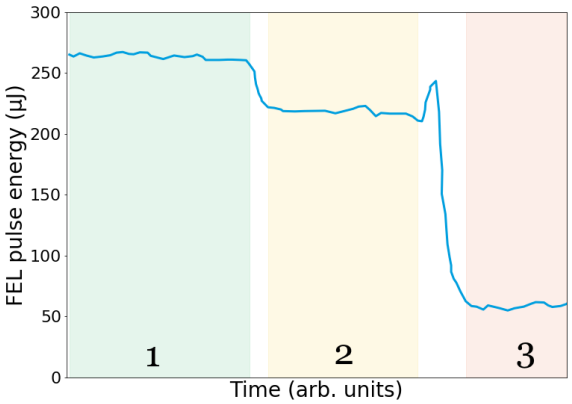

FIGURE 3.37: History plot of the FEL pulse energy illustrating the effect of the LH laser power on the FEL performance. 1. LH laser power optimised for maximum pulse energy, 2. LH laser blocked, 3. LH laser power set to 1.3 MW.

Chapter 4

Discussion

The purpose of this chapter is to provide additional perspective on the results presented in Chapter 3. This includes an analysis of the applicability of the results to a different parameter space, possible extensions of the treatment for FLASH2020+ and an outlook.

4.1 ISR and IBS

In Sec. 3.2 we have seen that the effect of ISR and IBS on the harmonic conversion efficiency basically can not be mitigated in the seeding section in an isolated way. At the same time, for the 4 nm EEHG setup at FLASH2020+ these effects do not present a significant design bottleneck, especially when compared to CSR. In the analysis of Subsec. 2.5.1 , 2.5.2 we see that this might change if significant changes occur in the machine parameters. For example, if the overall distance between the center of the first chicane and the center of the second chicane would significantly increase, this would benefit IBS. The effect of IBS is also quite notably enhanced by the bunch compression in ch1, which scales with the linear chirp of the electron beam and the R_{56} of the chicane, as described by Eq. 2.56. For the same reason, having a considerably larger nominal peak current might call for reconsidering IBS-induced smearing. As for ISR, the most crucial factor is the beam energy with the corresponding diffusion rate scaling roughly as $\sim \gamma^4$. Hence, for machines operating at larger energies ISR can also become a considerable problem. Finally, it is worth mentioning that for higher harmonics both effects will play a more significant role.

The study presented above can be extended to the machine sections other than the EEHG seeding section. The discussion of the bunching smearing would be less relevant in most sections, but the induced energy spread can still be important for any FEL process. For example, the energy spread induced in the linac (by IBS in particular) can work in a similar way as the laser heater [32]. The additional dynamically growing energy spread can be another complication in the radiator part of the machine, which is typically long (favoring IBS) and packed with magnets (favoring ISR).

4.2 CSR

The effect of CSR on EEHG FEL bandwidth was shown to be significant in the limit of long seed laser pulses ($\approx$ 200 fs and longer). With the nominal 50 fs seed2 pulse duration planned for FLASH2020+ the effect of CSR seems to be much less significant, as the Fourier limit becomes dominant. When the priority is producing short FEL pulses (for measurements requiring high temporal resolution), practical consideration of CSR may not be required. However, when spectral purity is prioritized

(for measurements requiring high longitudinal coherence), the flexible laser system that produces the seed2 pulse can potentially minimize the bandwidth. This includes not only the duration of seed2 pulse, but also potential compensation for the imprinted CSR wake by laser chirp and/or wavelength shift.

In order to effectively use either of the optimization methods, we need to know the exact shape of the CSR wake that we are compensating for. As we see from Sec. 3.3 this requires inclusion of transient, inter-dipole and, most importantly, chamber effects in calculation of CSR in the first EEHG chicane. Generating impedance data with `CSRZ` code solves this problem, but is, to some extent, computationally inconvenient. The impedance data for the chicane for 4 nm EEHG working point used in this work can be also used for other working points, as long as the bending radius of the dipoles does not change significantly. Beams that follow (almost) the same trajectory can be studied with the same simulation set-up even if they have varying current, energy and energy spread profiles. The longitudinal shape of the bunch is of utmost importance for calculation of CSR, as we have seen from comparison of CSR wakes for different lengths of Gaussian bunches. If the bunch is not Gaussian, but rather flat-top (or something in the middle between the two), the shape of the wake can also change significantly. For this reason, the work should be extended and included in start-to-end simulations to calculate the wakes for realistic beam distributions and to investigate possible compensation of the effect by non-transform-limited laser pulses. This will specify the requirements on the laser system for optimal spectral properties of seeded FEL at FLASH.

When using the short seed laser pulse it is also possible to choose, which part of the electron beam is seeded and will be eventually lasing [82]. In this work it was always assumed to be the center of the current profile. If the spectral purity is prioritized over the output power, we can longitudinally overlap the seed laser pulse with the region of the beam, where the energy profile is flat or mostly linearly chirped. In this case the spectrum will not be broadened by the CSR, but rather slightly shifted. The precise positioning of the laser pulse is somewhat complicated by the timing jitter. The jitter can also be a significant complication for the compensation of CSR wake with the laser chirp.

In principle, the CSR wakes could be also shaped by re-designing the chicane. In [41] we have shown that by changing the length of the chicane dipoles we can to some extent control the shape of the CSR wakes and the bunching spectrum. However, the conclusions were not as straight-forward as for the discussion on ISR and IBS in this work, as we did not observe any clear trend between the dipole length and the CSR-affected spectral bandwidth. On the other hand, a possibility of mitigating CSR-induced emittance by inventive chicane design was reported in the literature, e.g., by a five-bend chicane in [83]. The CSR-induced emittance was not discussed in the present work, since it is not relevant for the discussion of EEHG bunching formation. Also, simulations with `ELEGANT` estimate the contribution from CSR in the first chicane to be around 2 % of the intrinsic emittance value. However, this hints that chicane layout is a possible alternative method of controlling CSR-induced dynamics, if the more natural for FLASH2020+ methods discussed above will prove to be insufficient. For the purpose of optimizing the chicane geometry to minimize the effect of the wakefileds, other methods than `CSRZ` should be considered. For example, the parallel-plates CSR model can be a reasonable approximation, but it should be benchmarked for a substantially different chicane layouts.

4.3 MBI and Laser Heater

In Subsec. 3.4.2 we have seen experimental evidence that the laser heater at FLASH can substantially suppress the MBI. For this reason the effect of MBI on EEHG bunching was not studied in detail in this work. However, neglecting MBI in EEHG simulations is only justified for an isolated discussion of the beam dynamics in the seeding section, which is the focus of this work. Complete suppression of MBI comes at the cost of considerable attenuation of the FEL light. In this regard, this work serves as the necessary first step to include the effect of the LH in the simulation framework. The conclusion concerning the optimal LH setting should be defined for each working point individually. The integrated intensity of the output FEL pulse might be optimized at very low LH laser power. In contrast, a larger induced energy spread could benefit higher stability and spectral purity. Therefore, a dedicated LH study for different working points and optimization objectives could be a natural continuation of this work.

While simulation studies of the effect of MBI on EEHG bunching and mitigation of this effect with the LH would provide a better guideline for optimization of the set-up, it is essential to base the studies on reliable parameter sets for the electron beam at the LH, in particular the current and energy spread profiles. Accurate measurements and advanced diagnostic tools are crucial to guide the simulations effectively and ensure that the obtained insights are relevant and actionable. Realistic microbunching in the seeding section can also be included in calculation of CSR in the first EEHG chicane. In this case we could consider it as another contribution to Δp_2 in Eq. 2.112 and estimate its contribution to the bandwidth with Eq. 2.125.

Chapter 5

Conclusion

In this work we considered the influence of collective effects (ISR, IBS, CSR and MBI) on 4 nm EEHG performance at FLASH. While mitigation of ISR and IBS is rather complicated, the combined effect of the two is not expected to be a crucial factor for the efficiency of the harmonic conversion. The detrimental influence of CSR on the spectral properties of EEHG is substantial, but a number of mitigation strategies are possible. In particular, the strategy of using a short seed laser pulses was considered in this work in detail. We also demonstrated that MBI can be effectively mitigated with the recently installed laser heater at FLASH. The analysis presented in this work will be included in start-to-end simulations for a realistic estimation of output FEL light properties.

Overall, we conclude that the 4 nm EEHG operation mode (and by extension less challenging modes) at FLASH2020+ is not expected to be critically hindered by the collective effects, provided that the machine is properly tuned and the appropriate mitigation strategies are employed.

Appendix A

Notes on simulation set-up

A.1 Functionality of some ELEGANT elements

The User's manual for ELEGANT can be found here: https://ops.aps.anl.gov/manuals/elegant_latest/elegant.pdf
The manual entries for the elements are quite exhaustive and well-maintained, so I am not hoping (or trying) to explain them better. However, I believe that it might be beneficial to mention certain aspects explicitly in context of this work.

A.1.1 LSRMDLTR

Pole factors

The pole factors, mentioned in the discussion of $A_1(z)$ for a chirped electron beam in Subsec. 3.1.1, are set by default to the "magic" values, given explicitly in the manual. This is different for WIGGLER element of ELEGANT and UNDULATOR element of GENESIS. This might be a source of discrepancy if one would try to benchmark seemingly identical simulation files or different simulation codes.

Finite seed profile

The time profile of the seed laser is loaded into the LSRMDLTR element as a separate file. The header of the file suggests that we need to write $P(t)$ into the file. One might immediately think that P stands for power and, hence, we need to write a power profile. However, it is clarified in the manual that we actually need to write a field profile. For a Gaussian laser pulse that means that the width of the profile should be $\sqrt{2}$ times wider. This might be a source of confusion.

A.1.2 ZLONGIT

When preparing impedance data for loading into ZLONGIT element, it is important to remember two things. First, the number of data points in the file has to be $2^n + 1$, where n is integer. Second, if there is a data point for $f = 0$ (DC), Im $[Z(0)]$ has to be exactly 0. This might be a non-obvious source of some frustrating crashes.

A.2 Calculating modulation amplitudes

In order to estimate the modulation amplitude from the particle distributions produced by simulations we use

$$A_1 = \sqrt{2}\,\frac{1}{\sigma_E}\sqrt{\sigma_E^2\big|_{\text{mod1}} - \sigma_E^2}\,, \tag{A.1}$$

$$A_2 = \sqrt{2}\,\frac{1}{\sigma_E}\sqrt{\sigma_E^2\big|_{\text{mod2}} - \sigma_E^2\big|_{\text{ch1}}}\,, \tag{A.2}$$

where $\sigma_E\big|_{\text{mod1,mod2,ch1}}$ is the slice energy spread in the electron bunch after the first, the second modulator and the first chicane, respectively, and σ_E is the energy spread at the entrance of mod1.

Appendix B

Resistive wakefields

Since we discussed the effect of the chicane chamber of CSR wakefields, we should also mention another concept, related to the chamber walls: resistive wakefields (RW). In [48] we have compared the impedance of RW for parallel-plates [84] to the CSR impedance given by the parallel-plates model. For self-sufficiency of this work, we duplicate the results below.

The RW impedance is given by

$$Z_{RW}(k) = \frac{Z_0 c}{4\pi}\frac{2s_0}{ca^2}\int_0^\infty \mathrm{sech}(x)\left(\frac{2}{1-i}\frac{1}{\sqrt{ks_0}}\cosh(x) - iks_0\frac{\sinh(x)}{x}\right)^{-1} dx\,, \qquad \text{(B.1)}$$

where a is half-distance between the plates, $s_0 = (2a^2/Z_0\sigma_c)^{1/3}$ and σ_c is the conductivity of the resistive wall material. The chicane chamber is made of copper-coated steel, so we assumed copper as the material of the inner walls. From Fig. B.1 we see that the impedance of RW of parallel plates is negligibly small compared to the CSR impedance in PP-SS model. For this reason, the RW have been neglected in this work.

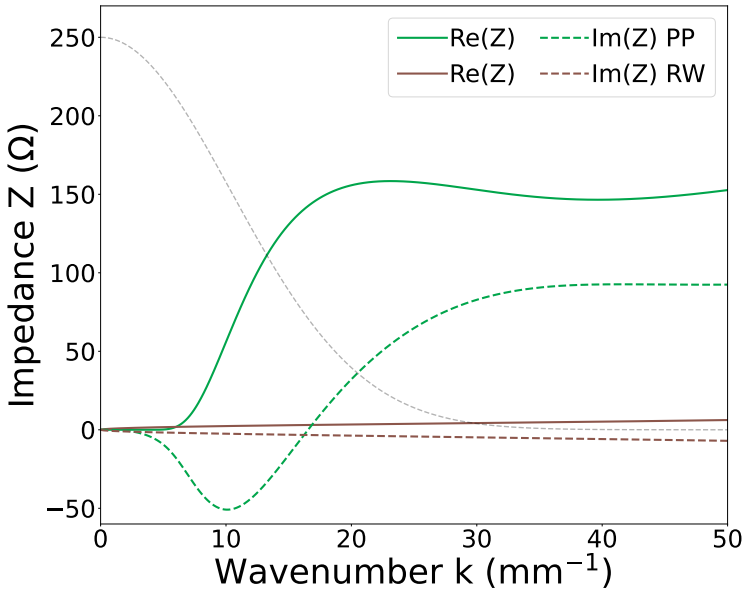

FIGURE B.1: CSR impedance of the parallel-plates model (PP) and resistive wakefields impedance (RW). The latter is fairly negligible in the relevant k-range, given by the bunch spectrum.

Appendix C

Twiss parameters in the seeding section

Since we discussed the evolution of the beam size in the seeding section in the context of IBS in Sec. 3.2, for completeness we give here the Twiss functions $\alpha_{x,y}$ and $\beta_{x,y}$ in the seeding section in Fig. C.1.

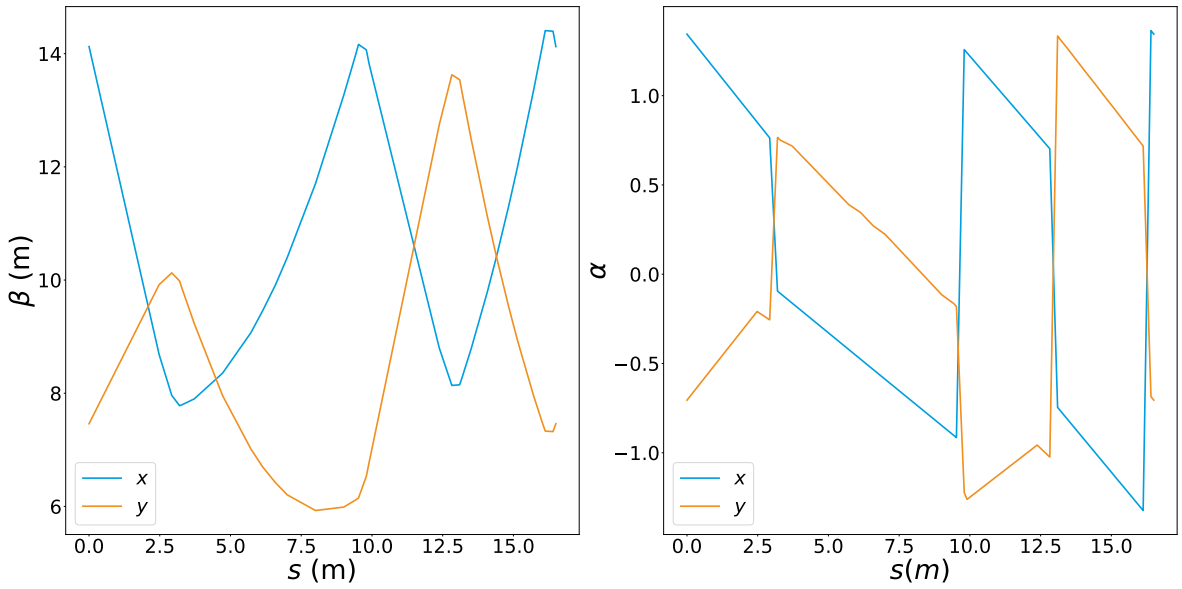

FIGURE C.1: Twiss functions $\alpha_{x,y}$ and $\beta_{x,y}$ in the seeding section. The coordinate s is measured from the entrance of mod1.

List of Figures

List of Tables

List of Symbols

$\mathcal{B}$	spectral brightness
t, t'	time coordinate
x, y	transverse displacement
x', y'	transverse angular displacement
$\hat{e}_{x,y,s}, \vec{n}$	unit vector
s	longitudinal coordinate along particle's trajectory
R	radius of curvature
$\vec{F}$	force
q	charge
$\vec{E}$	electric field
$\vec{v}$	velocity
$\vec{B}$	magnetic field
B_0	peak magnetic field
c	speed of light in vacuum
$\vec{p}$	particle's momentum
$p_{x,y}$	transverse particle's momentum
$k(s)$	quadrupole strength
$\vec{k}$	wave vector
k	wave number
l	3rd order multipole strength
m_0	particle's rest mass
m_e	electron rest mass
L_Q	quadrupole length
$f_{x,y}^Q$	focal length of the quadrupole
$\vec{j}$	current density
$\vec{A}$	magnetic vector potential
$\vec{r}, \vec{r'}$	coordinate vector
e	elementary charge
$\vec{S}$	Poynting vector
P	power
z	longitudinal (intra-bunch) coordinate
$\vec{X}$	particle's 6-vector
$\mathbb{R}$	6D transport matrix
$\mathbb{M}$	4D transport matrix
$\mathbb{B}$	beta matrix (Twiss)
$w_{\parallel}$	longitudinal wake function
$W_{\parallel}$	longitudinal wake potential
$Z(k)$	impedance
$I(z)$	current
I_0	peak current
P_0	peak power

r	radial coordinate
$\mathcal{E}_0$	peak electric field
E_0	central energy of electron beam
$w(z)$	laser beam waist
k_L	laser field wavenumber
z_R	Rayleigh length
R_w	curvature of the wavefront
E	energy
V_{RF}	RF voltage
f	frequency
h_1	electron beam linear energy chirp
k_u	undulator wavenumber
K_u	undulator parameter
N_u	number of undulator periods
L_u	undulator length
k_p	space charge parameter
n_e	electron density
L_g	gain length
$P_{\mathrm{in,\ out}}$	input and output power
P_{sat}	saturation power
P_e	electron beam power
p	relative energy deviation (from central energy)
$A_{1,2}$	normalized energy modulation
$B_{1,2}$	normalized longitudinal dispersion
$k_{1,2}$	seed laser wavenumber
$b_{n,m}, b$	bunching factor
$f_{\mathrm{ISR,\ IBS}}$	geometrical factor for ISR and IBS
r_e	classical electron radius
$\mathcal{B}_u$	peak magnetic field of undulator
h_2	quadratic electron beam chirp
$b_{\mathrm{min,\ max}}$	minimal and maximal impact parameter
k_{th}	theroshold wavenumber
h	chamber height
Z_0	impedance of free space
l_b	length of a bending magnet
l_d, L_d	length of a drift
z_L	CSR slippage length
Δz_{max}	cut-off distance (CSR)
G	microbunching gain
C	linear compression factor
r_b	electron beam radius
φ_{RF}	RF phase
ω	angular frequency
$\sigma_{x,y}^{\mathrm{ph}}$	RMS transverse size of photon beam
$\sigma_{x,y}^{\mathrm{e}}$	RMS transverse size of electron beam
$\sigma_{x,y}^{\mathrm{ph}}$	RMS angular divergence of photon beam
$\sigma_{x,y}^{\mathrm{e}}$	RMS angular divergence of electron beam
κ	dipole strength
ϵ_0	vacuum permitivity
ρ	charge density

μ_0	vacuum permeability
Φ	electric scalar potential
$\vec{\beta}_\gamma$	normalized particle's velocity
γ	Lorentz factor
Ω	solid angle
θ	polar angle
ϕ	azimuthal angle
ϑ	bending angle
$\epsilon_{x,y}$	transverse emittance
$\alpha_{x,y}$	alpha function (Twiss)
$\beta_{x,y}$	beta function (Twiss)
$\gamma_{T_{x,y}}$	gamma function (Twiss)
$\lambda(s,z)$	line charge density
σ_t	laser pulse duration
$\sigma_{\omega,k,\lambda}$	spectral width
λ_L	laser field wavelength
σ_E	energy spread
λ_u	undulator period
λ_{slip}	slippage length
ω_u	undulator angular frequency
λ_l	undulator radiation wavelength
ω_l	undulator radiation angular frequency
$\Delta\gamma$	energy modulation
$\bar{\beta}_\gamma$	average normalized longitudinal velocity
$\psi(t)$	pondermotive phase
$\nu(z)$	detuning parameter
η	relative energy deviation (from resonance)
Γ	gain paraemter
ω_p^*	plasma frequency
ρ_{FEL}	Pierce parameter
ζ_E	EEHG scaling factor
a_E	harmonic number
$\eta_{\text{ISR, IBS}}$	bunching smearing factor
ρ_u	undulator bending radius
α	fine structure constant
λ_D	Debye length
$\sigma_\perp$	transverse size of the beam

Acknowledgements

The author acknowledges DESY, Germany, a member of the Helmholtz Association HGF, for the provision of experimental facilities. This work has been carried out at FLASH. This work has been supported by BMBF within the project 05K19GUC. The author would like to thank the Maxwell computational resources operated at Deutsches Elektronen-Synchrotron (DESY), Hamburg, Germany. The author gratefully acknowledges the Gauss Centre for Supercomputing e.V. (www.gauss-centre.eu) for funding this project by providing computing time through the John von Neumann Institute for Computing (NIC) on the GCS Supercomputer JUWELS [85] at Jülich Supercomputing Centre (JSC). The author also acknowledges the funding through the Lund-Hamburg "IFELD" collaboration.

I would like to thank my supervisors Wolfgang Hillert and Lucas Schaper for giving me the opportunity to work on this project, for introducing me to the working environment at DESY, for navigating administrative and financial aspects, and for helping me to shape up this work. I would like to thank Demin Zhou and Najmeh Mirian for their invaluable help with CSR-related part of the work, and I am grateful to Mihai Pop for initially introducing me to the topic. I would like to thank Christopher Gerth and all members of the laser heater team at FLASH for the fruitful beamtimes and their help in finalizing the results. I would also like to thank Eugenio Ferrari, Sven Ackermann, Philipp Amstutz and Enrico Allaria for very helpful discussions on various topics.

A special and immeasurable chunk of gratitude goes to Pardis Niknejadi for her advise and support on daily basis, for continuous guidance during this work, for countless questions answered and explanations given, for her initiative and relentlessness in addressing my problems, for always having my back and prioritizing my interests, and for many other things I simply can't wrap up in words.

I would like to thank (in order of appearance) Fabian Pannek, Georgia Paraskaki, Andreas Thiel, Margarit Asatrian and Hendrik Wenzel for helpful work-related discussions, for not-necessarily-helpful discussions on random topics, and for adding some colors to my daily work-life. I would also like to thank every member (former or active) of Xseed team for making the beamtimes at FLASH not only an educational, but also a fun experience.

I am deeply grateful to my family and friends for their support during the stressful times. Most of all, I want to thank my loving wife Mila for her care and patience, for giving me strength and motivation, and just for being there no matter what. I simply couldn't do it without you. I would also thank Baloo, but he's a dog and can't read.

Bibliography

[1] F. R. Elder et al. “Radiation from Electrons in a Synchrotron”. In: *Phys. Rev.* 71 (11 June 1947), pp. 829–830. DOI: 10.1103/PhysRev.71.829.5. URL: https://link.aps.org/doi/10.1103/PhysRev.71.829.5.

[2] John M. J. Madey. “Stimulated Emission of Bremsstrahlung in a Periodic Magnetic Field”. In: *Journal of Applied Physics* 42.5 (Apr. 1971), pp. 1906–1913. ISSN: 0021-8979. DOI: 10.1063/1.1660466. eprint: https://pubs.aip.org/aip/jap/article-pdf/42/5/1906/18357380/1906_1_online.pdf. URL: https://doi.org/10.1063/1.1660466.

[3] Luis R. Elias et al. “Observation of Stimulated Emission of Radiation by Relativistic Electrons in a Spatially Periodic Transverse Magnetic Field”. In: *Phys. Rev. Lett.* 36 (13 Mar. 1976), pp. 717–720. DOI: 10.1103/PhysRevLett.36.717. URL: https://link.aps.org/doi/10.1103/PhysRevLett.36.717.

[4] D. A. G. Deacon et al. “First Operation of a Free-Electron Laser”. In: *Phys. Rev. Lett.* 38 (16 Apr. 1977), pp. 892–894. DOI: 10.1103/PhysRevLett.38.892. URL: https://link.aps.org/doi/10.1103/PhysRevLett.38.892.

[5] A M Kondratenko and E L Saldin. “Generating Of Coherent Radiation By A Relativistic Electron beam In An ondulator”. In: *Part. Accel.* 10 (1980), pp. 207–216. URL: https://cds.cern.ch/record/1107977.

[6] W. Ackermann et al. “Operation of a free-electron laser from the extreme ultraviolet to the water window”. en. In: *Nature Photon* 1.6 (June 2007). Publisher: Nature Publishing Group, pp. 336–342. ISSN: 1749-4893. DOI: 10.1038/nphoton.2007.76. URL: https://www.nature.com/articles/nphoton.2007.76 (visited on 06/25/2024).

[7] P. Emma et al. “First lasing and operation of an ångstrom-wavelength free-electron laser”. en. In: *Nature Photon* 4.9 (Sept. 2010). Publisher: Nature Publishing Group, pp. 641–647. ISSN: 1749-4893. DOI: 10.1038/nphoton.2010.176. URL: https://www.nature.com/articles/nphoton.2010.176 (visited on 06/16/2024).

[8] Eduard Prat et al. “A compact and cost-effective hard X-ray free-electron laser driven by a high-brightness and low-energy electron beam”. en. In: *Nat. Photonics* 14.12 (Dec. 2020). Number: 12 Publisher: Nature Publishing Group, pp. 748–754. ISSN: 1749-4893. DOI: 10.1038/s41566-020-00712-8. URL: https://www.nature.com/articles/s41566-020-00712-8 (visited on 08/04/2023).

[9] Heung-Sik Kang et al. “Hard X-ray free-electron laser with femtosecond-scale timing jitter”. en. In: *Nature Photon* 11.11 (Nov. 2017). Publisher: Nature Publishing Group, pp. 708–713. ISSN: 1749-4893. DOI: 10.1038/s41566-017-0029-8. URL: https://www.nature.com/articles/s41566-017-0029-8 (visited on 06/16/2024).

[10] Zhirong Huang and Ingolf Lindau. "SACLA hard-X-ray compact FEL". en. In: *Nature Photon* 6.8 (Aug. 2012). Publisher: Nature Publishing Group, pp. 505–506. ISSN: 1749-4893. DOI: 10.1038/nphoton.2012.184. URL: https://www.nature.com/articles/nphoton.2012.184 (visited on 06/25/2024).

[11] L. H. Yu. "Generation of intense uv radiation by subharmonically seeded single-pass free-electron lasers". In: *Phys. Rev. A* 44 (8 Aug. 1991), pp. 5178–5193. DOI: 10.1103/PhysRevA.44.5178. URL: https://link.aps.org/doi/10.1103/PhysRevA.44.5178.

[12] G. Stupakov. "Using the Beam-Echo Effect for Generation of Short-Wavelength Radiation". In: *Phys. Rev. Lett.* 102 (7 Feb. 2009), p. 074801. DOI: 10.1103/PhysRevLett.102.074801. URL: https://link.aps.org/doi/10.1103/PhysRevLett.102.074801.

[13] Primož Rebernik Ribič et al. "Coherent soft X-ray pulses from an echo-enabled harmonic generation free-electron laser". en. In: *Nat. Photonics* 13.8 (Aug. 2019). Publisher: Nature Publishing Group, pp. 555–561. ISSN: 1749-4893. DOI: 10.1038/s41566-019-0427-1. URL: https://www.nature.com/articles/s41566-019-0427-1 (visited on 06/17/2024).

[14] E. L Saldin, E. A Schneidmiller, and M. V Yurkov. "Longitudinal space charge-driven microbunching instability in the TESLA Test Facility linac". In: *Nuclear Instruments and Methods in Physics Research Section A: Accelerators, Spectrometers, Detectors and Associated Equipment*. Proceedings of the 25th International Free Electron Laser Conference, and the 10th FEL Users Workshop 528.1 (Aug. 2004), pp. 355–359. ISSN: 0168-9002. DOI: 10.1016/j.nima.2004.04.067. URL: https://www.sciencedirect.com/science/article/pii/S016890020400720X (visited on 06/17/2024).

[15] E.L. Saldin, E.A. Schneidmiller, and M.V. Yurkov. "An analytical description of longitudinal phase space distortions in magnetic bunch compressors". In: *Nuclear Instruments and Methods in Physics Research Section A: Accelerators, Spectrometers, Detectors and Associated Equipment* 483.1 (2002). Proceedings of the 23rd International Free Electron Laser Confere nce and 8th FEL Users Workshop, pp. 516–520. ISSN: 0168-9002. DOI: https://doi.org/10.1016/S0168-9002(02)00372-8. URL: https://www.sciencedirect.com/science/article/pii/S0168900202003728.

[16] Zhen Zhang et al. "Microbunching-instability-induced sidebands in a seeded free-electron laser". In: *Phys. Rev. Accel. Beams* 19.5 (May 2016). Publisher: American Physical Society, p. 050701. DOI: 10.1103/PhysRevAccelBeams.19.050701. URL: https://link.aps.org/doi/10.1103/PhysRevAccelBeams.19.050701 (visited on 06/28/2024).

[17] Matthew Sands. "Synchrotron oscillations induced by radiation fluctuations". In: *Physical Review* 97.2 (1955). Cited by: 41, pp. 470–473. DOI: 10.1103/PhysRev.97.470. URL: https://www.scopus.com/inward/record.uri?eid=2-s2.0-0041861463&doi=10.1103%2fPhysRev.97.470&partnerID=40&md5=e6db949e9857fa2f9820a2224aebf4da.

[18] A Piwinski. "Intra-beam-scattering". In: (1974). DOI: 10.5170/CERN-1992-001.226. URL: https://cds.cern.ch/record/400720.

[19] E. Hemsing et al. "Sensitivity of echo enabled harmonic generation to sinusoidal electron beam energy structure". en. In: *Phys. Rev. Accel. Beams* 20.6 (June 2017), p. 060702. ISSN: 2469-9888. DOI: 10.1103/PhysRevAccelBeams.20.060702. URL: http://link.aps.org/doi/10.1103/PhysRevAccelBeams.20.060702 (visited on 01/05/2021).

[20] E. L. Saldin, E. A. Schneidmiller, and M. V. Yurkov. "On the coherent radiation of an electron bunch moving in an arc of a circle". en. In: *Nuclear Instruments and Methods in Physics Research Section A: Accelerators, Spectrometers, Detectors and Associated Equipment* 398.2 (Oct. 1997), pp. 373–394. ISSN: 0168-9002. DOI: 10.1016/S0168-9002(97)00822-X. URL: http://www.sciencedirect.com/science/article/pii/S016890029700822X (visited on 12/08/2020).

[21] Dao Xiang and Gennady Stupakov. "Echo-enabled harmonic generation free electron laser". In: *Phys. Rev. ST Accel. Beams* 12 (3 Mar. 2009), p. 030702. DOI: 10.1103/PhysRevSTAB.12.030702. URL: https://link.aps.org/doi/10.1103/PhysRevSTAB.12.030702.

[22] E. L Saldin, E. A Schneidmiller, and M. V Yurkov. "Longitudinal space charge-driven microbunching instability in the TESLA Test Facility linac". In: *Nucl. Instrum. Methods Phys. Res., Sect. A* 528.1 (2004), pp. 355–359. DOI: 10.1016/j.nima.2004.04.067.

[23] Z. Huang et al. "Measurements of the linac coherent light source laser heater and its impact on the x-ray free-electron laser performance". In: *Phys. Rev. ST Accel. Beams* 13 (2 Feb. 2010), p. 020703. DOI: 10.1103/PhysRevSTAB.13.020703.

[24] S. Spampinati et al. "Laser heater commissioning at an externally seeded free-electron laser". In: *Phys. Rev. ST Accel. Beams* 17 (12 Dec. 2014), p. 120705. DOI: 10.1103/PhysRevSTAB.17.120705.

[25] Lee JaeHyun et al. "PAL-XFEL laser heater commissioning". In: *Nucl. Instrum. Methods Phys. Res., Sect. A* 843 (2017), pp. 39–45. DOI: 10.1016/j.nima.2016.11.001.

[26] Intae Eom et al. "Recent Progress of the PAL-XFEL". en. In: *Applied Sciences* 12.3 (Jan. 2022). Number: 3 Publisher: Multidisciplinary Digital Publishing Institute, p. 1010. ISSN: 2076-3417. DOI: 10.3390/app12031010. URL: https://www.mdpi.com/2076-3417/12/3/1010 (visited on 06/28/2024).

[27] Mathias Hamberg, Frank Brinker, and Matthias Scholz. "First Heating with the European XFEL Laser Heater". en. In: *Proceedings of the 5th Int. Beam Instrumentation Conf.* IBIC2016 (2017). Artwork Size: 3 pages, 0.755 MB ISBN: 9783954501779 Medium: PDF Publisher: JACoW, Geneva, Switzerland, 3 pages, 0.755 MB. DOI: 10.18429/JACOW-IBIC2016-WEPG32. URL: http://jacow.org/ibic2016/doi/JACoW-IBIC2016-WEPG32.html (visited on 06/28/2024).

[28] Simon Fahlström et al. "NIR spectrometer for bunch-resolved, non-destructive studies of microbunching at European XFEL". In: *39th Free Electron Laser Conference (FEL'19), Hamburg, Germany, 26-30 August 2019*. JACOW Publishing, Geneva, Switzerland. 2019, pp. 392–395.

[29] D. Samoilenko et al. "First beam heating with the laser heater for FLASH2020+". English. In: *Proc. IPAC'23* (Venice, Italy). IPAC'23 - 14th International Particle Accelerator Conference 14. JACoW Publishing, Geneva, Switzerland, May 2023, pp. 1950–1953. ISBN: 978-3-95450-231-8. DOI: 10.18429/JACoW-IPAC2023-TUPL098. URL: https://indico.jacow.org/event/41/contributions/1387.

[30] Alexander Wu Chao et al., eds. *Handbook of accelerator physics and engineering; Third edition*. Hackensack: World Scientific, 2023, xvii, 909 pages, 31 pages : illustrations, diagrams. ISBN: 9789811270154. DOI: 10.1142/13229. URL: https://bib-pubdb1.desy.de/record/490823.

[31] Gregory Penn. *EEHG Performance and Scaling Laws*. en. Tech. rep. LBNL-6481E, 1164809. Oct. 2013, LBNL–6481E, 1164809. DOI: 10.2172/1164809. URL: http://www.osti.gov/servlets/purl/1164809/ (visited on 12/11/2020).

[32] S. Di Mitri et al. "Experimental evidence of intrabeam scattering in a free-electron laser driver". en. In: *New J. Phys.* 22.8 (Aug. 2020). Publisher: IOP Publishing, p. 083053. ISSN: 1367-2630. DOI: 10.1088/1367-2630/aba572. URL: https://dx.doi.org/10.1088/1367-2630/aba572 (visited on 05/31/2024).

[33] Z Huang. *Intrabeam Scattering in an X-ray FEL Driver*. en. Tech. rep. SLAC-TN-05-026, 839686. Jan. 2005, SLAC–TN–05–026, 839686. DOI: 10.2172/839686. URL: http://www.osti.gov/servlets/purl/839686/ (visited on 01/29/2024).

[34] E. Hemsing et al. "Soft x-ray seeding studies for the SLAC Linac Coherent Light Source II". en. In: *Phys. Rev. Accel. Beams* 22.11 (Nov. 2019), p. 110701. ISSN: 2469-9888. DOI: 10.1103/PhysRevAccelBeams.22.110701. URL: https://link.aps.org/doi/10.1103/PhysRevAccelBeams.22.110701 (visited on 07/25/2023).

[35] Kaishang Zhou, Chao Feng, and Dong Wang. "Feasibility study of generating ultra-high harmonic radiation with a single stage echo-enabled harmonic generation scheme". en. In: *Nuclear Instruments and Methods in Physics Research Section A: Accelerators, Spectrometers, Detectors and Associated Equipment* 834 (Oct. 2016), pp. 30–35. ISSN: 01689002. DOI: 10.1016/j.nima.2016.07.021. URL: https://linkinghub.elsevier.com/retrieve/pii/S0168900216307379 (visited on 07/06/2021).

[36] E Prat and S Reiche. "EEHG seeding design for SwissFEL". In: *TUPA25, Proceedings of FEL* (2011).

[37] X. Yang et al. "Toward a fully coherent tender and hard X-ray free-electron laser via cascaded EEHG in fourth-generation synchrotron light sources". In: *Journal of Synchrotron Radiation* 30.5 (Sept. 2023), pp. 861–875. DOI: 10.1107/S1600577523006586. URL: https://doi.org/10.1107/S1600577523006586.

[38] Weijie Fan et al. "Hybrid echo-enabled harmonic generation scheme for seeding coherent soft x-ray free-electron lasers". In: *Nuclear Instruments and Methods in Physics Research Section A: Accelerators, Spectrometers, Detectors and Associated Equipment* 1027 (2022), p. 166241. ISSN: 0168-9002. DOI: https://doi.org/10.1016/j.nima.2021.166241. URL: https://www.sciencedirect.com/science/article/pii/S0168900221010822.

[39] E. Hemsing. "Bunching phase and constraints on echo enabled harmonic generation". In: *Phys. Rev. Accel. Beams* 21 (5 May 2018), p. 050702. DOI: 10.1103/PhysRevAccelBeams.21.050702. URL: https://link.aps.org/doi/10.1103/PhysRevAccelBeams.21.050702.

[40] E. Hemsing et al. "Soft x-ray seeding studies for the SLAC Linac Coherent Light Source II". In: *Phys. Rev. Accel. Beams* 22 (11 Nov. 2019), p. 110701. DOI: 10.1103/PhysRevAccelBeams.22.110701. URL: https://link.aps.org/doi/10.1103/PhysRevAccelBeams.22.110701.

[41] Dmitrii Samoilenko et al. "Discussion on CSR instability in EEHG Simulation". In: *12th International Particle Accelerator Conference*. Aug. 2021. DOI: 10.18429/JACoW-IPAC2021-TUPAB103.

[42] D. Samoilenko et al. "Sensitivity of EEHG simulations to dynamic beam parameters". In: *JACoW* IPAC2022 (2022), TUPOMS024. DOI: 10.1088/1742-6596/2420/1/012024.

[43] Mihai Pop et al. "Mitigation of CSR induced spectral broadening in EEHG FEL". In: *Nuclear Instruments and Methods in Physics Research Section A: Accelerators, Spectrometers, Detectors and Associated Equipment* 1048 (2023), p. 167926. ISSN: 0168-9002. DOI: https://doi.org/10.1016/j.nima.2022.167926. URL: https://www.sciencedirect.com/science/article/pii/S0168900222012189.

[44] G. Stupakov and P. Emma. "CSR wake for a short magnet in ultrarelativistic limit". In: *Proceedings of EPAC*. Citeseer. 2002, p. 1479.

[45] Christopher Mayes and Georg Hoffstaetter. "Exact 1D model for coherent synchrotron radiation with shielding and bunch compression". In: *Physical Review Special Topics-Accelerators and Beams* 12.2 (2009), p. 024401.

[46] David Sagan et al. "Extended one-dimensional method for coherent synchrotron radiation including shielding". In: *Physical Review Special Topics-Accelerators and Beams* 12.4 (2009), p. 040703.

[47] William Lou and GH Hoffstaetter. "Coherent synchrotron radiation wake expressions with two bending magnets and simulation results for a multiturn energy-recovery linac". In: *Physical Review Accelerators and Beams* 23.5 (2020), p. 054404.

[48] D. Samoilenko et al. "Calculation of the CSR Effect on EEHG Performance". English. In: *Proc. FEL2022* (Trieste). International Free Electron Laser Conference 40. JACoW Publishing, Geneva, Switzerland, Aug. 2022, pp. 326–329. ISBN: 978-3-95450-220-2. DOI: 10.18429/JACoW-FEL2022-TUP74. URL: https://indico.jacow.org/event/44/contributions/483.

[49] *An Alternative 1D Model for CSR with Chamber Shielding*. en. 2012.

[50] Demin Zhou et al. "Calculation of Coherent Synchrotron Radiation Impedance for a Beam Moving in a Curved Trajectory". In: *Japanese Journal of Applied Physics* 51.1R (Dec. 2011), p. 016401. DOI: 10.1143/JJAP.51.016401. URL: https://dx.doi.org/10.1143/JJAP.51.016401.

[51] Wolfgang Hillert. *Transverse Linear Beam Dynamics*. 2021. arXiv: 2107.02614 [physics.acc-ph].

[52] Martin Dohlus and Rainer Wanzenberg. "An Introduction to Wake Fields and Impedances". en. In: *CERN Yellow Reports: School Proceedings* 3 (July 2017), pp. 15–15. ISSN: 2519-805X. DOI: 10.23730/CYRSP-2017-003.15. URL: https://e-publishing.cern.ch/index.php/CYRSP/article/view/338 (visited on 06/21/2024).

[53] Peter Schmüser et al. *Free-Electron Lasers in the Ultraviolet and X-Ray Regime*. en. Vol. 258. Springer Tracts in Modern Physics. Cham: Springer International Publishing, 2014. ISBN: 978-3-319-04081-3. DOI: 10.1007/978-3-319-04081-3. URL: http://link.springer.com/10.1007/978-3-319-04081-3 (visited on 12/10/2020).

[54] B. Aune et al. "Superconducting TESLA cavities". en. In: *Phys. Rev. ST Accel. Beams* 3.9 (Sept. 2000), p. 092001. ISSN: 1098-4402. DOI: 10.1103/PhysRevSTAB.3.092001. URL: https://link.aps.org/doi/10.1103/PhysRevSTAB.3.092001 (visited on 01/09/2024).

[55] Erik Hemsing et al. "Beam by design: laser manipulation of electrons in modern accelerators". In: *Rev. Mod. Phys.* 86.3 (July 2014). arXiv:1404.2579 [physics], pp. 897–941. ISSN: 0034-6861, 1539-0756. DOI: 10.1103/RevModPhys.86.897. URL: http://arxiv.org/abs/1404.2579 (visited on 04/22/2024).

[56] Lucas Schaper et al. "Flexible and Coherent Soft X-ray Pulses at High Repetition Rate: Current Research and Perspectives". en. In: *Applied Sciences* 11.20 (Jan. 2021). Number: 20 Publisher: Multidisciplinary Digital Publishing Institute, p. 9729. ISSN: 2076-3417. DOI: 10.3390/app11209729. URL: https://www.mdpi.com/2076-3417/11/20/9729 (visited on 06/14/2023).

[57] Martin Beye et al. "FLASH and the FLASH2020+ project—current status and upgrades for the free-electron laser in Hamburg at DESY". en. In: *Eur. Phys. J. Plus* 138.3 (Mar. 2023), p. 193. ISSN: 2190-5444. DOI: 10.1140/epjp/s13360-023-03814-8. URL: https://doi.org/10.1140/epjp/s13360-023-03814-8 (visited on 06/22/2024).

[58] R. D'Arcy et al. "FLASHForward: plasma wakefield accelerator science for high-average-power applications". In: *Philosophical Transactions of the Royal Society A: Mathematical, Physical and Engineering Sciences* 377.2151 (June 2019). Publisher: Royal Society, p. 20180392. DOI: 10.1098/rsta.2018.0392. URL: https://royalsocietypublishing.org/doi/10.1098/rsta.2018.0392 (visited on 06/22/2024).

[59] Luca Giannessi. "Seeding and Harmonic Generation in Free-Electron Lasers". In: *Synchrotron Light Sources and Free-Electron Lasers: Accelerator Physics, Instrumentation and Science Applications*. Ed. by Eberhard J. Jaeschke et al. Cham: Springer International Publishing, 2016, pp. 195–223. ISBN: 978-3-319-14394-1. DOI: 10.1007/978-3-319-14394-1_3. URL: https://doi.org/10.1007/978-3-319-14394-1_3.

[60] G. Dattoli et al. "Semi-analytical model of self-amplified spontaneous-emission free-electron lasers, including diffraction and pulse-propagation effects". In: *Journal of Applied Physics* 95.6 (Mar. 2004), pp. 3206–3210. ISSN: 0021-8979. DOI: 10.1063/1.1645979. URL: https://doi.org/10.1063/1.1645979 (visited on 06/19/2024).

[61] Z. Huang et al. *Effects of Energy Chirp on Echo-Enabled Harmonic Generation Free-Electron Lasers*. en. Tech. rep. SLAC-PUB-13547, 948487. Feb. 2009, SLAC–PUB–13547, 948487. DOI: 10.2172/948487. URL: http://www.osti.gov/servlets/purl/948487-2O58kw/ (visited on 11/07/2023).

[62] Paola Finetti et al. "Pulse Duration of Seeded Free-Electron Lasers". In: *Phys. Rev. X* 7.2 (June 2017). Publisher: American Physical Society, p. 021043. DOI: 10.1103/PhysRevX.7.021043. URL: https://link.aps.org/doi/10.1103/PhysRevX.7.021043 (visited on 03/14/2024).

[63] Julian Schwinger. "On the Classical Radiation of Accelerated Electrons". In: *Phys. Rev.* 75.12 (June 1949). Publisher: American Physical Society, pp. 1912–1925. DOI: 10.1103/PhysRev.75.1912. URL: https://link.aps.org/doi/10.1103/PhysRev.75.1912 (visited on 01/16/2024).

[64] K. Wille. *The physics of particle accelerators: An introduction*. 2000.

[65] Nikolai Yampolsky and Bruce E. Carlsten. "Beam debunching due to ISR-induced energy diffusion". In: *Nuclear Instruments and Methods in Physics Research Section A: Accelerators, Spectrometers, Detectors and Associated Equipment* 870 (2017), pp. 156–162. ISSN: 0168-9002. DOI: https://doi.org/10.1016/j.nima.2017.06.023. URL: https://www.sciencedirect.com/science/article/pii/S0168900217306769.

[66] Yaroslav S. Derbenev et al. *Microbunch radiative tail-head interaction*. Tech. rep. Hamburg: DESY, 1995. URL: https://cds.cern.ch/record/291102.

[67] S. Di Mitri et al. "Design and simulation challenges for FERMI@elettra". In: *Nuclear Instruments and Methods in Physics Research Section A: Accelerators, Spectrometers, Detectors and Associated Equipment* 608.1 (2009), pp. 19–27. ISSN: 0168-9002. DOI: https://doi.org/10.1016/j.nima.2009.06.028. URL: https://www.sciencedirect.com/science/article/pii/S0168900209012340.

[68] S. Heifets and G. Stupakov. "Beam instability and microbunching due to CSR". In: *Proceedings of the PAC*. 2001.

[69] M. Borland et al. "Start-to-end simulation of self-amplified spontaneous emission free electron lasers from the gun through the undulator". en. In: *Nuclear Instruments and Methods in Physics Research Section A: Accelerators, Spectrometers, Detectors and Associated Equipment* 483.1-2 (May 2002), pp. 268–272. ISSN: 01689002. DOI: 10.1016/S0168-9002(02)00325-X. URL: https://linkinghub.elsevier.com/retrieve/pii/S016890020200325X (visited on 10/12/2023).

[70] Bas Van Der Geer et al. "GPT-CSR: A New Simulation Code for CSR Effects". en. In: *Proceedings of the 60th ICFA Advanced Beam Dynamics Workshop on Future Light Sources* FLS2018 (2018). Artwork Size: 3 pages, 0.978 MB ISBN: 9783954502066 Medium: PDF Publisher: JACoW Publishing, Geneva, Switzerland, 3 pages, 0.978 MB. DOI: 10.18429/JACOW-FLS2018-THA1WA03. URL: http://jacow.org/fls2018/doi/JACoW-FLS2018-THA1WA03.html (visited on 12/10/2023).

[71] Alexander Brynes et al. "Understanding 1D to 3D coherent synchrotron radiation Effects". In: *39th Free Electron Laser Conference (FEL'19), Hamburg, Germany, 26-30 August 2019*. JACOW Publishing, Geneva, Switzerland. 2019, pp. 578–583.

[72] S. Heifets, G. Stupakov, and S. Krinsky. "Coherent synchrotron radiation instability in a bunch compressor". In: *Phys. Rev. ST Accel. Beams* 5 (6 June 2002), p. 064401. DOI: 10.1103/PhysRevSTAB.5.064401. URL: https://link.aps.org/doi/10.1103/PhysRevSTAB.5.064401.

[73] T Agoh and K Yokoya. "Calculation of coherent synchrotron radiation using mesh". In: *Physical Review Special Topics-Accelerators and Beams* 7.5 (2004), p. 054403.

[74] M. Borland. "Simple method for particle tracking with coherent synchrotron radiation". en. In: *Phys. Rev. ST Accel. Beams* 4.7 (July 2001), p. 070701. ISSN: 1098-4402. DOI: 10.1103/PhysRevSTAB.4.070701. URL: https://link.aps.org/doi/10.1103/PhysRevSTAB.4.070701 (visited on 05/20/2021).

[75] M Borland. "ELEGANT: A flexible SDDS-compliant code for accelerator simulation". In: (Aug. 2000). DOI: 10.2172/761286. URL: https://www.osti.gov/biblio/761286.

[76] Gennady Stupakov and Demin Zhou. "Analytical theory of coherent synchrotron radiation wakefield of short bunches shielded by conducting parallel plates". In: *Phys. Rev. Accel. Beams* 19 (4 Apr. 2016), p. 044402. DOI: 10.1103/PhysRevAccelBeams.19.044402. URL: https://link.aps.org/doi/10.1103/PhysRevAccelBeams.19.044402.

[77] E. L. Saldin, E. A. Schneidmiller, and M. V. Yurkov. "Klystron instability of a relativistic electron beam in a bunch compressor". In: *Nuclear Instruments and Methods in Physics Research Section A: Accelerators, Spectrometers, Detectors and Associated Equipment* 490.1 (Sept. 2002), pp. 1–8. ISSN: 0168-9002. DOI: 10.1016/S0168-9002(02)00905-1. URL: https://www.sciencedirect.com/science/article/pii/S0168900202009051 (visited on 01/09/2024).

[78] Z. Huang et al. "Suppression of microbunching instability in the linac coherent light source". In: *Phys. Rev. ST Accel. Beams* 7 (7 July 2004), p. 074401. DOI: 10.1103/PhysRevSTAB.7.074401. URL: https://link.aps.org/doi/10.1103/PhysRevSTAB.7.074401.

[79] S. Di Mitri and M. Cornacchia. "Electron beam brightness in linac drivers for free-electron-lasers". In: *Physics Reports* 539.1 (2014), pp. 1–48. ISSN: 0370-1573. DOI: https://doi.org/10.1016/j.physrep.2014.01.005. URL: https://www.sciencedirect.com/science/article/pii/S0370157314000088.

[80] E. Allaria et al. "Highly coherent and stable pulses from the FERMI seeded free-electron laser in the extreme ultraviolet". In: *Nature Photonics* 6.10 (2012), pp. 699–704. DOI: 10.1038/nphoton.2012.233.

[81] Ph. Amstutz and M. Vogt. "Microbunching Studies for the FLASH2020+ Upgrade Using a Semi-Lagrangian Vlasov Solver". In: *Proc. IPAC'22* (Bangkok, Thailand). International Particle Accelerator Conference 13. JACoW Publishing, Geneva, Switzerland, July 2022, WEPOMS037, pp. 2334–2337. ISBN: 978-3-95450-227-1. DOI: 10.18429/JACoW-IPAC2022-WEPOMS037. URL: https://jacow.org/ipac2022/papers/wepoms037.pdf.

[82] F. Pannek et al. "Mitigation of Beam Instabilities in the Echo-Enabled Harmonic Generation Beamline for FLASH2020+". In: *Proc. IPAC'21* (Campinas, SP, Brazil). International Particle Accelerator Conference 12. https://doi.org/10.18429/JACoW-IPAC2021-FRXA06. JACoW Publishing, Geneva, Switzerland, Aug. 2021, FRXA06, pp. 4514–4517. ISBN: 978-3-95450-214-1. DOI: 10.18429/JACoW-IPAC2021-FRXA06. URL: https://jacow.org/ipac2021/papers/frxa06.pdf.

[83] Donish Z. Khan and Tor O. Raubenheimer. "Novel bunch compressor chicane: The five-bend chicane". en. In: *Phys. Rev. Accel. Beams* 25.9 (Sept. 2022), p. 090701. ISSN: 2469-9888. DOI: 10.1103/PhysRevAccelBeams.25.090701. URL: https://link.aps.org/doi/10.1103/PhysRevAccelBeams.25.090701 (visited on 10/07/2022).

[84] Karl Bane and Gennady Stupakov. "Using surface impedance for calculating wakefields in flat geometry". In: *Phys. Rev. ST Accel. Beams* 18 (3 Mar. 2015), p. 034401. DOI: 10.1103/PhysRevSTAB.18.034401. URL: https://link.aps.org/doi/10.1103/PhysRevSTAB.18.034401.

[85] Jülich Supercomputing Centre. "JUWELS Cluster and Booster: Exascale Pathfinder with Modular Supercomputing Architecture at Juelich Supercomputing Centre". In: *Journal of large-scale research facilities* 7.A138 (2021). DOI: 10.17815/jlsrf-7-183. URL: http://dx.doi.org/10.17815/jlsrf-7-183.